



AMERICAN UNIVERSITY OF BEIRUT

ENHANCING LIGHT HARVESTING AND WATER  
OXIDATION AT Mo:BiVO<sub>4</sub> PHOTOANODES BY COUPLING  
WITH TiO<sub>2</sub> PHOTONIC CRYSTALS AND OXYGEN  
EVOLUTION CATALYSTS

by  
MARWA AHMAD AL RAMMAL

A thesis  
submitted in partial fulfillment of the requirements  
for the degree of Master of Science  
to the Department of Chemistry  
of the Faculty of Art and Sciences  
at the American University of Beirut

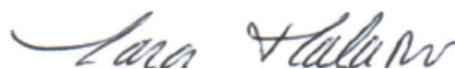
Beirut, Lebanon  
August 2021

AMERICAN UNIVERSITY OF BEIRUT

ENHANCING LIGHT HARVESTING AND WATER  
OXIDATION AT Mo:BiVO<sub>4</sub> PHOTOANODES BY COUPLING  
WITH TiO<sub>2</sub> PHOTONIC CRYSTALS AND OXYGEN  
EVOLUTION CATALYSTS

by  
MARWA AHMAD AL RAMMAL

Approved by:



---

Dr. Lara Halaoui, Professor  
Chemistry

Advisor



---

Dr. Digambara Patra, Professor  
Chemistry

Member of Committee



---

Dr. Faraj Hasanayn Professor  
Chemistry

Member of Committee

Date of thesis defense: August 12, 2021

# AMERICAN UNIVERSITY OF BEIRUT

## THESIS RELEASE FORM

Student Name: Al Rammal Marwa Ahmad  
Last First Middle

I authorize the American University of Beirut, to: (a) reproduce hard or electronic copies of my thesis; (b) include such copies in the archives and digital repositories of the University; and (c) make freely available such copies to third parties for research or educational purposes:

- As of the date of submission
- One year from the date of submission of my thesis.
- Two years from the date of submission of my thesis.
- Three years from the date of submission of my thesis.



17 August 2021

---

Signature

Date

## ACKNOWLEDGEMENTS

I express my thanks and gratitude to my research adviser Dr. Lara Halaoui for her constant guidance and overall professionalism. I am lucky and proud to be a member of her research group who provided me with indispensable knowledge and helped me to be the chemist I'm today.

I express my thanks and respect to the committee members, Dr. Digambara Patra and Dr. Faraj Hasanayn, for the feedback and guidance.

I like to thank with whole my heart Rida Farhat , Khalil Akkaoui and Jihan Dhainy for their guidance, motivation, and help during my journey in Dr.Halaoui's Laboratory.

I acknowledge the technical support and overall help of the CRSL team, Ms. Rania Shatila, Mr. Joan Younes, Mr. Samer Khalil and technicians Mr. Simon Al-Ghawi and Mr. Boutros Sawaya.

I dedicate this work to my beloved family for their never-ending support and motivation. I would like to offer my deepest gratitude and thanks to my mother Nour Al Sabah, my father Ahmad, my sisters, my brother, and my lovely grandma. I also sincerely dedicate this work to my precious friends Ahmed Bahaddin Al Salhi, and Dalia Ezzeddine who always support and believe in me during this journey.

# ABSTRACT OF THE THESIS OF

Marwa Ahmad Al Rammal

for

Master of Science  
Major: Chemistry

Title: Enhancing Light Harvesting and Water Oxidation at Mo:BiVO<sub>4</sub> Photoanodes by Coupling with TiO<sub>2</sub> Photonic Crystals and Oxygen Evolution Catalysts.

This MS thesis work aims to fabricate a Mo:BiVO<sub>4</sub> photoanode with improved photoelectrochemical properties for solar water splitting by coupling with photonic crystals to enhance absorbance in the films and oxygen evolution catalysts to enhance the kinetics of water oxidation. The effect of coupling Mo-doped BiVO<sub>4</sub> photoanode of different thickness to TiO<sub>2</sub> photonic crystals of varying stop bands on light harvesting in a photoelectrochemical cell was studied in sulfate sulfite electrolyte in the presence of a hole scavenger. The TiO<sub>2</sub> inverse opals stop band was varied by varying the sphere size in the opal template. The PEC behavior was compared to that of Mo:BiVO<sub>4</sub> coupled to disordered and non-scattering nanocrystalline films. This photoanode aimed to create heterojunction that facilitates electron separation and transport, and to enhance absorption by light trapping. Photocurrents were measured at Mo:BiVO<sub>4</sub> coupled to inverse opals with different stop bands leading to a significant enhancement in %IPCE. The photoanodes that are coupled with inverse glass and non-scattering nanocrystalline showed smaller enhancement or even showed decreased light harvesting efficiency. The second aim focuses on oxygen evolution reaction (OER) catalysts coupled with the photoanodes. In the second aim the electrolyte was varied to potassium borate solution to study water oxidation in the absence of hole scavenger. The bilayer photoanodes that were fabricated in the first aim were coupled to nickel borate (Ni-B<sub>i</sub>), which was observed to produce enhanced %IPCE of ca. 2.21-fold. Ni-B<sub>i</sub> is believed to have a dual role, a catalytic effect and decreasing recombination.

# TABLE OF CONTENTS

|   |    |
|---|----|
| ACKNOWLEDGEMENTS .....  | 1  |
| ABSTRACT .....  | 2  |
| ILLUSTRATIONS .....   | 7  |
| TABLES .....  | 11 |
| INTRODUCTION .....  | 12 |
| A. Photoelectrochemical Water Splitting .....   | 12 |
| B. Oxygen Evolution Reaction .....  | 14 |
| C. Semiconductor.....   | 16 |
| 1. Types of Semiconductors.....   | 16 |
| 2. Photoelectrochemistry at Semiconductor/Electrolyte Interface .....                                 | 17 |
| D. Mo:BiVO <sub>4</sub> Photoanode .....  | 19 |
| E. The Effect of Illumination Direction on Photoelectrochemical Performance.....                      | 20 |
| F. Photonic Crystals and Photonic Glass .....   | 21 |
| G. Previous Studies of Using Photonic Crystals and Disordered Films to Enhance Light Harvesting ..... | 23 |
| H. Previous Studies on TiO <sub>2</sub> coupled to BiVO <sub>4</sub> .....                            | 25 |
| I. Oxygen Evolution Catalysts Coupled to BiVO <sub>4</sub> Photoanodes .....                          | 26 |
| 1. Ni and Fe-oxo/hydroxide OER Electrocatalysts Coupled to BiVO <sub>4</sub> .....                    | 26 |
| 2. Ni-B; Co-catalyst Coupled to BiVO <sub>4</sub> .....   | 28 |
| J. The Work in This Thesis.....   | 29 |

|   |    |
|---|----|
| Experimental section .....  | 30 |
| A. Materials .....  | 30 |
| B. Preparation of Solutions .....   | 30 |
| 1. KB <sub>i</sub> electrolytes .....   | 30 |
| 2. Na <sub>2</sub> SO <sub>4</sub> in the presence of Na <sub>2</sub> SO <sub>3</sub> Electrolyte .....   | 31 |
| C. Preparation of Electrodes .....  | 31 |
| 1. Substrates .....   | 31 |
| 2. Mo:BiVO <sub>4</sub> Electrodes .....  | 31 |
| 3. Ordered TiO <sub>2</sub> /Mo:BiVO <sub>4</sub> Electrodes .....  | 32 |
| 4. Disordered TiO <sub>2</sub> / Mo:BiVO <sub>4</sub> Electrodes .....  | 34 |
| 5. Nanocrystalline - TiO <sub>2</sub> /Mo:BiVO <sub>4</sub> Electrodes .....  | 34 |
| 6. NaCl-treated/ Mo:BiVO <sub>4</sub> Electrodes .....  | 35 |
| 7. Backgrounds i-TiO <sub>2</sub> -o, i-TiO <sub>2</sub> -g and nc-TiO <sub>2</sub> Electrodes .....  | 35 |
| D. Photodeposition.....   | 36 |
| 1. Preparation of Ni(NO <sub>3</sub> ) <sub>2</sub> Solution .....  | 36 |
| 2. Photodeposition of Ni-B <sub>i</sub> /Mo:BiVO <sub>4</sub> Electrodes .....  | 36 |
| 3. Photodeposition of Ni-B <sub>i</sub> /TiO <sub>2</sub> /Mo:BiVO <sub>4</sub> electrodes.....   | 36 |
| E. Photoelectrochemical Measurements .....  | 37 |
| 1. Photoelectrochemical Setup.....  | 37 |
| 2. Cyclic Voltammetry .....   | 38 |
| 3. Incident Photon to Current Conversion Efficiency (%IPCE) .....   | 38 |
| 4. Backwall Vs. Front Wall Measurements .....   | 39 |
| 5. SEM Imaging, EDX, XRD , UV-Vis and Profilometry .....  | 40 |
| <br>  |    |
| INVESTIGATION OF THE EFFECTS OF LIGHT<br>HARVESTING OF COUPLED AT Mo:BiVO <sub>4</sub> PHOTOANODE<br>TO TiO <sub>2</sub> PHOTONIC CRYSTALS IN THE PRESENCE OF<br>HOLE SCAVENGER IN SULFATE SULFITE ELECTROLYTE<br>..... | 42 |

|   |    |
|---|----|
| A. Mo:BiVO <sub>4</sub> Photoanodes of Different Thickness .....  | 43 |
| 1. Characterization of Mo:BiVO <sub>4</sub> Photoanodes .....   | 43 |
| 2. Investigation of the Effect of Molybdenum doping of BiVO <sub>4</sub> Photoanode on the Photoelectrochemical Behavior .....  | 45 |
| B. Ordered TiO <sub>2</sub> Inverse Opals (282 nm sphere size) Coupled to Different Thickness of Mo:BiVO <sub>4</sub> Photoanodes .....   | 46 |
| 1. UV-Vis Absorption Spectra of Mo:BiVO <sub>4</sub> and Bilayer 282-i-TiO <sub>2</sub> -o/Mo:BiVO <sub>4</sub> .....   | 46 |
| 2. SEM Characterization of Bilayer 282-i-TiO <sub>2</sub> -o/Mo:BiVO <sub>4</sub> of Different Thicknesses .....  | 48 |
| 3. Investigation of Photoelectrochemical Behavior of 282-i-TiO <sub>2</sub> -o of different thickness Coupled to different thickness of Mo:BiVO <sub>4</sub> Electrodes.....                        | 51 |
| 4. The Effect of 282-i-TiO <sub>2</sub> -o on the Photoelectrochemical Behavior .....   | 57 |
| C. Disordered TiO <sub>2</sub> Inverse Glass as Photonic Crystals Coupled to Mo:BiVO <sub>4</sub> Photoanode Using the Same Air Hole Size (282 nm) .....  | 59 |
| 1. UV-Vis Absorption Spectra of Bilayer 282-i-TiO <sub>2</sub> -g/Mo:BiVO <sub>4</sub> .....  | 59 |
| 2. Characterization of PG <sub>282</sub> /Mo:BiVO <sub>4</sub> and Bilayer 282-i-TiO <sub>2</sub> -g/Mo:BiVO <sub>4</sub> ....  | 60 |
| 3. Investigation of Photoelectrochemical Behavior of 282nm Sphere Size Inverse Glass TiO <sub>2</sub> Coupled to Mo:BiVO <sub>4</sub> .....   | 61 |
| 4. The Effect of 282-i-TiO <sub>2</sub> -g on the Photoelectrochemical Behavior .....   | 64 |
| 5. NaCl Control Test: Mo:BiVO <sub>4</sub> subjected to NaCl Treatment .....  | 65 |
| D. Mo:BiVO <sub>4</sub> Photoanodes Coupled to Nanocrystalline TiO <sub>2</sub> films.....  | 68 |
| 1. UV-Vis Absorption Spectra of Bilayer nc-TiO <sub>2</sub> /Mo:BiVO <sub>4</sub> .....   | 68 |
| 2. Characterization of Bilayer nc-TiO <sub>2</sub> /Mo:BiVO <sub>4</sub> .....  | 69 |
| 3. Investigation of Photoelectrochemical Behavior of Nanocrystalline TiO <sub>2</sub> Coupled to Mo:BiVO <sub>4</sub> electrodes.....   | 69 |
| 4. The Effect of nc-TiO <sub>2</sub> on the Photoelectrochemical Behavior .....   | 71 |
| E. Mo:BiVO <sub>4</sub> Coupled to Ordered TiO <sub>2</sub> of Varied Stop Band .....   | 73 |
| 1. UV-Vis Absorption Spectra of 150 nm , 227 nm , 305 Sphere Size Inverse Opals Coupled to Mo:BiVO <sub>4</sub> .....   | 73 |
| 2. SEM and EDX Characterization of Bilayer 305-i-TiO <sub>2</sub> -o/Mo:BiVO <sub>4</sub> , 227-i-TiO <sub>2</sub> -o/Mo:BiVO <sub>4</sub> and 150-i-TiO <sub>2</sub> -o/Mo:BiVO <sub>4</sub> ..... | 75 |

|   |            |
|---|------------|
| 3. Investigation of Photoelectrochemical Behavior of 305nm , 227nm and 150 nm Sphere Size TiO <sub>2</sub> Inverse Opals Coupled to Mo:BiVO <sub>4</sub> electrodes .....       | 77         |
| D. Conclusions.....   | 85         |
| <b>INVESTIGATION OF OER CATALYSIS AT Ni-B<sub>i</sub> ON THE Mo:BiVO<sub>4</sub> PHOTOANODE COUPLED TO TiO<sub>2</sub> PHOTONIC CRYSTAL IN POTASSIUM BORATE ELCTROLYTE.....</b> | <b>89</b>  |
| A. Effect of Ni-B <sub>i</sub> OER Co-Catalyst on the Mo:BiVO <sub>4</sub> Photoanode Coupled to TiO <sub>2</sub> Photonic Crystal.....   | 90         |
| 1. Characterization of Ni-B <sub>i</sub> /282-i-TiO <sub>2</sub> -o/Mo:BiVO <sub>4</sub> electrode .....  | 90         |
| 2. Photoelectrochemical Behavior of 282-i-TiO <sub>2</sub> -o/Mo:BiVO <sub>4</sub> Photoanode before and after Ni-B <sub>i</sub> Photodeposition.....                           | 91         |
| 3. The Effect of 282-i-TiO <sub>2</sub> -o on the Photoelectrochemical Behavior Before and After Ni-B <sub>i</sub> Photodeposition .....  | 96         |
| B. Effect of Ni-B <sub>i</sub> OER Co-Catalyst on the Mo:BiVO <sub>4</sub> Photoanode .....   | 99         |
| 1. Characterization of Ni-B <sub>i</sub> /Mo:BiVO <sub>4</sub> electrode.....   | 99         |
| 2. The Photoelectrochemical Behavior of Mo:BiVO <sub>4</sub> Photoanode before and after Ni-B <sub>i</sub> Bilayer Photodeposition .....  | 100        |
| 3- Effect of Ni-B <sub>i</sub> Photodeposition on Cast Mo:BiVO <sub>4</sub> on the Photoelectrochemical Behavior.....   | 105        |
| C. Conclusions .....  | 108        |
| <b>Conclusion .....</b>   | <b>109</b> |
| <b>REFERENCES .....</b>   | <b>113</b> |

# ILLUSTRATIONS

## Figure

1. Schematic diagram of the photoelectrochemical cell demonstrating a photocatalytic water splitting..... 14
2. The energy bands and Fermi level of an intrinsic and extrinsic semiconductors: n-type and p-type. .... 17
3. Junction formation between n-type semiconductor and a solution with redox couple O/R under light irradiation. <sup>17</sup> ..... 18
4. Current potential curve of n-type semiconductor under light irradiation. <sup>17</sup> ..... 18
5. Schematic diagram of Mo:BiVO<sub>4</sub> electrode/Electrolyte/Pt junction. .... 20
6. The difference in the distance traveled by the photogenerated electrons and hole pairs under front and back illumination conditions. .... 21
7. Scheme showing single scattering particle forming ordered and disordered packing. .... 22
8. Scheme represents the stopband of the 282-i-TiO<sub>2</sub>-o/Mo:BiVO<sub>4</sub> at 573 nm and the blue circle shows the blue edge of stop band and the red circle shows the red edge of the stopband. .... 23
9. Scheme of charge transfer processes in TiO<sub>2</sub>/BiVO<sub>4</sub> electrode under visible light irradiation. .... 26
10. Scheme of Ni-B<sub>i</sub> catalyzed photoelectrochemical water oxidation of Mo:BiVO<sub>4</sub> photoanode. .... 28
11. Scheme of i-TiO<sub>2</sub>-o / Mo:BiVO<sub>4</sub> with varying stop bands were fabricated via liquid phase deposition by replication of polystyrene (PS) opals assembled from different sphere sizes on top of Mo:BiVO<sub>4</sub> layer. .... 33
12. Scheme of the difference in preparation between ordered photonic crystals (PC) and disordered photonic glass (PG) ..... 34
13. Scheme showing steps of squeegee method for preparing the nc-TiO<sub>2</sub>/Mo:BiVO<sub>4</sub> FTO samples. .... 35
14. Scheme of the photodeposition of Ni-B<sub>i</sub> on TiO<sub>2</sub>/Mo:BiVO<sub>4</sub> where the procedures start from the steps shown in scheme 14. .... 37
15. Schematic diagram for monochromatic %IPCE measurement setup (back side illumination ) for Mo:BiVO<sub>4</sub> sample as working electrode (WE) versus Ag/AgCl as a reference electrode (RE) and Pt wire as a counter electrode (CE). .... 39
16. Scheme showing the front and back illumination of i-TiO<sub>2</sub>-o/Mo:BiVO<sub>4</sub> photoelectrode. .... 39

|   |    |
|---|----|
| 17. SEM images of Mo:BiVO <sub>4</sub> of different thickness ( A: $0.467 \pm 0.110 \mu\text{m}$ , B: $0.615 \pm 0.131 \mu\text{m}$ , C: $0.663 \pm 0.129 \mu\text{m}$ ) with D: EDX spectrum of Mo:BiVO <sub>4</sub> .....   | 43 |
| 18. XRD of Mo:BiVO <sub>4</sub> .....   | 45 |
| 19. I-V curves at BiVO <sub>4</sub> and Mo:BiVO <sub>4</sub> photoanodes in the dark and upon back and front light illumination in 1M KBi electrolyte (pH = 9.2). The scan rate is 10 mV/s.....   | 46 |
| 20. UV-Vis absorption spectra of (A) Mo:BiVO <sub>4</sub> , (B) bilayer 282-i-TiO <sub>2</sub> -o/20 $\mu\text{l}$ Mo:BiVO <sub>4</sub> , (C) 282-i-TiO <sub>2</sub> -o/40 $\mu\text{l}$ Mo:BiVO <sub>4</sub> and (D) 282-i-TiO <sub>2</sub> -o/20 $\mu\text{l}$ cast Mo:BiVO <sub>4</sub> .....  | 48 |
| 21. SEM images of (A) bilayer 282-i-TiO <sub>2</sub> -o/Mo:BiVO <sub>4</sub> of thickness ( $2.11 \pm 0.407 \mu\text{m}$ ), (B) inverse opal structures of 282 sphere size with average air-hole diameter $0.21 \pm 0.12 \mu\text{m}$ respectively and with (C) its EDX. ....   | 50 |
| 22. SEM images of bilayer 282-i-TiO <sub>2</sub> -o/Mo:BiVO <sub>4</sub> of different thickness ( A: $2.63 \pm 0.77 \mu\text{m}$ , B: $3.99 \pm 1.07 \mu\text{m}$ ) and with their EDX spectra (C and D) respectively. ....   | 51 |
| 23. %IPCE at 0.6 V vs Ag/AgCl of (A) average and best film (highest %IPCE) bilayer 282-i-TiO <sub>2</sub> -o/ 20 $\mu\text{l}$ Mo:BiVO <sub>4</sub> with the best film (B) I-V curves in the dark and back light illumination at 100 mW/cm <sup>2</sup> intensity of a scan rate 10 mV/s. Electrolyte solution is 0.5 M Na <sub>2</sub> SO <sub>4</sub> in 0.1 M Na <sub>2</sub> SO <sub>3</sub> solution (pH ~ 9.63). ....   | 53 |
| 24. %IPCE at 0.6 V vs Ag/AgCl of (A) average and best film (highest %IPCE) bilayer 282-i-TiO <sub>2</sub> -o/ 40 $\mu\text{l}$ Mo:BiVO <sub>4</sub> , (B) average and best film (highest %IPCE) bilayer 282-i-TiO <sub>2</sub> -o/ 20 $\mu\text{l}$ cast Mo:BiVO <sub>4</sub> with their best film I-V curves ( C and D) respectively in the dark and back light illumination at 100 mW/cm <sup>2</sup> intensity of a scan rate 10 mV/s. Electrolyte solution is 0.5 M Na <sub>2</sub> SO <sub>4</sub> in 0.1 M Na <sub>2</sub> SO <sub>3</sub> solution (pH ~ 9.63). .... | 55 |
| 25. I-V curves of (A) 282-i-TiO <sub>2</sub> -o in dark and upon light under front and back illumination of 10mV/s scan rate with their (B) %IPCE vs wavelength (nm) at 0.6 V vs Ag/AgCl in 0.5 M Na <sub>2</sub> SO <sub>4</sub> in 0.1 M Na <sub>2</sub> SO <sub>3</sub> solution (pH ~ 9.63). ....   | 57 |
| 26. UV-vis absorption spectra of (a) PG <sub>282</sub> / Mo:BiVO <sub>4</sub> , and (b) bilayer 282-i-TiO <sub>2</sub> -g/Mo:BiVO <sub>4</sub> .....  | 60 |
| 27. SEM images of (A) PG <sub>282</sub> /Mo:BiVO <sub>4</sub> ( $4.72 \pm 2.89\mu\text{m}$ ) and (B) bilayer 282-i-TiO <sub>2</sub> -g/Mo:BiVO <sub>4</sub> ( $3.99 \pm 2.65 \mu\text{m}$ ), and with their EDX spectra (C and D) respectively .....  | 61 |
| 28. %IPCE vs wavelength (nm) at 0.6 V vs Ag/AgCl of (A) average and best film ( highest %IPCE ) bilayer 282-i-TiO <sub>2</sub> -g/ Mo:BiVO <sub>4</sub> , (C) average and best film (highest %IPCE ) 282-i-TiO <sub>2</sub> -g with their best cyclic voltammograms (B) and (D) respectively in dark and upon light under back illumination for (A,B,C and  |    |

|  |    |
|--|----|
| D) and front illumination (C and D) in 0.5 M Na <sub>2</sub> SO <sub>4</sub> in 0.1 M Na <sub>2</sub> SO <sub>3</sub> solution (pH ~ 9.63). The scan rate is 10 mV/s.....  | 63 |
| 29. UV-Vis absorption spectra (A) of NaCl-treated/Mo:BiVO <sub>4</sub> , %IPCE at 0.6 V vs Ag/AgCl of (B) average and best film (highest %IPCE) bilayer NaCl-treated/Mo:BiVO <sub>4</sub> with its best film (B) I-V curves in the dark and back light illumination at 100 mW/cm <sup>2</sup> intensity of a scan rate 10 mV/s. Electrolyte solution is 0.5 M Na <sub>2</sub> SO <sub>4</sub> in 0.1 M Na <sub>2</sub> SO <sub>3</sub> solution (pH ~ 9.63). ..... | 67 |
| 30. UV-vis absorption spectra of bilayer nc-TiO <sub>2</sub> /Mo:BiVO <sub>4</sub> .....   | 68 |
| 31. SEM images of (A) bilayer nc-TiO <sub>2</sub> /Mo:BiVO <sub>4</sub> (1.57 ± 0.77 μm) with (B) its EDX spectrum.....  | 69 |
| 32. %IPCE at 0.6 V vs Ag/AgCl of (A) average and best film (highest %IPCE) bilayer nc-TiO <sub>2</sub> / Mo:BiVO <sub>4</sub> with its best film (B) I-V curves in the dark and back light illumination at 100 mW/cm <sup>2</sup> intensity of a scan rate 10 mV/s. Electrolyte solution is 0.5 M Na <sub>2</sub> SO <sub>4</sub> in 0.1 M Na <sub>2</sub> SO <sub>3</sub> solution (pH ~ 9.63)...   | 70 |
| 33. %IPCE at 0.6 V vs Ag/AgCl of (A) average and best film (highest %IPCE) nc-TiO <sub>2</sub> with its best film (B) I-V curves in the dark and back light illumination at 100 mW/cm <sup>2</sup> intensity of a scan rate 10 mV/s. Electrolyte solution is 0.5 M Na <sub>2</sub> SO <sub>4</sub> in 0.1 M Na <sub>2</sub> SO <sub>3</sub> solution (pH ~ 9.63). .....  | 71 |
| 34. UV-Vis absorption spectra of (A) 305-i-TiO <sub>2</sub> -o/Mo:BiVO <sub>4</sub> (a) and (b) PC <sub>305</sub> /Mo:BiVO <sub>4</sub> , (B) 227-i-TiO <sub>2</sub> -o/Mo:BiVO <sub>4</sub> (a) and (b) PC <sub>227</sub> /Mo:BiVO <sub>4</sub> and (C) 150-i-TiO <sub>2</sub> -o/Mo:BiVO <sub>4</sub> (a) and (b) PC <sub>150</sub> /Mo:BiVO <sub>4</sub> .....  | 74 |
| 35. SEM images of (A) PC <sub>305</sub> /Mo:BiVO <sub>4</sub> (5.6 ± 2.9 μm), (B) bilayer 305-i-TiO <sub>2</sub> -o/Mo:BiVO <sub>4</sub> (3.6 ± 1.25 μm) with their EDX spectra (D and E) respectively and (C) inverse opal structures of 305 nm sphere size with average air-hole diameter 0.239 ± 0.008 μm.....  | 76 |
| 36. SEM images of (A) bilayer 150-i-TiO <sub>2</sub> -o/Mo:BiVO <sub>4</sub> (5.57 ± 1.28 μm) , and (B) bilayer 227-i-TiO <sub>2</sub> -o/Mo:BiVO <sub>4</sub> (2.40 ± 0.99 μm) and with their EDX spectra (C and D) respectively .....  | 77 |
| 37. %IPCE vs wavelength (nm) at 0.6 V vs Ag/AgCl of (A) average and best film ( highest %IPCE ) bilayer 305-i-TiO <sub>2</sub> -g/ Mo:BiVO <sub>4</sub> , with its best film I-V curves (B) in dark and under back illumination in 0.5 M Na <sub>2</sub> SO <sub>4</sub> in 0.1 M Na <sub>2</sub> SO <sub>3</sub> solution (pH ~ 9.63). The scan rate is 10 mV/s.....  | 78 |
| 38. %IPCE vs wavelength (nm) at 0.6 V vs Ag/AgCl of (A) average and best film (highest %IPCE) bilayer 227-i-TiO <sub>2</sub> -g/Mo:BiVO <sub>4</sub> , with its best film I-V curves (B) in dark and under back illumination in 0.5 M Na <sub>2</sub> SO <sub>4</sub> in 0.1 M Na <sub>2</sub> SO <sub>3</sub> solution (pH ~ 9.63). The scan rate is 10 mV/s.....   | 80 |
| 39. %IPCE vs wavelength (nm) at 0.6 V vs Ag/AgCl of (A) average and best film (highest %IPCE) bilayer 227-i-TiO <sub>2</sub> -g/Mo:BiVO <sub>4</sub> under front illumination, with its best film I-V curves in dark and (B) under back illumination and (C) under   |    |

|   |     |
|---|-----|
| front illumination in 0.5 M Na <sub>2</sub> SO <sub>4</sub> in 0.1 M Na <sub>2</sub> SO <sub>3</sub> solution (pH ~ 9.63). The scan rate is 10 mV/s.....  | 82  |
| 40. %IPCE vs wavelength (nm) at 0.6 V vs Ag/AgCl of (A) average and best film (highest %IPCE) bilayer 150-i-TiO <sub>2</sub> -g/Mo:BiVO <sub>4</sub> , with its best film I-V curves (B) in dark and under back illumination in 0.5 M Na <sub>2</sub> SO <sub>4</sub> in 0.1 M Na <sub>2</sub> SO <sub>3</sub> solution (pH ~ 9.63). The scan rate is 10 mV/s.....          | 84  |
| 41. SEM images of (A) bilayer Ni-B <sub>i</sub> /282-i-TiO <sub>2</sub> -o/Mo:BiVO <sub>4</sub> (2.36 ± 0.74 μm) , (B) inverse opals 282nm TiO <sub>2</sub> / Mo:BiVO <sub>4</sub> , with its EDX spectrum (C).....   | 91  |
| 42. %IPCE at 0.6 V vs Ag/AgCl of (A) Average of Ni-B <sub>i</sub> coupled to bilayer 282-i-TiO <sub>2</sub> -o/Mo:BiVO <sub>4</sub> and (B) best Film of Ni-B <sub>i</sub> coupled to bilayer 282-i-TiO <sub>2</sub> -o/Mo:BiVO <sub>4</sub> . Electrolyte is 1M KB <sub>i</sub> (pH=9.16).....   | 92  |
| 43. Cyclic voltammograms (A) of the best film in %IPCE of 282-i-TiO <sub>2</sub> -o/Mo:BiVO <sub>4</sub> before and after the photodeposition of Ni-B <sub>i</sub> in the dark and with back light illumination at 100 mW/cm <sup>2</sup> intensity along with its (B) linear sweep voltammograms under chopped light irradiation for 3 min . The Scan rate is 10 mV/s..... | 93  |
| 44. Cyclic voltammograms of (A) 282-i-TiO <sub>2</sub> -o in dark and upon light under front and back illumination of 10 mV/s scan rate before and after PD Ni-B <sub>i</sub> , (B) along with linear sweep voltammograms under chopped light irradiation for 3 min and (A) %IPCE vs wavelength (nm) in 1M KB <sub>i</sub> (pH=9.16). .....                                 | 97  |
| 45. SEM images of (A) Ni-B <sub>i</sub> /Mo:BiVO <sub>4</sub> with its EDX spectrum (B).....  | 99  |
| 46. %IPCE at 0.6 V (A) of Mo:BiVO <sub>4</sub> and photodeposition of Ni-B <sub>i</sub> 3 min along with their (B) cyclic voltammograms under dark and light illumination. Electrolyte is 1M KB <sub>i</sub> (pH = 9.18) and scan rate is 10 mV/s .....   | 100 |
| 47. linear sweep voltammograms under chopped light irradiation at the Mo:BiVO <sub>4</sub> photoanode before and after photodeposition of Ni <sup>2+</sup> /KB <sub>i</sub> under 3 min back light illumination. Scan rate is 10 mV/s.....  | 103 |
| 48. Scheme of charge transfer processes in Ni(Fe)-B <sub>i</sub> /i-TiO <sub>2</sub> -o/Mo:BiVO <sub>4</sub> photocatalyst under visible light irradiation. ....  | 105 |
| 49. %IPCE at 0.6 V (A) of Cast Mo:BiVO <sub>4</sub> and photodeposition of Ni-B <sub>i</sub> (0.4mM) along with their (B) cyclic voltammograms under dark and light illumination. Electrolyte is 1M KBi (pH = 9.18) and scan rate is 10 mV/s.....   | 106 |

## TABLES

### Table

1. Current density at 0.6 V of I-V curves of figure 43 A of Ni-B<sub>i</sub>/282-i-TiO<sub>2</sub>-o/Mo:BiVO<sub>4</sub> in 1 M KB<sub>i</sub> electrolyte (pH= 9.16) ..... 95
2. Bias shift in I-V curves of figure 43 A of Ni-B<sub>i</sub>/282-i-TiO<sub>2</sub>-o/Mo:BiVO<sub>4</sub> at 0.2 and 0.5 mA/cm<sup>2</sup> in 1 M KB<sub>i</sub> electrolyte (pH= 9.16)..... 96
3. Current density at 0.6 V of cyclic voltammogram of figure 46 B of Ni-B<sub>i</sub>/Mo:BiVO<sub>4</sub> in 1 M KB<sub>i</sub> Electrolyte (pH= 9.18)..... 101
4. Bias shift of I-V curves of Figure 46 B of Ni-B<sub>i</sub>/ Mo:BiVO<sub>4</sub> at 0.2 and 0.5 mA/cm<sup>2</sup> in 1 M KB<sub>i</sub> Electrolyte (pH= 9.18)..... 103

# CHAPTER I

## INTRODUCTION

The greatest free source of green energy is the sun which provides us on earth within one hour with solar energy sufficient for global energy consumption per year.<sup>1</sup> Through natural photosynthesis, solar energy is harvested by storing light energy in chemical bonds.<sup>2</sup> That inspired researchers towards the need for energy harvesting and storage through mimicking photosynthesis process.<sup>3</sup> One process of artificial photosynthesis is water splitting. Chemists have challenges to improve solar water splitting systems for a better energy conversion to generate hydrogen for energy storage which is the key towards a clean energy.<sup>4</sup>

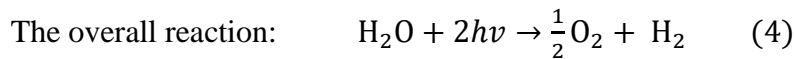
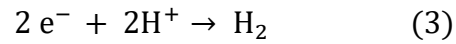
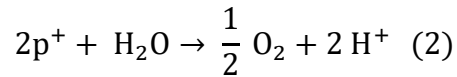
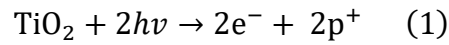
### A. Photoelectrochemical Water Splitting

One of the main solar water splitting system is the photoelectrochemical cell (PEC). It can consists of one semiconductor or of two semiconductors and a metal electrode immersed in an electrolyte.<sup>5</sup> Useful hydrogen fuels through splitting of water to hydrogen and oxygen is produced in PECs.<sup>5</sup> Water splitting is a thermodynamically unfavored reaction (uphill reaction) where Gibbs free energy increases by 237 kJ/mol.<sup>6</sup> It occurs when the energy requirements are met.<sup>7, 8</sup>

Water Splitting:<sup>9</sup> 
$$\text{H}_2\text{O} \rightarrow \text{H}_2 + \frac{1}{2}\text{O}_2$$

Fusjishima and Honda in 1972 were the first to report photocatalytic water splitting in a PEC cell using titanium dioxide ( TiO<sub>2</sub> ) photoanode and platinum (Pt) counter electrode.<sup>10</sup> The steps that take place to produce H<sub>2</sub> and O<sub>2</sub> as shown in Figure 1

in a cell with semiconductor photoanode and a metal cathode and are presented as follows: <sup>10</sup>



Light irradiation on the photoanode generates electron-hole pairs. Then, photogenerated holes on the photoanode surface permits the oxidation of water to produce O<sub>2</sub> and H<sup>+</sup>.<sup>11</sup> After that, an external circuit allows the transfer of photogenerated electrons to the cathode.<sup>11</sup> Finally, the photogenerated electrons on the cathode surface allows reduction of H<sup>+</sup> to produce H<sub>2</sub>.<sup>11</sup> When the energetic requirements are met, water splitting occurs. To overcome the overpotential and other system losses, the practical potential will be much higher than the minimum required potential.<sup>12</sup>

Hydrogen is the most abundant element that exist in both water and biomass with a 122 kJ/g energy yield which is higher than other fuels (gasoline has 40 kJ/g energy yield).<sup>11</sup> Its end use doesn't produce greenhouse gases, pollutants nor harmful effects on the environment, which is why it is considered eco-friendly.<sup>11</sup>

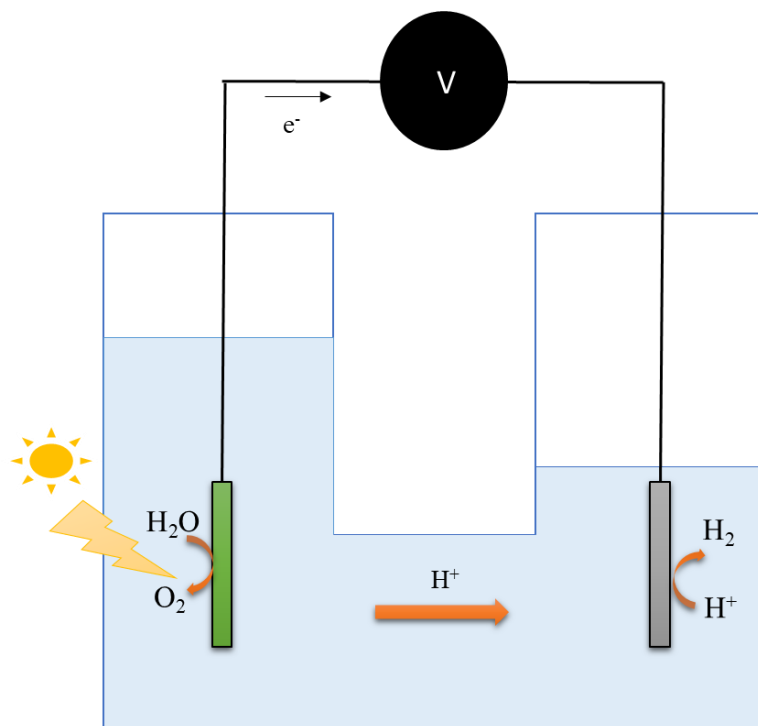
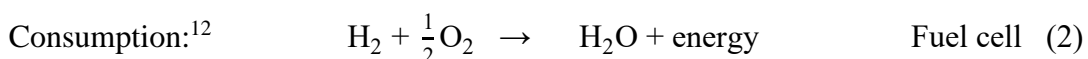
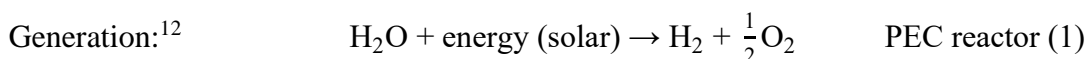


**Figure 1.** Schematic diagram of the photoelectrochemical cell demonstrating a photocatalytic water splitting.<sup>13</sup>

Hydrogen is a clean fuel based energy source and it is an ideal energy carrier when used in a fuel cell by combining it with oxygen producing water and energy.<sup>12</sup>



## B. Oxygen Evolution Reaction

Photoelectrochemical water splitting is made of two main reactions. At the cathode, hydrogen evolution reaction (HER) occurs where the reduction of water occurs to yield hydrogen ( $\text{H}_2$ ).<sup>14</sup> At the anode, oxygen evolution reaction (OER) occurs where the oxidation of water yields oxygen ( $\text{O}_2$ ).<sup>14</sup> The reactions are presented here in alkaline and acidic media:

OER:<sup>14</sup>  $4\text{OH}^- \rightarrow \text{O}_2 + 2\text{H}_2\text{O} + 4\text{e}^-$  ( $E^\circ = -0.40$  V) Alkaline Medium

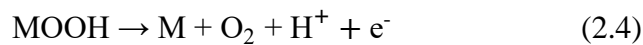
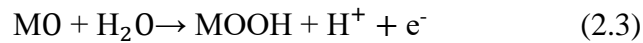
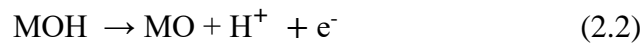
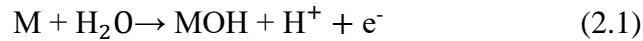
$2\text{H}_2\text{O} \rightarrow \text{O}_2 + 4\text{H}^+ + 4\text{e}^-$  ( $E^\circ = 1.23$  V) Acidic Medium

HER:<sup>14</sup>  $2\text{H}_2\text{O} + 2\text{e}^- \rightarrow \text{H}_2 + 2\text{OH}^-$  ( $E^\circ = -0.83$  V) Alkaline Medium

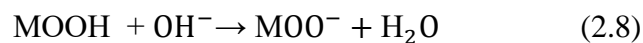
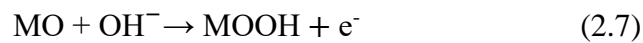
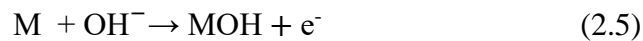
$2\text{H}^+ + 2\text{e}^- \rightarrow \text{H}_2$  ( $E^\circ = 0$  V) Acidic Medium

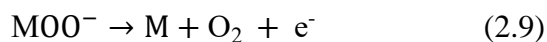
The sluggish kinetics is one of the important reasons which prevent the practical use of these systems.<sup>14</sup> OER consists of a four electron- four proton coupled reaction. A higher overpotential is required for OER to occur to be able to overcome the kinetic barrier. Extensive studies, various photoanodes and catalysts have been designed over the years to improve the stability and electrode kinetics of OER under different electrolyte environments.<sup>14</sup> There are two mechanisms proposed for OER under acidic and alkaline conditions.<sup>15, 16</sup> There are some differences and similarities among these proposed mechanisms as shown in the equations below.<sup>15, 16</sup> The same intermediates such as MOH and MO are noted in the proposed mechanism, but their action towards forming oxygen is the major difference.<sup>15, 16</sup>

Proposed mechanism in acidic medium:<sup>15</sup>



Proposed mechanism in alkaline medium:<sup>16</sup>





The electrocatalyst is used to facilitate chemical reactions including charge transfer. It facilitates charge transfer between the electrode and reactant since it adsorbs reactant on the surface to form the adsorbed intermediate.<sup>14</sup> One of the important electrocatalytic kinetic parameters is the overpotential ( $\eta$ ) required to yield a certain current density.<sup>14</sup> The overpotential is the difference between the applied potential ( $E_{\text{app}}$ ) and the thermodynamic potential of reaction at equilibrium ( $E_{\text{eq}}$ ) required for OER and expressed in eqn (2.10). When a lower overpotential is needed to produce a certain current density, it indicates an active and more efficient electrocatalyst.<sup>14</sup>

$$\eta = E_{\text{app}} - E_{\text{eq}} \quad (2.10)$$

### **C. Semiconductor**

Semiconductors changed the world beyond what could have been imagined. Semiconductors are the building blocks of photovoltaic devices, photoelectrochemical cells, the entire electronics and computer industry.

#### ***1. Types of Semiconductors***

An intrinsic semiconductor's Fermi level referring to the level of energy where the probability of finding an electron is 0.5, lies midpoint between the valence band and conduction band.<sup>17</sup> To increase the number of charge carriers within the semiconducting material, impurity atoms (doping) are added. This results in an extrinsic semiconductor. There are two types of extrinsic semiconductors, p-type and n-type as expressed in figure 2. In a p-type semiconductor, the majority carrier are holes (positive, p) and in n-type semiconductor, the majority carriers are electrons (negative, n).<sup>17</sup> The energy bands

and Fermi levels of an intrinsic and of p-type and n-type semiconductor are shown in Figure 2.

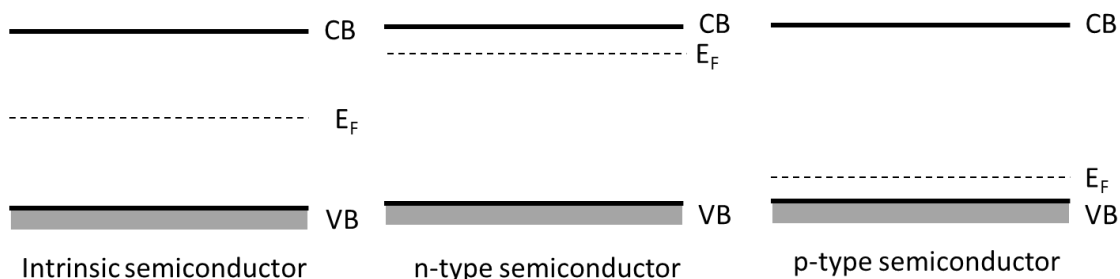


**Figure 2.** The energy bands and Fermi level of an intrinsic and extrinsic semiconductors: n-type and p-type.

## 2. Photoelectrochemistry at Semiconductor/Electrolyte Interface

In a photoelectrochemical cell, a semiconductor/liquid junction forms  $E_{F(\text{semiconductor})} = E_{F(\text{O/R})}$ . Figure 3 shows a junction formation between n-type semiconductor and a solution with a redox couple. The band edges positions are fixed in the semiconductor-solution interface.<sup>18</sup> The bands are bent upward when the semiconductor charge is positive relative to the solution.<sup>18</sup> From the space-charge region, the excess electrons move toward the bulk semiconductor and the excess holes move toward the interface as shown in Figure 3.<sup>18</sup> The electrode potential at which the bands are flat (not bent) is the flat-band potential ( $E_{fb}$ ).<sup>19</sup> In Figure 3, photons are absorbed and electron-hole pairs are created, when the light irradiation energy is greater than  $E_g$ . Separation of electrons and holes are promoted by the space-charge field.<sup>18</sup> Oxidation of R to O is caused by the holes at valence band edge of the semiconductor electrode surface, electrons move into the external circuit.<sup>18</sup> Therefore, a photoanodic current is promoted by the irradiation of an n-type semiconductor electrode and

photooxidation occurs at potentials positive of  $E_{fb}$  which is shown in the  $i$ - $E$  curves in Figure 3. <sup>18</sup>

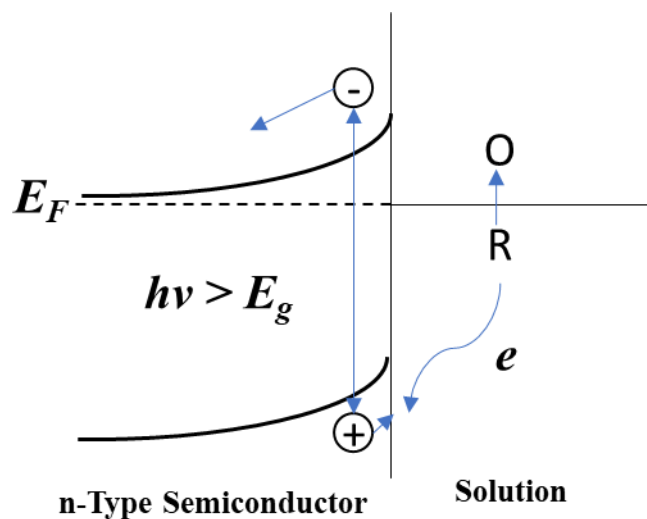


**Figure 3.** Junction formation between n-type semiconductor and a solution with redox couple O/R under light irradiation. <sup>18</sup>

When the potential of the electrode is more positive than  $E_{fb}$ , a photoanodic current ( $i_{pa}$ ) flows since the electron/hole pair separation occurs under irradiation as shown in Figure 4 (b). <sup>18</sup> Near the  $E_{fb}$  is the onset of the photocurrent.

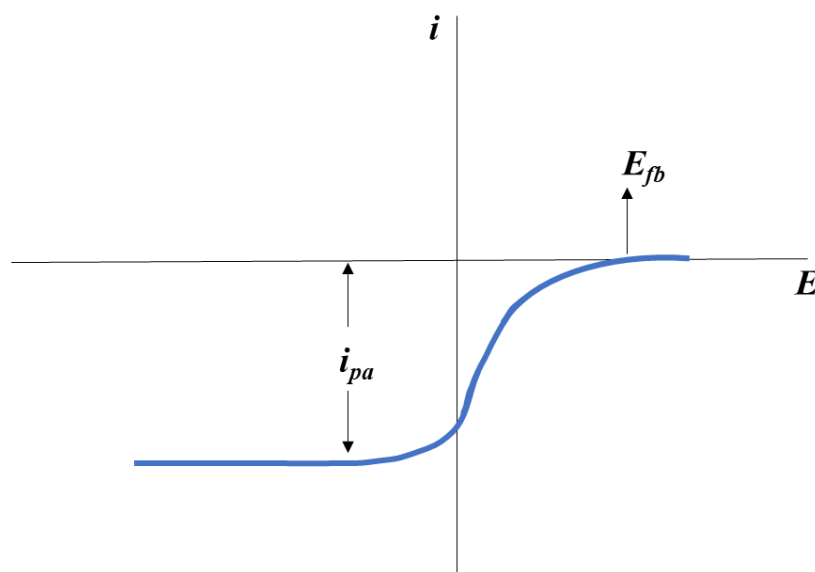


**Figure 4.** Current potential curve of n-type semiconductor under light irradiation. <sup>18</sup>

A photocathodic current and photoreduction is promoted by the irradiation of a p-type semiconductor electrode, where electrons move from the space-charge region to the surface and holes move to the bulk.<sup>18</sup>

#### **D. Mo:BiVO<sub>4</sub> Photoanode**

Researchers have been working to find efficient and stable light absorbing photoelectrodes for oxygen evolution reaction.<sup>20</sup> BiVO<sub>4</sub> has proven to be a promising photoanode, which was first reported for water photooxidation by Kudo and coworkers,<sup>21</sup> because of its moderate band gap (2.4-2.5 eV), suitable valence band position for oxygen evolution, and stability in aqueous solutions.<sup>22</sup> However, it has low efficiency of transport and electrons collection due to the low mobility, and suffers from kinetics limitation for water oxidation.<sup>23</sup> Incorporating elements with a higher oxidation state has been used as a mean to increase electrode conductivity of the n-type BiVO<sub>4</sub>, such as doping BiVO<sub>4</sub> with metals like Tungsten W<sup>24</sup> or Molybdenum Mo.<sup>22</sup> Mo has been reported to improve electronic conductivity and enhance the photoelectrochemical properties of BiVO<sub>4</sub>. Mo or W contribute to increase in conductivity by playing a role of donor dopants.<sup>25</sup> In this thesis, BiVO<sub>4</sub> photoanodes were doped with Mo to enhance its photoelectrochemical behavior.

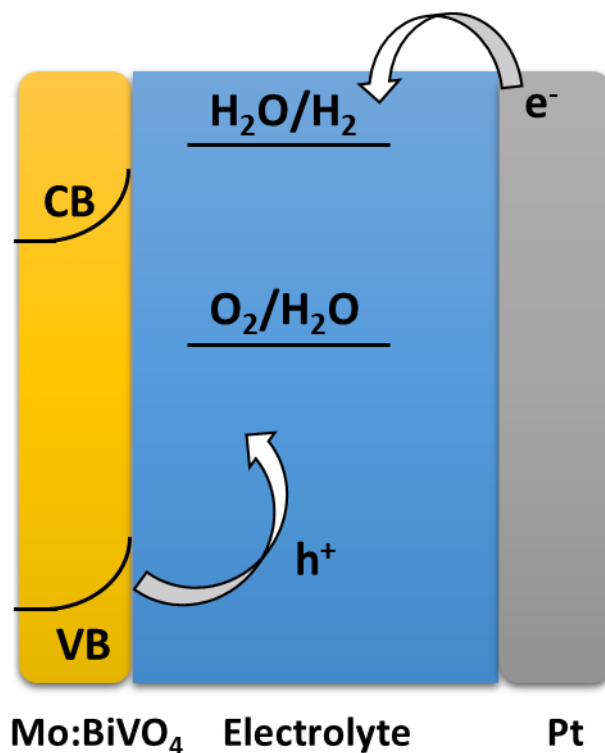


**Figure 5.** Schematic diagram of Mo:BiVO<sub>4</sub> electrode/Electrolyte/Pt junction.

There are some ways to improve Mo:BiVO<sub>4</sub> photoanodes by introducing a heterojunction that enhance charge separation like with TiO<sub>2</sub><sup>26</sup> or WO<sub>3</sub><sup>27</sup> and by decreasing the distance at the solid-liquid interface before separation through nanostructuring.<sup>23</sup>

### **E. The Effect of Illumination Direction on Photoelectrochemical Performance**

The PEC performance of Mo:BiVO<sub>4</sub> can depend on the illumination directions, under front and back illumination conditions presented in Figure 6. At the semiconductor electrolyte interface under front illumination conditions, the electron hole pairs are produced, and the electrons travel to reach the back contact by BiVO<sub>4</sub> matrix as presented in Figure 6 (a). While under back illumination conditions, the

electron hole pairs are produced near the back contact and the holes travel reaching the BiVO<sub>4</sub> electrolyte interface as presented in Figure 6 (b).<sup>28-30</sup>

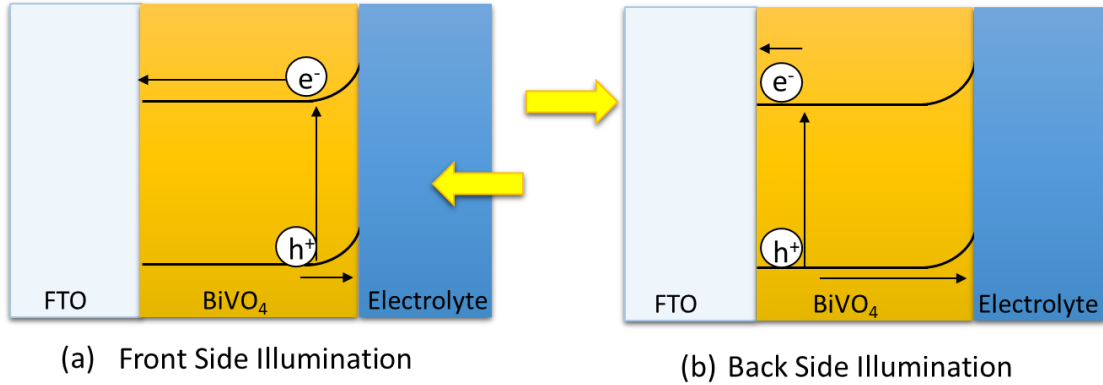


**Figure 6.** The difference in the distance traveled by the photogenerated electrons and hole pairs under front and back illumination conditions.

## F. Photonic Crystals and Photonic Glass

The ordered periodically modulated structures with alternating refractive index where propagation of light may be allowed or forbidden by the photons band structure are called photonic crystals (PC).<sup>31</sup> They can lead to the amplification of light absorbance by slowing certain frequencies of light and aiding in energy conversion.<sup>32</sup> PC is built from dielectric sphere with a size comparable to the wavelength of light leading to a perfectly ordered arrangement. From the same building block it is possible to fabricate a photonic glass (PG), consisting of a completely random arrangement of spheres as shown in Figure 7.<sup>33</sup> This is achieved by adding salt to the assembly medium.<sup>33</sup> One of the properties of photonic crystals is prohibition of propagation of certain wavelengths of light ( photonic band gap).<sup>34</sup> Yablonovitch<sup>35</sup> and John<sup>36</sup> were the first to introduce the band gap concept. They constructed a crystal consisting of periodic array of uniform dielectric which affect the propagation of photons.<sup>37</sup>

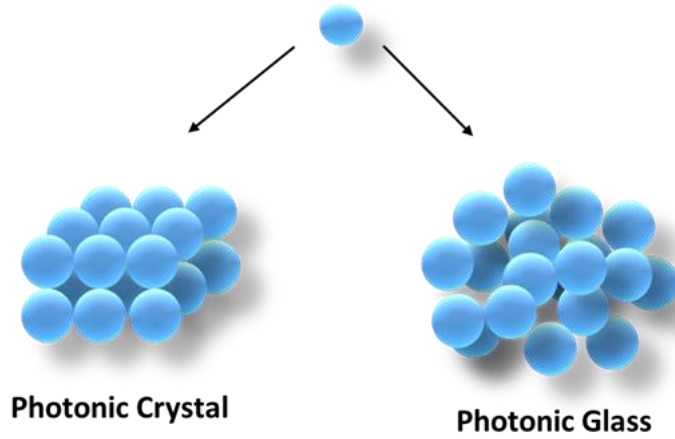


**Figure 7.** Scheme showing single scattering particle forming ordered and disordered packing.

If the photonic crystal refractive index exceed 2.8 using sphere sizes of the order of wavelength of light, the complete band gap becomes possible where radiations are completely reflected when incident from any direction.<sup>38</sup> In this thesis, closed packed face centered cubic (FCC) structures photonic crystal opals having 26% air voids and 74% polystyrene spheres are assembled from polystyrene spheres with refractive index  $n = 1.59$ .<sup>38</sup> The voids of the polystyrene opals were infiltrated with  $\text{TiO}_2$  a high refractive index material ( $n = 2.5$  ; anatase  $n = 2.2$  in the preparation used), followed by calcination of  $\text{TiO}_2$  and the polystyrene spheres to achieve a high refractive index contrast.<sup>38</sup> This will result in  $\text{TiO}_2$  inverse opal (i- $\text{TiO}_2$ -o) with 74 % air voids and 26 %  $\text{TiO}_2$ .<sup>38</sup> According to the Bragg's equation, the wavelength of the center or maximum of the stop band is given by:<sup>38</sup>

$$\lambda = 2D\sqrt{(0.74 \times n_s^2) + (0.26 \times n_v^2)} \quad (6)$$

D is equal to 0.87 times the diameter of the sphere or material filling the void,  $n_s$  and  $n_v$  are the refractive indices of spheres and void or  $\text{TiO}_2$  respectively.<sup>38</sup>

In addition to Bragg reflection within stop band, another property that makes PCs of interest for energy conversion is the slow group velocity of light at the edges of the stop band. <sup>39</sup> Light can be described as a standing wave when approaching the stop band from the long wavelength side. At the blue edge of the stop band, the peaks of this wave are localized in the low dielectric part of photonic crystal, while they are localized in the high electric part on the red edge. <sup>39</sup> An absorber in the high dielectric medium reacts less strongly with light of wavelengths to the blue of the stop band and more strongly with photons having wavelength to the red. <sup>39</sup>

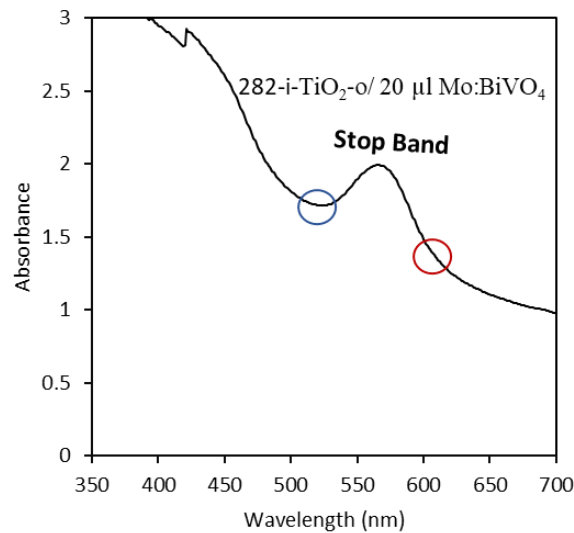


**Figure 8.** Scheme represents the stopband of the 282-i-TiO<sub>2</sub>-o/Mo:BiVO<sub>4</sub> at 573 nm and the blue circle shows the blue edge of stop band and the red circle shows the red edge of the stopband.

### G. Previous Studies of Using Photonic Crystals and Disordered Films to Enhance Light Harvesting

Previous studies have shown significant enhancement when type-II Q-CdTe/CdSe quantum dots were adsorbed on i-TiO<sub>2</sub>-o compared to nc-TiO<sub>2</sub>. <sup>40</sup> Gain was also reported when dye-sensitized nc-TiO<sub>2</sub> was coupled to i-TiO<sub>2</sub>-o. <sup>40</sup> The enhancement

in the absorbance of Ru-N719 dye to the red of the stop band maximum of 486 nm was observed by Nishimura et al. and attributed to slow light at the red edge of the stop band which increase light-matter interaction with the dye localized in the high refractive index region of the photonic crystal.<sup>34</sup> At the blue edge of a TiO<sub>2</sub> (titanium dioxide) inverse opals sensitized Q-CdS in sulfide electrolyte showed a significant enhancement in the conversion of light- to-current as reported by El Harakeh and Halaoui.<sup>41</sup> An enhancement factor of  $4.7 \pm 2.6$  was measured at 420 nm, 30 nm to the blue of the stop band center of a titania inverse opal with stop band centered at 450 nm with Q-CdS with absorption edge at 410 nm.<sup>41</sup> An enhancement in light harvesting by an ultrathin Q-CdTe/Se quantum dot layer sensitized TiO<sub>2</sub> photonic crystal that increased light absorbance in the photonic crystal structure by light trapping was reported by Beydoun et al.<sup>40</sup> i-TiO<sub>2</sub>-o (titanium dioxide inverse opals) sensitized with green-Q-CdTe/CdSe resulted in 4-5 fold enhancement in the overall photon to-current-conversion efficiency where relative to modified nc-TiO<sub>2</sub> (nanocrystalline TiO<sub>2</sub>) 2-fold was attributed to the type-II structure and 2-fold was attributed to light trapping in the photonic crystal.<sup>40</sup>

Halaoui and El Harakeh investigated the disorder effect in inverse opal by sensitizing inverse disordered TiO<sub>2</sub> films (i-TiO<sub>2</sub>-d) by Q-CdS particles.<sup>41</sup> The sensitized photoanode did not exhibit a stop band indicating disorder.<sup>41</sup> An enhancement factor of  $4.8 \pm 2.4$  at 420 nm and  $5.1 \pm 2.5$  at 440 nm relative to nc-TiO<sub>2</sub> was reported.<sup>41</sup> The enhancement measured at the ordered structures at the blue edge of the stop band is similar to the gain observed by the highly disordered structures attributing the gain to multiple internal scattering of light.<sup>41</sup> The disorder effects arising from multiple internal scattering was also studied by Chen et al.<sup>41-44</sup> Using assembled polystyrene spheres of diameters of 150 and 180 nm, and replicating to form titania

inverse opals.<sup>41-44</sup> An enhancement in the photodegradation efficiency of methylene blue adsorbed on the disordered films was observed relative to nanocrystalline TiO<sub>2</sub>, but was less than the inverse opal of 150 nm sphere diameter.<sup>41-44</sup> The disorder in photonic crystal results in internal light scattering.<sup>41-44</sup>

## H. Previous Studies on TiO<sub>2</sub> coupled to BiVO<sub>4</sub>

Lv et al. investigated photocatalytic activity, the formation of an internal heterostructure of BiVO<sub>4</sub> with wide band gap semiconductor was reported to enhance charge separation at BiVO<sub>4</sub>/TiO<sub>2</sub> and reported the photocatalytic enhancement of degradation of rhodamine B (RhB) relative to BiVO<sub>4</sub>/TiO<sub>2</sub>.<sup>45</sup> They attributed the enhancement to the formation of the heterojunction which enabled the photoexcited electrons to transfer to TiO<sub>2</sub>, which promoted charge separation and improved the visible light absorbance.<sup>45</sup> Haifeng Zhang and Chuanwei Cheng fabricated a 3D FTO/TiO<sub>2</sub>/BiVO<sub>4</sub> inverse opals photoanodes through atomic layer deposition of TiO<sub>2</sub> on F:SnO<sub>2</sub> (FTO) inverse opal and electrodeposition of Mo:BiVO<sub>4</sub>.<sup>46</sup> The highest %IPCE at 1.23 V vs RHE equaled 80 % value at 390 nm in the presence of a hole scavenger.<sup>46</sup> The purpose of depositing both TiO<sub>2</sub> and BiVO<sub>4</sub> above F:SnO<sub>2</sub> inverse opal to improve electron transport efficiency. They explained that TiO<sub>2</sub> improves the charge separation efficiency.<sup>46</sup> In Figure 9, the conduction band (CB) of BiVO<sub>4</sub> electrons will be transferred to the CB of TiO<sub>2</sub> because of the heterojunction.<sup>46</sup> These reports show the possibility of electron transfer from CB of BiVO<sub>4</sub> to TiO<sub>2</sub> as shown in Figure 9.

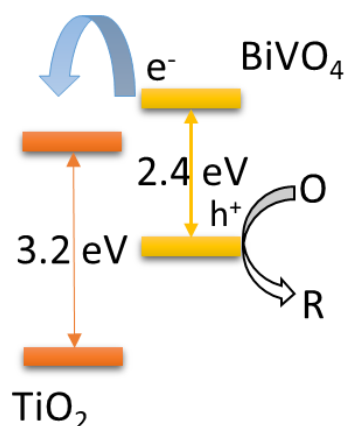


**Figure 9.** Scheme of charge transfer processes in  $\text{TiO}_2/\text{BiVO}_4$  electrode under visible light irradiation.

## I. Oxygen Evolution Catalysts Coupled to $\text{BiVO}_4$ Photoanodes

Introducing oxygen evolution catalysts (OEC) to a photoanode has been shown to have a significant effect on the semiconductor's stability and photocatalytic performance.<sup>22</sup> Research has been focused on finding cheap earth-abundant catalyst for OER, and coupling to photoanodes to enhance the kinetics.<sup>22</sup>

### 1. Ni and Fe-oxo/hydroxide OER Electrocatalysts Coupled to $\text{BiVO}_4$

Ni-oxo/hydroxo based OER catalysts are some of the most efficient non-noble metal catalysts in alkaline and have been coupled to photoanodes and studied in borate electrolyte (pH~ 9) and in KOH electrolyte. Ni-based oxides and layered oxides were used in battery technology and in several applications in engineering, physics and chemistry since 1950s.<sup>47, 48</sup>  $\text{NiO}_x\text{H}_y$  are nickel hydroxides and oxyhydroxides with relative low cost, high activity coupled with stability and abundance, making them promising in alkaline electrolyte as OER catalysts.<sup>14, 49</sup> Their catalytic activity is caused

by the ideal bonding strength of the Ni-OH bond.<sup>14</sup> Ni in Ni(OH)<sub>2</sub> is stable in alkaline medium with oxidation state +2, it oxidizes to +3 or higher with the onset of OER forming NiOOH as expressed in the equation:<sup>49</sup>



The bode diagram shows the transformation in the electrochemical medium. There are two redox couples:  $\alpha$ - Ni(OH)<sub>2</sub>/ $\gamma$ -NiOOH and  $\beta$ -Ni(OH)<sub>2</sub>/ $\beta$ -NiOOH.<sup>48, 50</sup> With aging in alkaline medium, the hydrated disordered  $\alpha$ -Ni(OH)<sub>2</sub> transforms into dehydrated crystalline  $\beta$ -Ni(OH)<sub>2</sub>.<sup>48, 50</sup> With overcharging,  $\beta$ -NiOOH transforms into  $\gamma$ -NiOOH.<sup>51</sup> Water intercalation leads to a significant increase in interlayer distance as transformation from the  $\beta/\beta$  couple to the  $\alpha/\gamma$  couple occurs.<sup>51</sup>

Systematic studies done by Zhang et al. showed that the well-crystallized  $\alpha$ -FeOOH leads to a high efficiency and excellent stability of the  $\alpha$ -FeOOH(P-II)/BiVO<sub>4</sub> photoanode, and resulted in more than 21-fold conversion efficiency compared to pure BiVO<sub>4</sub> photoanode because it facilitates the charge carrier separation and transfer for PEC water splitting.<sup>52</sup> Xiaofon Zhang et al. constructed an ultrathin Nirop modified nanoporous BiVO<sub>4</sub> photoanode (BiVO<sub>4</sub>@Ni:FeOOH).<sup>53</sup> The photocurrent density increased by a factor of 11 compared to pristine BiVO<sub>4</sub> and they indicated that Ni:FeOOH largely decreases the surface recombination rate constant ( $k_{\text{rec}}$ ) rather than increase surface catalysis.<sup>53</sup> Studies showed that Fe inclusion occurs from electrolyte and is the cause of increase of OER activity of Ni-oxo/hydroxide catalysts with activation.<sup>49</sup>

## 2. Ni-B<sub>i</sub> Co-catalyst Coupled to BiVO<sub>4</sub>

Nocera et al. reported a significant OER activity at amorphous electrodeposited Ni-(oxo)/hydroxo films in borate electrolyte (Ni-B<sub>i</sub>).<sup>3</sup> A significant effect on the semiconductor photocatalytic performance has been shown by coupling to oxygen evolution catalysts Co-Pi and Ni-B<sub>i</sub>.<sup>54</sup> Choi *et.al* studied the effects of photodeposition (PD) and electrodeposition (ED) of Ni-B<sub>i</sub> on BiVO<sub>4</sub> photoanodes while varying the deposition time.<sup>55</sup> They reported optimal effects at low deposition times in 0.1 M potassium borate (pH 9.2).<sup>55</sup> A maximum %IPCE 30% was recorded after PD of Ni-B<sub>i</sub> in comparison to 13% at the bare BiVO<sub>4</sub> films at 380.<sup>55</sup> A significant decrease in the produced photocurrent was also noted at very high deposition times.<sup>55</sup>

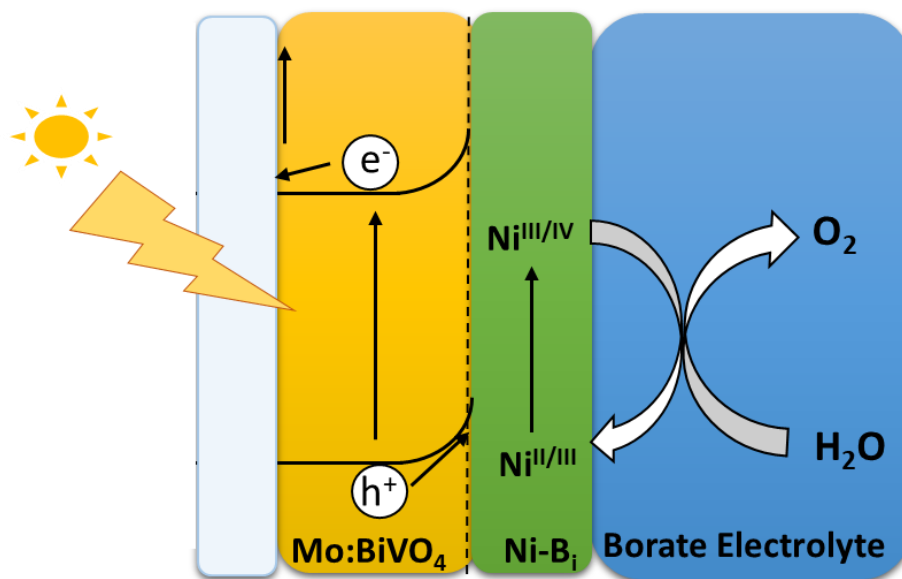


**Figure 10.** Scheme of Ni-B<sub>i</sub> catalyzed photoelectrochemical water oxidation of Mo:BiVO<sub>4</sub> photoanode.

It was reported that Ni-B<sub>i</sub> on BiVO<sub>4</sub> plays a dual role.<sup>55</sup> First, it mediates the hole transfer from BiVO<sub>4</sub> which inhibits the recombination of electron-hole pairs photogenerated at BiVO<sub>4</sub>. This results in a change in the Ni oxidation state from lower

(Ni<sup>2+</sup> and Ni<sup>3+</sup>) to higher states (Ni<sup>3+</sup> and Ni<sup>4+</sup>). The Ni-B<sub>i</sub> catalyzes water oxidation to evolve oxygen which is shown in Figure 10.

## **J. The Work in This Thesis**

In this thesis, the first study aims at coupling Mo-doped BiVO<sub>4</sub> photoanodes of different thickness to TiO<sub>2</sub> photonic crystals of varying stop bands by varying the sphere size from 305, 282, 227 and 150 nm in the opal template to enhance light harvesting in thin films. The effect of coupling to inverse opal is compared to coupling to disordered and non-scattering nanocrystalline TiO<sub>2</sub> films in the presence of hole scavenger (sulfate sulfite electrolyte). This is presented in Chapter 3. The second study focuses on studying the photoelectrochemical behavior of bilayer i-TiO<sub>2</sub>-o/Mo:BiVO<sub>4</sub> modified with Ni-B<sub>i</sub> OER co-catalyst in borate buffer. The effect of the i-TiO<sub>2</sub>-o and Ni-B<sub>i</sub> OER catalyst on water oxidation in borate buffer was compared to the effect of Ni-B<sub>i</sub> on Mo:BiVO<sub>4</sub> photoanodes. This is presented in chapter 4.

## CHAPTER II

### EXPERIMENTAL SECTION

#### A. Materials

Bismuth (III) nitrate pentahydrate  $\text{BiH}_{10}\text{N}_3\text{O}_{14}$  (99,99%, Across), ammonium metavanadate  $\text{NH}_4\text{VO}_3$  (99.5%, Aldrich), ammonium molybdate tetrahydrate  $\text{H}_{32}\text{Mo}_7\text{N}_6\text{O}_{28}$  (Aldrich, %83-81) nitric acid  $\text{HNO}_3$  (65%, Chem-Lab), ethanol  $\text{C}_2\text{H}_6$  (99.8% , Aldrich) were used to prepare the first layer of  $\text{Mo}:\text{BiVO}_4$  electrode. Nickel (II) nitrate hexahydrate  $\text{H}_{12}\text{N}_2\text{NiO}_{12}$  (99.99%, Aldrich) was used for photodeposition of Ni-Bi. Boric acid  $\text{H}_3\text{BO}_3$  (99.8%, Aldrich), sodium sulfate  $\text{Na}_2\text{SO}_4$  (99 -100.5% , Aldrich), sodium sulfite  $\text{Na}_2\text{SO}_3$  (98% , Aldrich), potassium hydroxide  $\text{KOH}$  (85% ,Aldrich) were used to prepare the electrolytes. Carboxylate modified polystyrene (Diameter: 150, 190, 227, 282 and 305 nm nm,ThermoScientific), Igepal  $\text{C}_{25}\text{H}_{44}\text{O}_6$  (Aldrich), titanium (IV) isopropoxide  $\text{C}_{12}\text{H}_{28}\text{O}_4\text{Ti}$  (98+%, Acros) , ammonium hexafluorotitanate  $\text{F}_6\text{H}_8\text{N}_2\text{Ti}$  (99.99%, Aldrich), sodium chloride  $\text{NaCl}$  (Aldrich) Ti - nanoxide T (Solaronix, 10g ) were used to prepare the bilayer  $\text{TiO}_2$  electrodes. Isopropanol  $\text{C}_3\text{H}_8\text{O}$  (99.5%, Aldrich) was used to clean the FTO before any assembly. Deionized water  $\text{H}_2\text{O}$  (resistivity  $\geq 18 \text{ M}\Omega\cdot\text{cm}$ , Nanopure Diamond) was used in all preparations and experiments.

#### B. Preparation of Solutions

##### 1. $\text{KB}_i$ electrolytes

0.1 M  $\text{KB}_i$  was prepared by dissolving 3.0915 g boric acid in 500 mL of deionized water. Similarly, 1 M  $\text{KB}_i$  was prepared using 30.915 g of boric acid in 500

mL of deionized water. In both, the pH was adjusted to ~ 9.2 by the gradual addition of potassium hydroxide (KOH) pellets while stirring to dissolve.

## ***2. Na<sub>2</sub>SO<sub>4</sub> in the presence of Na<sub>2</sub>SO<sub>3</sub> Electrolyte***

The electrolyte of 0.5 M sodium sulfate (Na<sub>2</sub>SO<sub>4</sub>) in the presence of 0.1 M sodium sulfite (Na<sub>2</sub>SO<sub>3</sub>) were prepared by dissolving 3.55g of Na<sub>2</sub>SO<sub>4</sub> and 0.63g of Na<sub>2</sub>SO<sub>3</sub> in 50 ml deionized water (pH ~ 9.63).

## **C. Preparation of Electrodes**

### ***1. Substrates***

Fluorine-doped tin oxide coated glass substrates (FTOs, coated one side, Solaronix,  $R=15 \Omega/\text{sq}$ ) were cut into  $\sim 2 \times 4 \text{ cm}^2$  fragments. They were cleaned by ultrasonication in isopropanol for 30 min followed by sonication of deionized water for 15 min and then placed on a paper towel to dry in air.

### ***2. Mo:BiVO<sub>4</sub> Electrodes***

The Mo:BiVO<sub>4</sub> solution was prepared by dissolving Bi(NO<sub>3</sub>)<sub>3</sub> (0.2425 g), (NH<sub>4</sub>)<sub>6</sub>Mo<sub>7</sub>O<sub>24</sub>·4H<sub>2</sub>O (0.0018 g), and NH<sub>4</sub>VO<sub>3</sub> (0.015 g) in 5 mL deionized water, then 5 mL nitric acid (concentration) was added and diluted with 10 mL ethanol. The solution was stirred for two hours at room temperature. To fabricate the Mo:BiVO<sub>4</sub> electrodes, 20  $\mu\text{L}$  of the solution was cast or cast then spread using the tip of the adjustable pipette for bilayer purpose on the FTO and dried in vacuum at room temperature in a vacuum oven. To achieve films with different thicknesses, the procedure of casting then spreading was repeated multiple times until a total of 20, and

40 $\mu$ L were deposited on different FTOs. The films were placed in furnace oven face up on an ITO glass to be annealed at 500 °C with a ramp rate of 2 °C/min for 3 hours, then removed to cool down to room temperature. The electrode geometric area was defined using a blade and an insulating epoxy resin at 0.25 cm<sup>2</sup>. The width of the film is measured and the corresponding length to reach an area of 0.25 cm<sup>2</sup> is calculated. Resin and hardener (Alteco F-05) epoxy was used where a small portion of the resin is added onto a watch glass and an equally sized portion of the hardener is added next to it. The two were then mixed thoroughly using a plastic spatula to activate the epoxy. The latter was then coated around the defined area and left to dry for a day. The upper portion of the electrode was left uncoated to allow its connection to the potentiostat during photoelectrochemical experiments.

### **3. Ordered TiO<sub>2</sub>/Mo:BiVO<sub>4</sub> Electrodes**

The ordered polystyrene templates were assembled by evaporation induced self-assembly at 55 °C from 150, 227, 282, and 350 nm PS (polystyrene) spheres after the removal of the epoxy using hotplate at 40 °C from the prepared Mo:BiVO<sub>4</sub> electrodes as shown in Figure 11. A solution of 0.17g of Igepal and 0.19 g of polystyrene in 75 ml deionized water was prepared. It is left to sonicate for 40 min until all are homogenized well. Then, the solution is poured into a beaker and the prepared FTOs are placed inside in a vertical way. Afterward, the beaker is placed inside the furnace oven for 48 hours. When the solution is completely evaporated, the films are removed to undergo UV-Vis measurement then undergo infiltration process. Infiltration of the opal template with TiO<sub>2</sub> through a liquid phase deposition as previously reported.<sup>38</sup> A solution of 0.84 g of titanium (IV) isopropoxide in 75 ml ethanol solution was prepared. Then the assembled

electrodes were dipped in the prepared solution for 5 min and left to dry in air for an hour. During this time, two solutions were prepared. The first solution is prepared by adding 1.082 g of boric acid to 35 ml deionized water and the other solution is prepared by adding 2.76 g of ammonium hexafluorotitanate to 35 ml deionized water. They are left to sonicate for 40 min until all solids dissolve. A beaker filled with water is placed on hotplate and thermostat inside to regulate the temperature at 50 °C. When the temperature rises to 50 °C, the two solutions are placed on hotplate at 50°C and a regulator temperature was placed in one of the solutions. When both reach 50°C, they are mixed and the pH is regulated at 2.9 through the addition of 1ml of 1M HCl solution. Then the electrodes are dipped in the solution mixture in the beaker for 30 min and then dipped for 1 min in deionized water. The electrodes are removed and left to dry in air. Then they are calcinations at 400 °C for 8 hrs. to obtain i-TiO<sub>2</sub>-o/Mo:BiVO<sub>4</sub> (inverse opal). And again, the electrode geometric area was defined as explained before. Figure 11 shows all the steps of the preparation procedure.

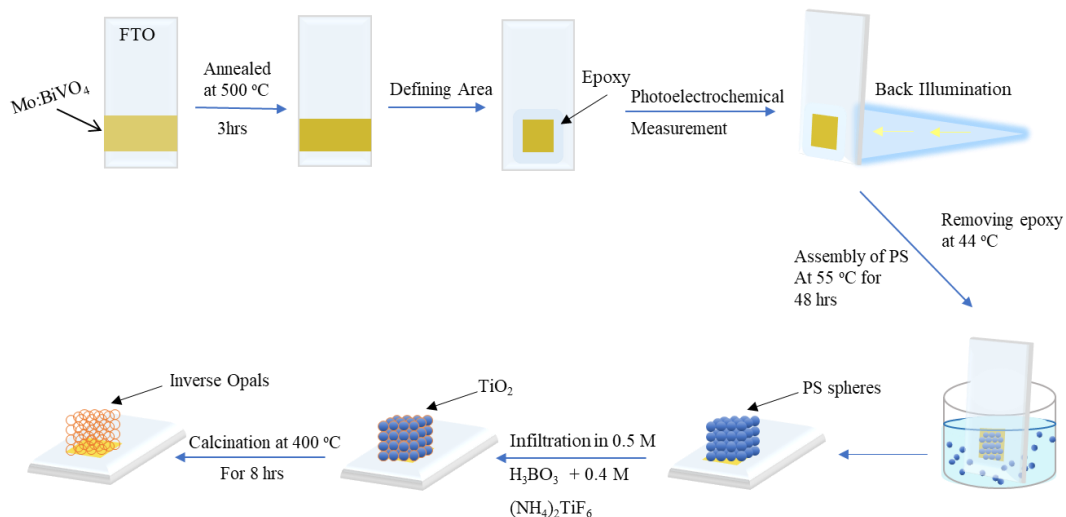


**Figure 11.** Scheme of i-TiO<sub>2</sub>-o / Mo:BiVO<sub>4</sub> with varying stop bands were fabricated via liquid phase deposition by replication of polystyrene (PS) opals assembled from different sphere sizes on top of Mo:BiVO<sub>4</sub> layer.

#### 4. Disordered $\text{TiO}_2/\text{Mo:BiVO}_4$ Electrodes

The disordered polystyrene templates were assembled and infiltrated in the same way as ordered polystyrene templates were prepared however, during assembly NaCl (3.5mM) was added to the 282 nm PS sphere size /Igepal to obtain i- $\text{TiO}_2$ -g/ $\text{Mo:BiVO}_4$  (inverse glass). Figure 12 shows the difference in the preparation of disordered photonic glass and ordered photonic crystals.

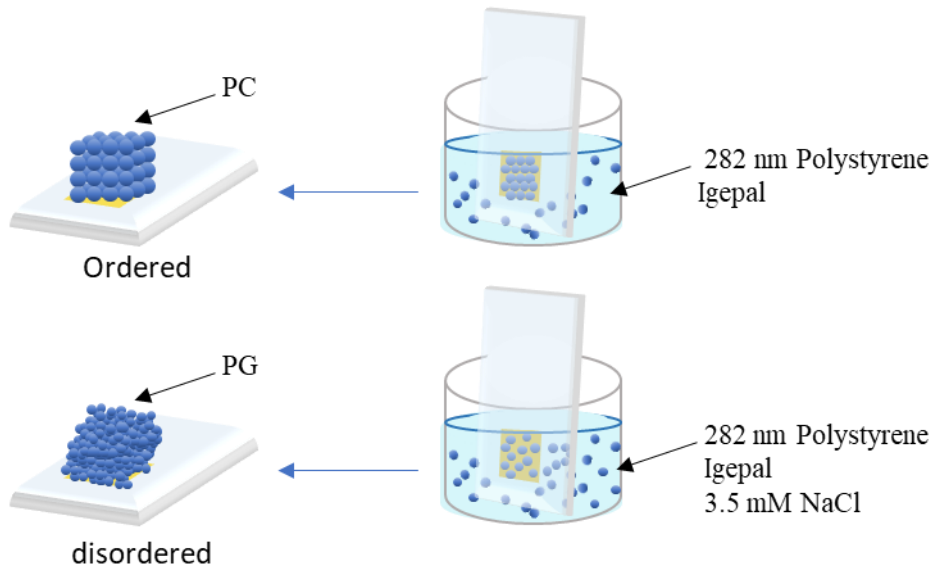
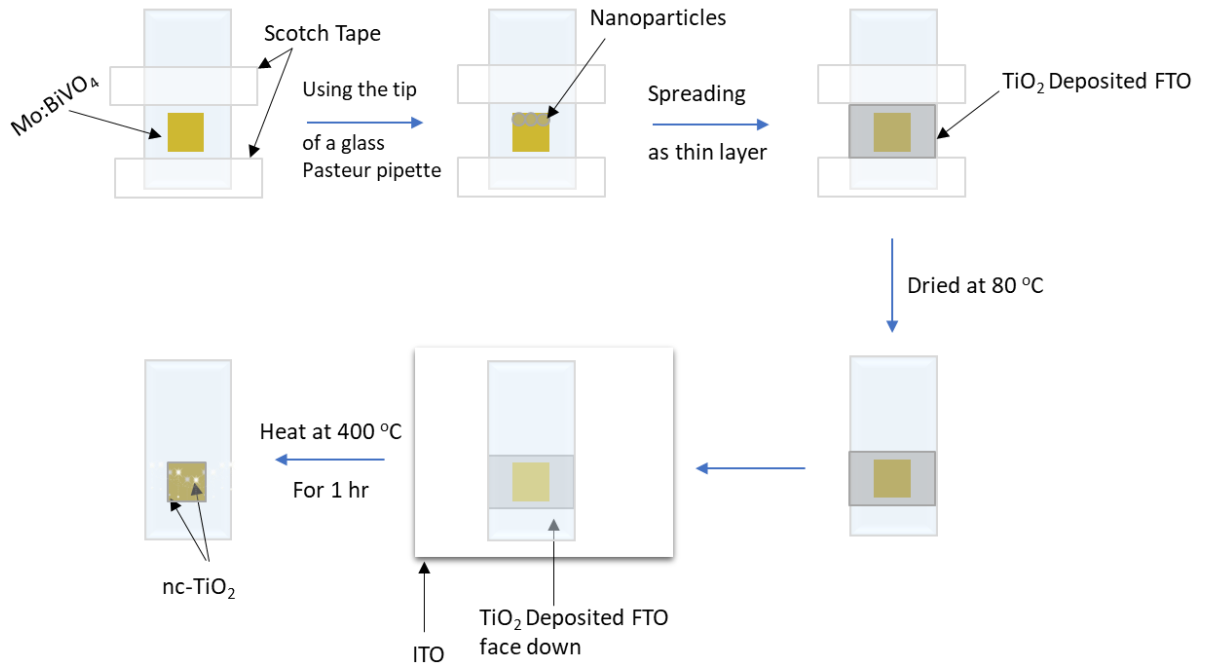


Figure 12. Scheme of the difference in preparation between ordered photonic crystals (PC) and disordered photonic glass (PG)

#### 5. Nanocrystalline - $\text{TiO}_2/\text{Mo:BiVO}_4$ Electrodes

The nanocrystalline  $\text{TiO}_2$  films were deposited using squeegee method by applying Ti - nanoxide T on top of the prepared  $\text{Mo:BiVO}_4$  electrodes. The thickness was controlled using two scotch tape. After the addition of nanoparticles and removal of tape, the solvent was dried at 80 °C on a hot plate for 1 min. The furnace oven is set at 400 °C. Afterwards, when the furnace temperature reaches 400 °C , the samples undergo calcinations at 400 °C for 1 hr by placing them face down on ITO surface and then

followed by cooling at room temperature and using a blade the area defined by 2 cm in width and by 2 cm in length to obtain nc-TiO<sub>2</sub>/Mo:BiVO<sub>4</sub>. This process is shown in Figure 13.



**Figure 13.** Scheme showing steps of squeegee method for preparing the nc-TiO<sub>2</sub>/Mo:BiVO<sub>4</sub> FTO samples.

## 6. NaCl-treated/ Mo:BiVO<sub>4</sub> Electrodes

The same procedures of the disordered TiO<sub>2</sub>/Mo:BiVO<sub>4</sub> was done to prepare NaCl/Mo:BiVO<sub>4</sub> however, in the absence of polystyrene in the assembly.

## 7. Backgrounds *i*-TiO<sub>2</sub>-o, *i*-TiO<sub>2</sub>-g and nc-TiO<sub>2</sub> Electrodes

*i*-TiO<sub>2</sub>-o and *i*-TiO<sub>2</sub>-g electrodes are prepared in the same way as the ordered TiO<sub>2</sub>/Mo:BiVO<sub>4</sub> and disordered TiO<sub>2</sub>/Mo:BiVO<sub>4</sub> electrodes respectively, while without the presence of the Mo:BiVO<sub>4</sub> layer upon assembly or infiltration. nc-TiO<sub>2</sub>

electrodes are prepared in the same way as the nc-TiO<sub>2</sub>/Mo:BiVO<sub>4</sub> without the presence of the Mo:BiVO<sub>4</sub> layer.

## **D. Photodeposition**

### ***1. Preparation of Ni(NO<sub>3</sub>)<sub>2</sub> Solution***

A 0.4 M Ni(NO<sub>3</sub>)<sub>2</sub> solution was prepared by dissolving 0.1163 g of Ni(NO<sub>3</sub>)<sub>2</sub>·6H<sub>2</sub>O in 1 ml deionized water.

### ***2. Photodeposition of Ni-B<sub>i</sub>/Mo:BiVO<sub>4</sub> Electrodes***

The Ni(NO<sub>3</sub>)<sub>2</sub> solution of 0.4 M concentration was freshly diluted to 0.4 mM via the addition of 20 μL of the solution into 20 mL of 0.1 M KB<sub>i</sub> electrolyte (pH ~ 9.20). White light at an intensity of 100 mW/cm<sup>2</sup> was irradiated from a 300-W xenon lamp (model 66901 lamp housing and 68911 power supply, Oriel Instruments) on the Mo:BiVO<sub>4</sub> electrodes for 3 minutes. The electrodes were then rinsed with deionized water to obtain Ni-B<sub>i</sub>/Mo:BiVO<sub>4</sub>.

### ***3. Photodeposition of Ni-B<sub>i</sub>/TiO<sub>2</sub>/Mo:BiVO<sub>4</sub> electrodes***

The TiO<sub>2</sub>/Mo:BiVO<sub>4</sub> electrodes were immersed in 0.1M KB<sub>i</sub> electrolyte (pH ~ 9.2) with 0.4 mM Ni(NO<sub>3</sub>)<sub>2</sub> using the same conditions of PD of Ni-B<sub>i</sub>/Mo:BiVO<sub>4</sub> to obtain Ni-B<sub>i</sub>/TiO<sub>2</sub>/Mo:BiVO<sub>4</sub> as shown in figure 14.

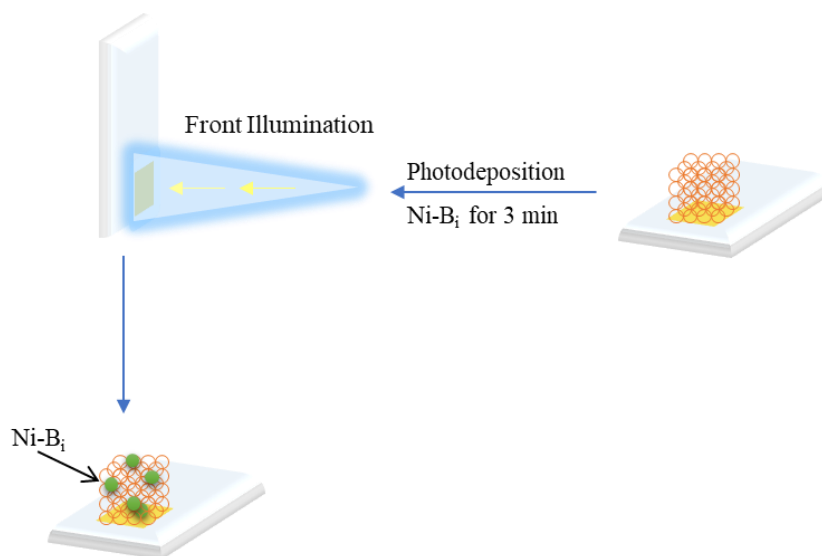


Figure 14. Scheme of the photodeposition of Ni-Bi on  $\text{TiO}_2/\text{Mo:BiVO}_4$  where the procedures start from the steps shown in scheme 14.

## E. Photoelectrochemical Measurements

### 1. Photoelectrochemical Setup

Photoelectrochemical measurements were performed using a CHI model 630A electrochemical workstation (CH instruments) in a 3-electrode quartz photoelectrochemical cell with Pt wire ( $d = 0.5 \text{ mm}$ ) as the counter electrode and Ag/AgCl electrode as the reference electrode (in 3 M KCl solution). The electrolyte used in different measurements was 1 M  $\text{KBi}$  electrolyte solution ( $\text{pH} \sim 9.2$ ) and 0.5 M  $\text{Na}_2\text{SO}_4$  in 0.1 M  $\text{Na}_2\text{SO}_3$  electrolyte ( $\text{pH} \sim 9.63$ ). The electrodes were irradiated by a 300 W xenon lamp during cyclic voltammetry and the sample was position at  $100\text{mW}/\text{cm}^2$ . A monochromator (Oriel Instruments, Model 77200) was used to disperse the light for monochromatic measurements.

## 2. Cyclic Voltammetry

Cyclic voltammograms (CVs) were performed in 1 M  $\text{KB}_i$  and 0.5 M  $\text{Na}_2\text{SO}_4$  in 0.1 M  $\text{Na}_2\text{SO}_3$ . The potential was scanned in the positive direction between -0.9 V and 1.2 V vs. Ag/AgCl. The CVs were acquired at 10 mV/s in dark, back, and front light illumination from 300 W xenon lamp. In the 1M  $\text{KB}_i$ , certain measurements undergo chopped light. The position of the electrode was approximated at  $100 \text{ mW/cm}^2$  mimicking the sunlight intensity on earth and no AM 1.5 filter was used.

## 3. Incident Photon to Current Conversion Efficiency (%IPCE)

The same photoelectrochemical cell was used for incident photon-to-current efficiency (IPCE) measurements. A monochromator (model 77200, Oriel) was attached to another 300 W xenon lamp of the same model as first lamp, and amperometric (i-t) curves were acquired at a potential of 0.6 V vs. Ag/AgCl under chopped light illumination from 300 to 500 nm in 20 nm increments as shown in Figure 15. Chopped light was done manually by moving a 3.16 mm black slit in and out to block and allow light propagation. The photocurrent was calculated by subtracting the dark current from the photocurrent obtained after the illumination of monochromatic light. The photocurrent was measured following united light – on transient after it reached approximately steady-state. The lamp spectrum was measured at the approximate electrode position using a power detector (model 230931, Gentec-eo) of exposed area  $1.13 \text{ cm}^2$  and power meter (model 232838, Gentec-eo). The %IPCE was calculated according to:

$$\% IPCE (at V) = \frac{J_{@V} \left( \frac{A}{\text{cm}^2} \right)}{I_{@ \lambda} \left( \frac{W}{\text{cm}^2} \right)} \times \frac{1240 (eV \cdot \text{nm})}{\lambda (nm)} \times 100$$

where  $J$  is the photocurrent density calculated at different wavelength,  $\lambda$ , at an applied potential  $V$  (0.6 V vs. Ag/AgCl), and  $I$  is the light intensity per  $\text{cm}^2$  measured with the light detector at  $\lambda$ .

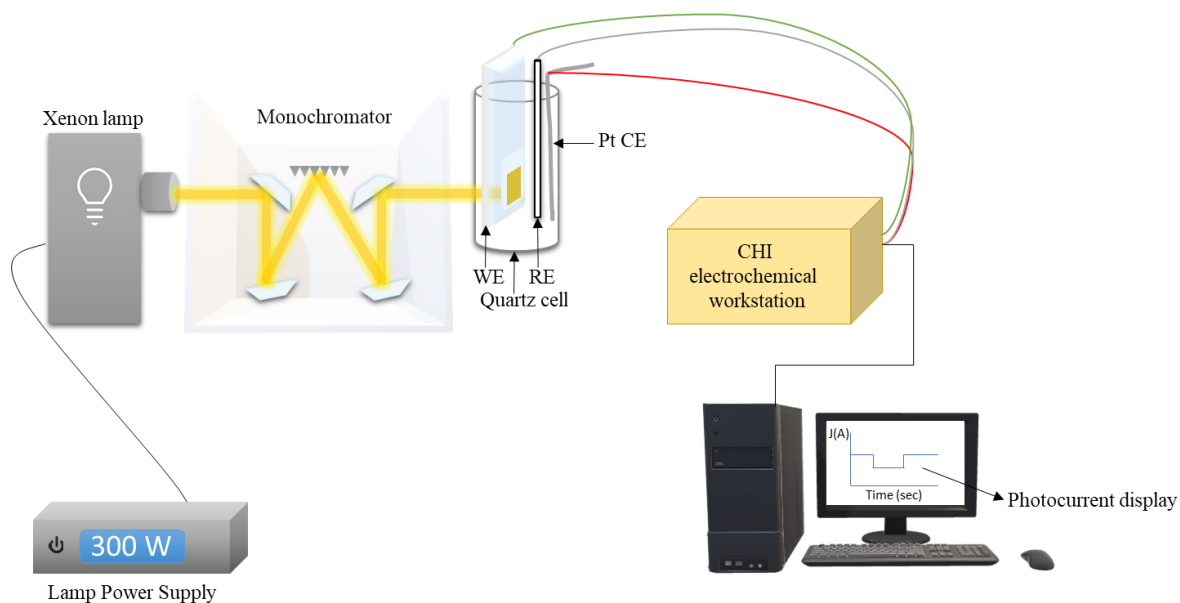


**Figure 15.** Schematic diagram for monochromatic %IPCE measurement setup (back side illumination) for Mo:BiVO<sub>4</sub> sample as working electrode (WE) versus Ag/AgCl as a reference electrode (RE) and Pt wire as a counter electrode (CE).

#### 4. Backwall Vs. Front Wall Measurements

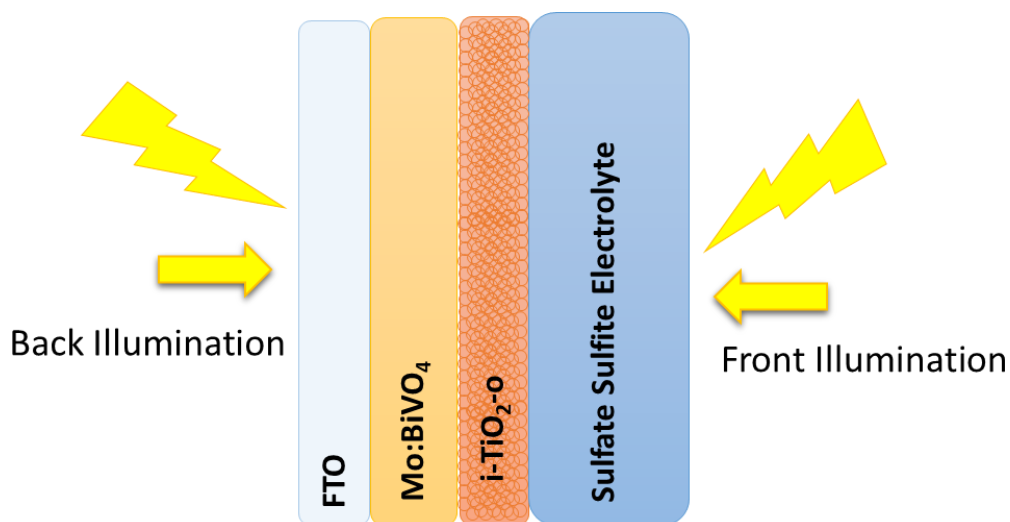


Figure 16. Scheme showing the front and back illumination of i-TiO<sub>2</sub>-o/Mo:BiVO<sub>4</sub> photoelectrode

The films that undergo back illumination shown in Figure 16, the different thickness of Mo:BiVO<sub>4</sub> photoelectrodes, ordered inverse opals of (150, 282, and 305 nm) sphere size TiO<sub>2</sub> bilayer electrodes, nc-TiO<sub>2</sub>/Mo:BiVO<sub>4</sub> electrodes, and NaCl/Mo:BiVO<sub>4</sub> in sulfate sulfite electrolyte in both %IPCE and I-V curves measurements. 282-i-TiO<sub>2</sub>-o/Mo:BiVO<sub>4</sub> before and after Ni-B<sub>i</sub> PD were subjected to back illumination in borate electrolyte in both %IPCE and I-V curves measurements. All backgrounds of 282-i-TiO<sub>2</sub>-o, 282-i-TiO<sub>2</sub>-g, and nc-TiO<sub>2</sub> electrodes undergo both back and front illumination in sulfate sulfite electrolyte, however 282-i-TiO<sub>2</sub>-o before and after Ni-B<sub>i</sub> was done in borate electrolyte in both %IPCE and I-V curves measurements. 227-i-TiO<sub>2</sub>-o/Mo:BiVO<sub>4</sub> undergo both front and back illumination in both %IPCE and I-V curves measurements.

##### ***5. SEM Imaging, EDX, XRD, UV-Vis and Profilometry***

SEM images were taken for Mo-BiVO<sub>4</sub> of different thicknesses, TiO<sub>2</sub> inverse opals and inverse glass bilayer with Mo:BiVO<sub>4</sub> and nc-TiO<sub>2</sub>/Mo:BiVO<sub>4</sub> on FTO using a Tescan MIRA 3 LMU FEG SEM, equipped with a SE detector and an IN-Beam SE detector. A thin layer (7 nm) of Au was sputtered using a Carbon/Metal Coater (Qorum, Q150T ES) on the polystyrene samples for better observation. The bilayer films were scratch using an iron blade single thin line in the middle and tilted to be able to observe better images of the bilayer form. EDX spectra were obtained using an Oxford Instruments X-Max 20 EDX detector running with Oxford INCA software. XRD spectra were acquired for Mo:BiVO<sub>4</sub>, 282-i-TiO<sub>2</sub>-o and 282-i-TiO<sub>2</sub>-o/Mo:BiVO<sub>4</sub> film using a Bruker D8 Advance X-ray diffractometer. UV-Vis Absorption Spectra of the following films: Mo:BiVO<sub>4</sub>, PC/Mo:BiVO<sub>4</sub>, PG/Mo:BiVO<sub>4</sub>, ordered and disordered

TiO<sub>2</sub>/Mo:BiVO<sub>4</sub> , nc-TiO<sub>2</sub>/Mo:BiVO<sub>4</sub>, backgrounds of i-TiO<sub>2</sub>-o, i-TiO<sub>2</sub>-g, nc-TiO<sub>2</sub> were obtained through a UV-Vis/NIR ASCO V-570 machine of serial number CU296670 and a spectra manager software. Before any measurement, the films were rinsed with deionized water and the blank was air. The thickness of all prepared films was obtained by a Bruker Dekta KXT of a step height standard  $860.3 \pm 5.2$  nm using vision 64 software. Each film was measurement from four different sides and then averaged by a standard scan  $6.5\mu\text{m}$  of a  $12.5\mu\text{m}$  stylus radius of 3 mg force for a duration of 300 sec and covered  $300\mu\text{m}$  length.

## CHAPTER III

### INVESTIGATION OF THE EFFECTS OF LIGHT HARVESTING OF COUPLED AT Mo:BiVO<sub>4</sub> PHOTOANODE TO TiO<sub>2</sub> PHOTONIC CRYSTALS IN THE PRESENCE OF HOLE SCAVENGER IN SULFATE SULFITE ELECTROLYTE

BiVO<sub>4</sub> has proven to be a promising photoanode for water oxidation. It was first reported for water photooxidation by Kudo and coworkers.<sup>21</sup> It has a moderate band gap (2.4-2.5 eV), suitable valence band position for oxygen evolution, and it is stable in aqueous solutions.<sup>22</sup> However, it has low efficiency of transport and electrons collection due to the low mobility, and suffers from kinetics limitation for water oxidation.<sup>23</sup>

Incorporating elements with a higher oxidation state has been used as a mean to increase conductivity of the n-type BiVO<sub>4</sub>. Doping it with metals like Tungsten W<sup>24</sup> or Molybdenum Mo was shown to enhance its electronic properties.<sup>22</sup> The PEC of BiVO<sub>4</sub> is hindered because of the poor mobility of its electron majority carrier which would eventually result in relatively short carrier diffusion lengths.<sup>56</sup> BiVO<sub>4</sub> photoanode was doped with Mo in all experiments in this work to improve its electronic properties .

There are some ways to improve Mo:BiVO<sub>4</sub> photoanodes by introducing a heterojunction that enhance charge separation like TiO<sub>2</sub><sup>26</sup> or WO<sub>3</sub><sup>27</sup> and by decreasing the distance at the solid-liquid interface before separation through nanostructuring.<sup>23</sup>

TiO<sub>2</sub> photonic crystals are found to enhance the light harvesting of photoanodes when coupled to BiVO<sub>4</sub>, and this heterostructure enables the transfer of photoexcited electron-hole pairs due to the formation of the heterojunction, the promotion of charge separation and the improvement of visible light absorbance.<sup>45, 46, 57, 58</sup>

In this chapter, we investigated the effect of TiO<sub>2</sub> photonic crystals of varying stop bands on light harvesting at Mo:BiVO<sub>4</sub> films, in a photoelectrochemical cell in the presence of hole scavenger (sulfate sulfite solution) to minimize the kinetics limitations. The stop band was varied by changing the sphere size in the polystyrene opal template and the effect of TiO<sub>2</sub> inverse opal on the light-to-current conversion efficiency of Mo:BiVO<sub>4</sub> was compared to the effect of coupling to disordered inverse glass and non-scattering nanocrystalline TiO<sub>2</sub> films. In the following chapter, the study of water oxidation.

## A. Mo:BiVO<sub>4</sub> Photoanodes of Different Thickness

### 1. Characterization of Mo:BiVO<sub>4</sub> Photoanodes

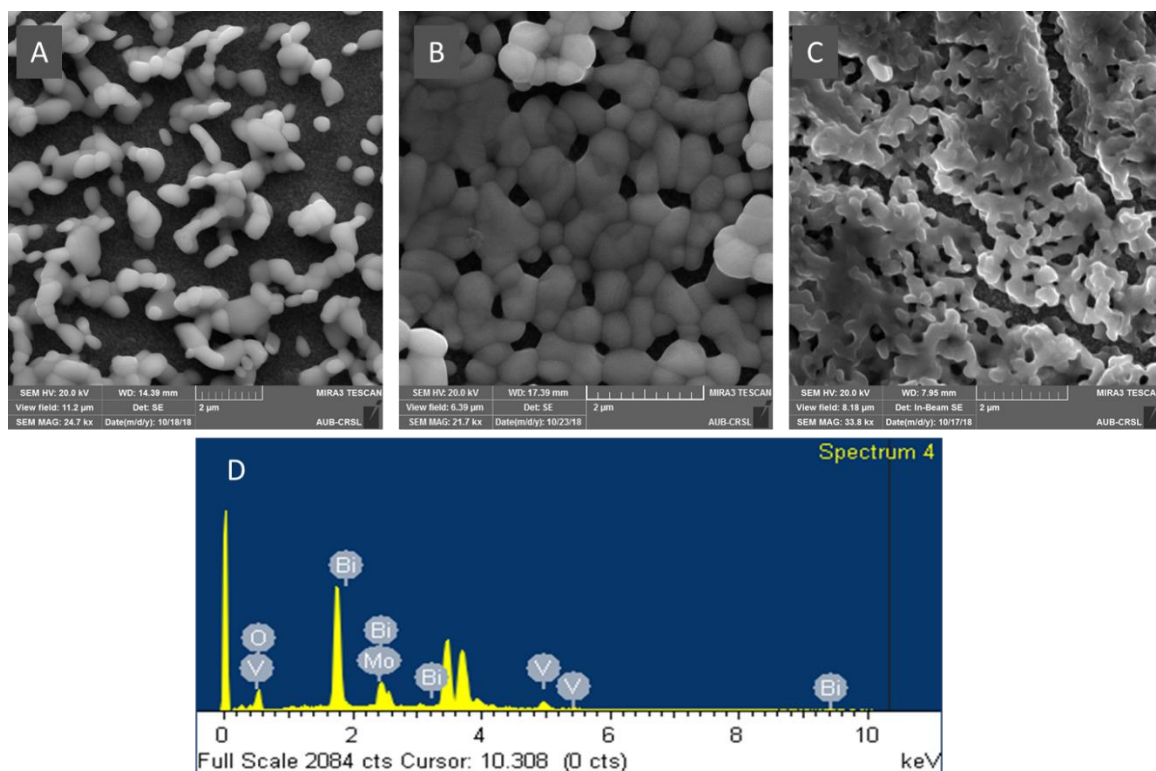


**Figure 17.** SEM images of Mo:BiVO<sub>4</sub> of different thickness ( A:  $0.467 \pm 0.110 \mu\text{m}$  , B:  $0.615 \pm 0.131 \mu\text{m}$  , C:  $0.663 \pm 0.129 \mu\text{m}$ ) with D: EDX spectrum of Mo:BiVO<sub>4</sub>

20 $\mu$ L of Mo:BiVO<sub>4</sub> precursor solution was cast onto an FTO glass, was manually spread and dried in vacuum at room temperature followed by annealing at 500 °C for 2 hours at a ramp rate of 2 °C/min forming Mo:BiVO<sub>4</sub>. The thickness of spread Mo:BiVO<sub>4</sub> shown in Figure 17 A was measured using profilometer. It equals  $0.467 \pm 0.110 \mu\text{m}$  for (N= 4). Figure 17 A shows an SEM image of Mo:BiVO<sub>4</sub> that shows porous uniform coated oval-like nanostructures with smooth surfaces. The EDX spectrum in Figure 17 D identifies the presence of Bi, Mo, V, and O peaks. In Figure 18 the XRD patterns of BiVO<sub>4</sub> single monoclinic phase is shown at (-121) peak sample at  $2\theta = 28.822^\circ$  which was slightly shifted due to compressive lattice strain to  $2\theta = 28.9^\circ$  is a characteristic of Mo:BiVO<sub>4</sub>.<sup>32</sup> A significant peak was observed sample at  $2\theta = 38.2^\circ$  corresponding to the (*hkl*) plane (-211) indicating Mo doping.<sup>32</sup> The  $2\theta$  diffraction peaks appearing  $18.5^\circ$ ,  $29.5^\circ$ , and  $44^\circ$  can be respectively indexed as (110), (121) and (240) planes of monoclinic Mo:BiVO<sub>4</sub> which is consistent with the literature.<sup>59</sup> The Mo:BiVO<sub>4</sub> nanostructured film that look more connected and no spacing in between shown in Figure 17 B was prepared in the same procedure as before but a repetitive cycle of 20  $\mu$ L was deposited for a total 40  $\mu$ L using the piston pipette tip to spread the solution on FTO, reaching a thickness  $0.615 \pm 0.131 \mu\text{m}$  (N=2). A second deposition method was used where the 20  $\mu$ l volume is cast without being spread. The thickness is  $0.663 \pm 0.129 \mu\text{m}$  for (N=2) and the structure of Mo:BiVO<sub>4</sub> became more compact than before as shown in Figure 17 C.

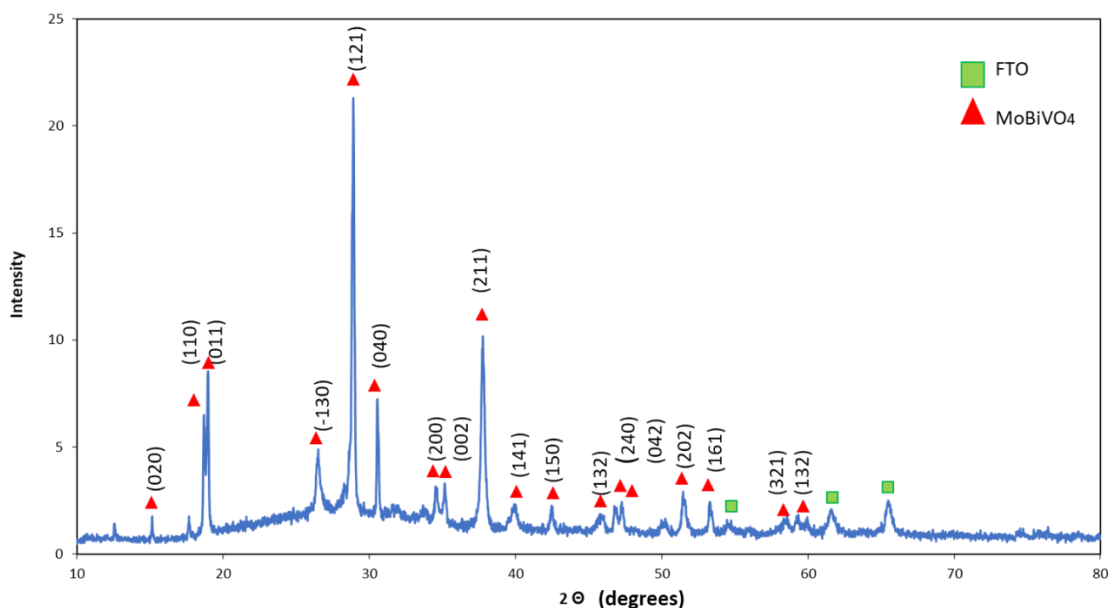


**Figure 18.** XRD of Mo:BiVO<sub>4</sub>.

(Peak assignments were taken from references 58 and 31<sup>59,32</sup>)

## ***2. Investigation of the Effect of Molybdenum doping of BiVO<sub>4</sub> Photoanode on the Photoelectrochemical Behavior***

To understand the photoelectrochemical behavior of the Mo:BiVO<sub>4</sub> photoanode cyclic voltammograms measurements were performed in 1M KB<sub>i</sub> electrolyte. Figure 19 shows the effect of 2% Mo doping on BiVO<sub>4</sub> photoanodes. Comparing the PEC performance of the BiVO<sub>4</sub> and Mo:BiVO<sub>4</sub> photoanodes, the latter showed an enhanced photoactivity. When doped, the film photocurrent was enhanced by a factor of 4.91 in back-wall illumination at 0.6 V vs. Ag/AgCl. When the measurements were done by back illumination, the photocurrent produced is higher than front illumination in both BiVO<sub>4</sub> and Mo:BiVO<sub>4</sub>. The reason is that electron-hole pairs are produced near the back contact in back illumination, while in the front illumination they are produced near the electrode/solution interface resulting in greater recombination.<sup>60</sup> Therefore, in this thesis photoelectrochemical measurements are mainly by back light illumination.

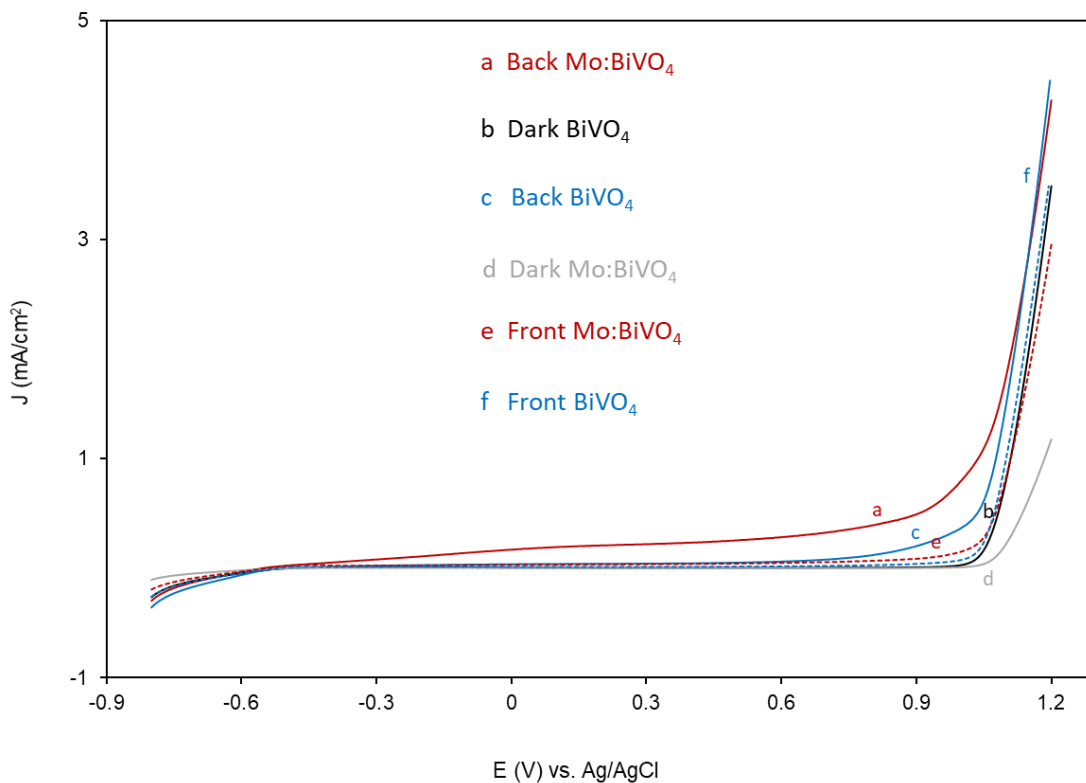


**Figure 19.** I-V curves at BiVO<sub>4</sub> and Mo:BiVO<sub>4</sub> photoanodes in the dark and upon back and front light illumination in 1M KB<sub>1</sub> electrolyte (pH = 9.2). The scan rate is 10 mV/s.

## **B. Ordered TiO<sub>2</sub> Inverse Opals (282 nm sphere size) Coupled to Different**

### **Thickness of Mo:BiVO<sub>4</sub> Photoanodes**

#### ***1. UV-Vis Absorption Spectra of Mo:BiVO<sub>4</sub> and Bilayer 282-i-TiO<sub>2</sub>-o/Mo:BiVO<sub>4</sub>***

In Figure 20 A, the UV-Vis absorption spectrum of Mo:BiVO<sub>4</sub> shows the absorption edge at ~ 520 nm, in agreement with a gap of 2.4 eV and shows a shoulder at 450 nm. Upon deposition of polystyrene photonic crystals from 282 nm sphere size (PC<sub>282</sub>) on Mo:BiVO<sub>4</sub> layer, the stop band peak was at 653 nm as shown in Figure 20 B (b). After the infiltration, it shifted toward blue region to a defined peak at 573 nm for 282-i-TiO<sub>2</sub>-o/Mo:BiVO<sub>4</sub> (thickness = 2.11 ± 0.407 μm) as shown in Figure 20 B (a). Figure 20 C and 20 D shows the UV-Vis absorption spectra of 282-i-TiO<sub>2</sub>-o/40 μl Mo:BiVO<sub>4</sub> and 282-i-TiO<sub>2</sub>-o/20 μl cast Mo:BiVO<sub>4</sub> respectively. Both Figures 20 C and

20 D have similar positions of peaks as in Figure 20 B except for the PC<sub>282</sub>/20  $\mu$ l cast Mo:BiVO<sub>4</sub> which is shifted towards 620 nm. However, the peaks seem to get broader as the thickness of Mo:BiVO<sub>4</sub> increases. In this chapter, closed packed face centered cubic (FCC) structures having 26% air voids and 74% polystyrene spheres are formed from the assembled photonic crystals from polystyrene spheres with refractive index (n = 1.59).<sup>38</sup> On the other hand, voids were infiltrated with high refractive index material followed by calcination of TiO<sub>2</sub> (n = 2.2) and the polystyrene spheres to achieve a high refractive index. This will result in 74 % air voids and 26 % TiO<sub>2</sub> which is called inverse opals.<sup>38</sup> According to Bragg's equation, the wavelength of center or maximum of the stop band is calculated:<sup>61</sup>

$$\lambda = 2D\sqrt{(0.74 \times n_s^2) + (0.26 \times n_v^2)}$$

D is equal to 0.87 times the diameter of the PS sphere, n<sub>s</sub> and n<sub>v</sub> are the refractive indices of polystyrene and void respectively.<sup>61</sup>

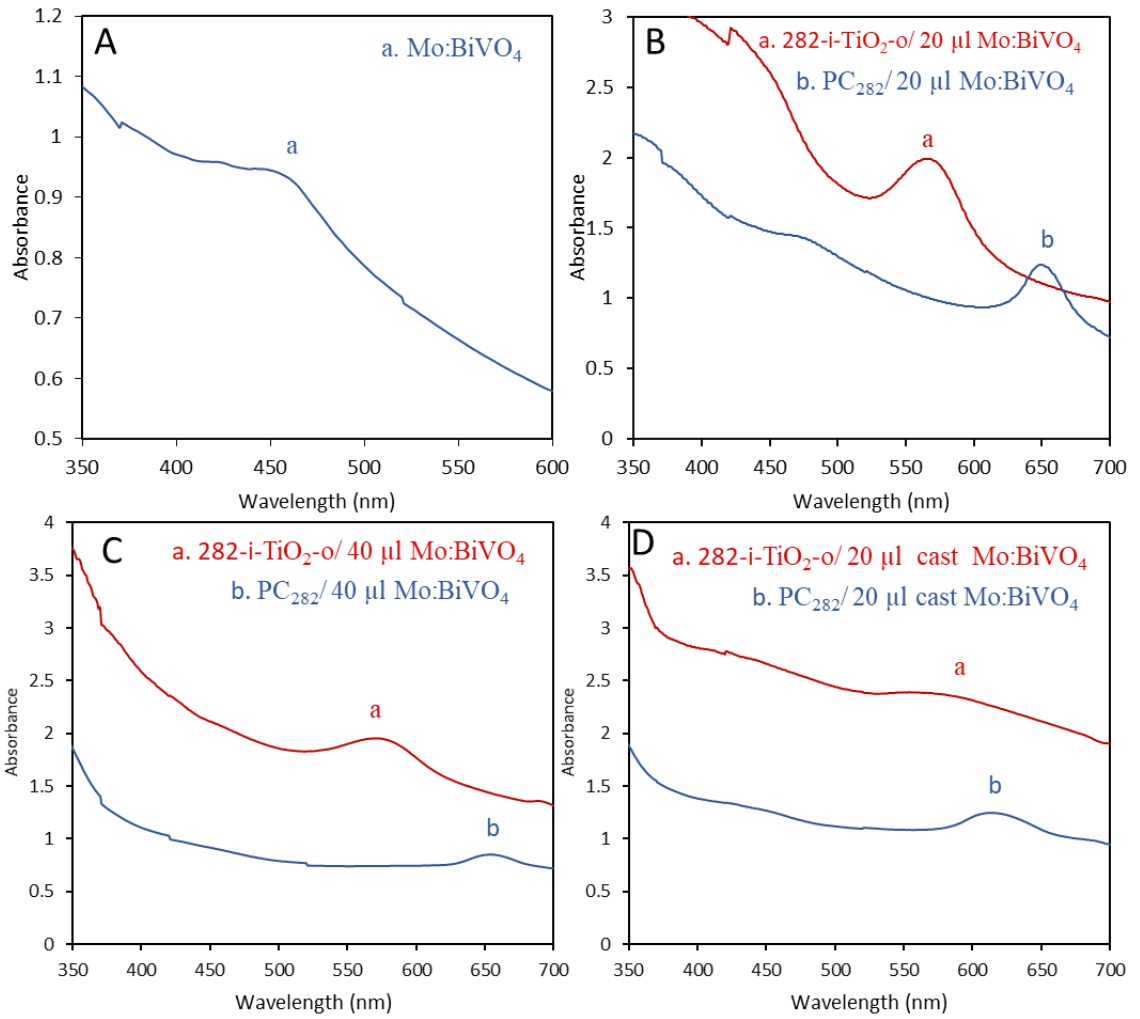


**Figure 20.** UV-Vis absorption spectra of (A) Mo:BiVO<sub>4</sub>, (B) bilayer 282-i-TiO<sub>2</sub>-o/20 μl Mo:BiVO<sub>4</sub>, (C) 282-i-TiO<sub>2</sub>-o/40 μl Mo:BiVO<sub>4</sub> and (D) 282-i-TiO<sub>2</sub>-o/20 μl cast Mo:BiVO<sub>4</sub>.

## 2. SEM Characterization of Bilayer 282-i-TiO<sub>2</sub>-o/Mo:BiVO<sub>4</sub> of Different Thicknesses

SEM images were taken to study the morphology of Mo:BiVO<sub>4</sub> photoanodes coupled to TiO<sub>2</sub> photonic crystals of different thickness. Figure 21 shows a bilayer of ordered TiO<sub>2</sub> inverse opals 282 nm size with Mo:BiVO<sub>4</sub> located at left and combination in the middle. The air-hole size measurements from the SEM image in Figure 21 B shows an average diameter of  $0.217 \pm 0.012$  μm. The % shrinkage is 23.05%.

According to Bragg's equation, the size of the TiO<sub>2</sub> voids corresponding to UV-Vis peak equals 0.205 μm (  $n_v = 2.2$ ) which also indicates shrinkage of the air-hole size.

Figure 22 A and B have similar bilayer structure of ordered inverse opals. The Mo:BiVO<sub>4</sub> nanostructures observed in Figure 22 A ( 40 μl consecutive spread deposition ) look bigger and connected while in Figure 22 B the Mo:BiVO<sub>4</sub> (20 μl cast) looks more condensed. The difference observed is related to the different method of deposition of the 20 μl of Mo:BiVO<sub>4</sub> used. The precursor solution was spread for the film in Figure 21 A, the quantity was doubled for the film in Figure 22A and the 20 μl Mo:BiVO<sub>4</sub> was cast without spreading in the film shown in Figure 22 B. All the EDXs of Figure 21 C and 22 (C and D) indicate the presence of Ti and O corresponding to TiO<sub>2</sub>. And they also indicate the presence of Bi ,V , O corresponding to BiVO<sub>4</sub>. Only in Figure 21 C, the EDX indicates the presence of Mo but, not in Figure 22 C and D. It seems that at higher thickness of Mo:BiVO<sub>4</sub>, the small quantity of Mo is not detected since in some measurements the peak of Mo coincides with Bi.

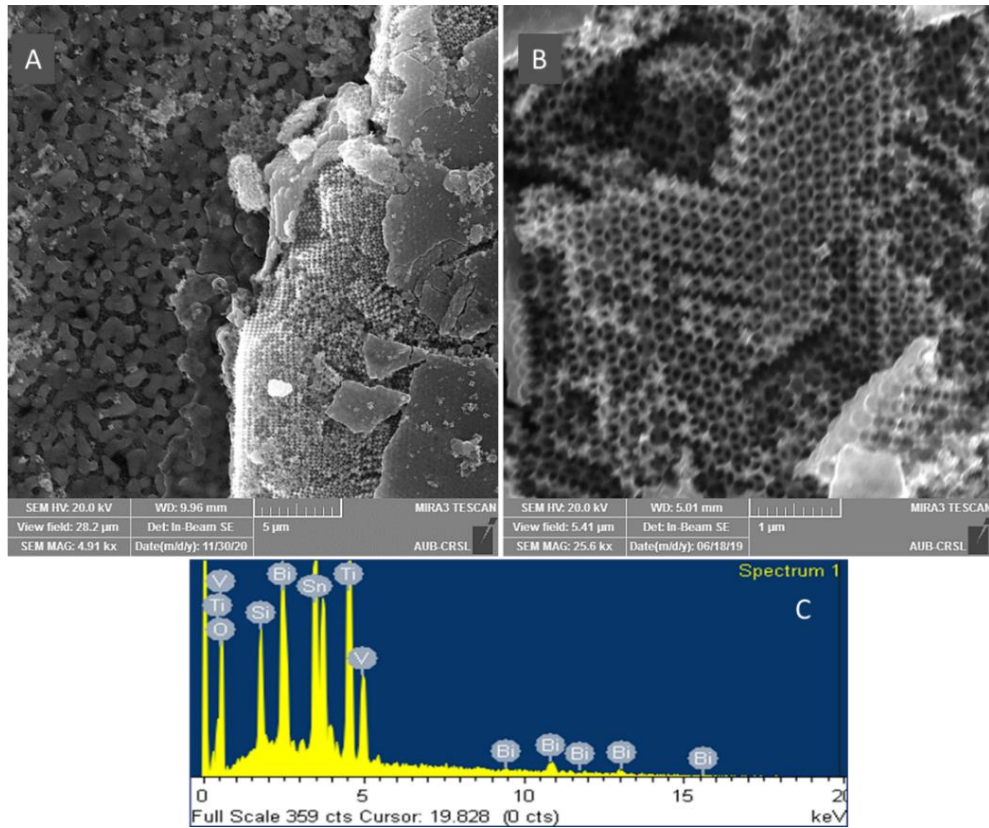


**Figure 21.** SEM images of (A) bilayer 282-i-TiO<sub>2</sub>-o/Mo:BiVO<sub>4</sub> of thickness ( $2.11 \pm 0.407 \mu\text{m}$ ), (B) inverse opal structures of 282 sphere size with average air-hole diameter  $0.21 \pm 0.12 \mu\text{m}$  respectively and with (C) its EDX.

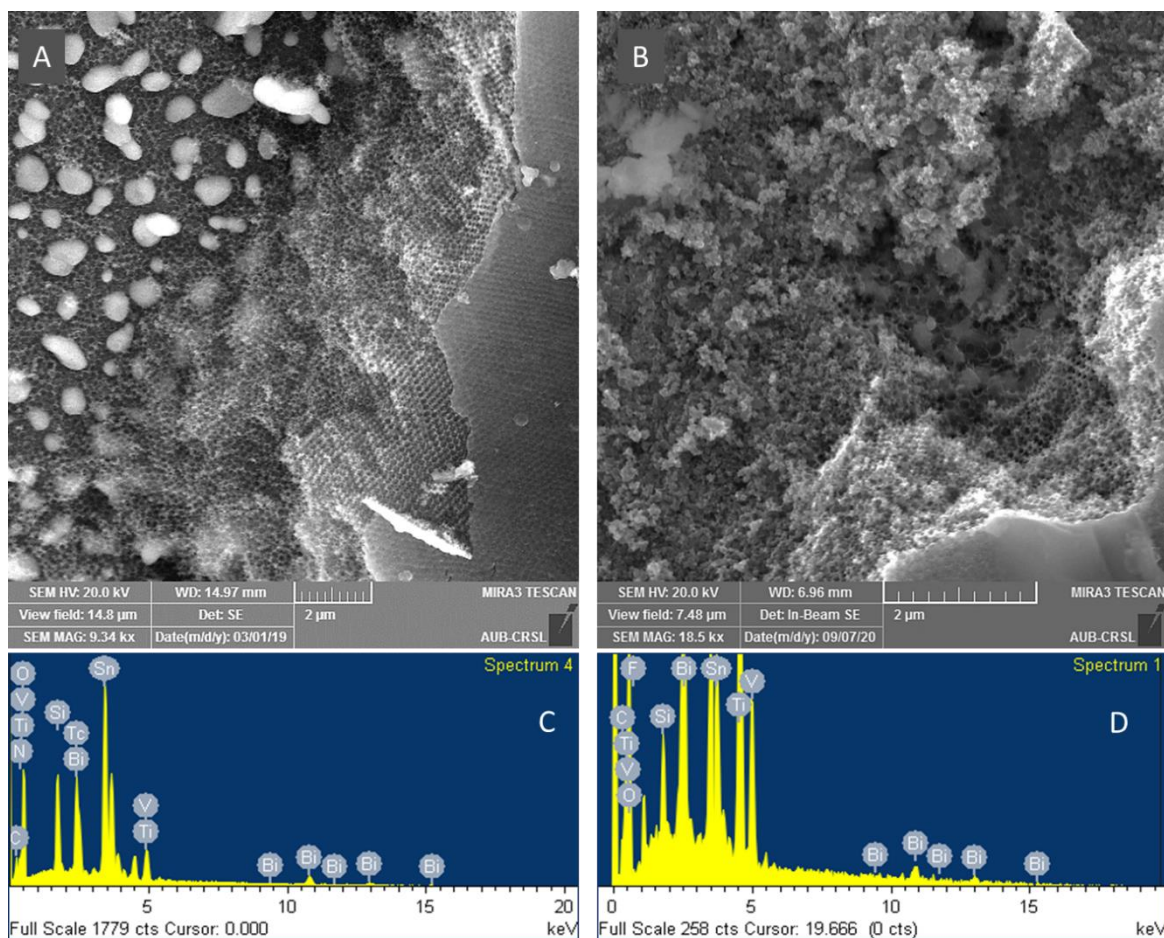


**Figure 22.** SEM images of bilayer 282-i-TiO<sub>2</sub>-o/Mo:BiVO<sub>4</sub> of different thickness ( A: 2.63 ± 0.77 μm, B: 3.99 ± 1.07 μm ) and with their EDX spectra (C and D) respectively.

### ***3. Investigation of Photoelectrochemical Behavior of 282-i-TiO<sub>2</sub>-o of different thickness Coupled to different thickness of Mo:BiVO<sub>4</sub> Electrodes***

To understand the photoelectrochemical behavior of 282-i-TiO<sub>2</sub>-o coupled to different thickness of Mo:BiVO<sub>4</sub> electrodes, incident-photon-to-current conversion efficiency (%IPCE) and cyclic voltammograms measurements were performed in 0.5 M Na<sub>2</sub>SO<sub>4</sub> in 0.1 M Na<sub>2</sub>SO<sub>3</sub> (pH~ 9.63) as a fast hole scavenger at 0.6 V vs Ag/AgCl. Figure 23 A shows the average and best film of highest % IPCE of 282-i-TiO<sub>2</sub>-o/ 20 μl Mo:BiVO<sub>4</sub> at 0.6 V vs Ag/AgCl in back-wall light illumination. The onset photocurrent occurs at 500 - 520 nm which is consistent with Mo:BiVO<sub>4</sub> band gap (E<sub>g</sub>= 2.4 eV) and

its absorption onset and generally a plateau with max %IPCE is observed between 360 - 450 nm. The %IPCE of the best Mo:BiVO<sub>4</sub> film equaled 31.14 % at 400nm, and after 282-i-TiO<sub>2</sub>-o addition, it increased to 74.40 % at 400 nm. Moreover, the average %IPCE of Mo:BiVO<sub>4</sub> films equaled  $26.96 \pm 10.50$  % (N = 4) at 400 nm, and it increased with the addition of 282-i-TiO<sub>2</sub>-o to  $64.68 \pm 10.56$  % (N = 4) at 400 nm.

The photocurrent was enhanced by a factor of  $2.21 \pm 0.53$  after 282-i-TiO<sub>2</sub>-o addition on Mo:BiVO<sub>4</sub> electrode at total average % IPCE between 300-500nm. A factor of 2.15 enhancement is measured for best film % IPCE between 300-500 nm. This indicates that the enhancement was caused by ordered TiO<sub>2</sub> inverse opals and can be attribute to internal light trapping and backscattering in the 282-i-TiO<sub>2</sub>-o/Mo:BiVO<sub>4</sub>.

Figure 23 B represents I -V curves of the best film in %IPCE of 282-i-TiO<sub>2</sub>-o/ Mo:BiVO<sub>4</sub> in the dark and with back-wall light illumination at 100 mW/cm<sup>2</sup> intensity in sulfate sulfite solution. The onset potential cathodically shifts from -0.47 V vs Ag/AgCl to -0.56 V vs Ag/AgCl after the addition of the ordered TiO<sub>2</sub> inverse opals on the Mo:BiVO<sub>4</sub> as shown in Figure 23 B. The current density of Mo:BiVO<sub>4</sub> at 0.6 V vs Ag/AgCl is 2.02 mA/cm<sup>2</sup> and after 282-i-TiO<sub>2</sub>-o addition, it increases to 3.75 mA/cm<sup>2</sup> as shown in Figure 23 B. The photocurrent was enhanced by a factor of 1.85 after 282-i-TiO<sub>2</sub>-o addition on Mo:BiVO<sub>4</sub> electrode. The current densities in this I-V curve resulted in an enhancement in photocurrent as observed in % IPCE but the overall gain in %IPCE is greater than the overall gain of I-V curves. Under white light illumination from 300 W Xenon lamp of 100 mA/cm<sup>2</sup> intensity, absorption of light by inverse opal TiO<sub>2</sub> in the bilayer can lead to photocurrent generation and affect both the photocurrent onset and the photocurrent.

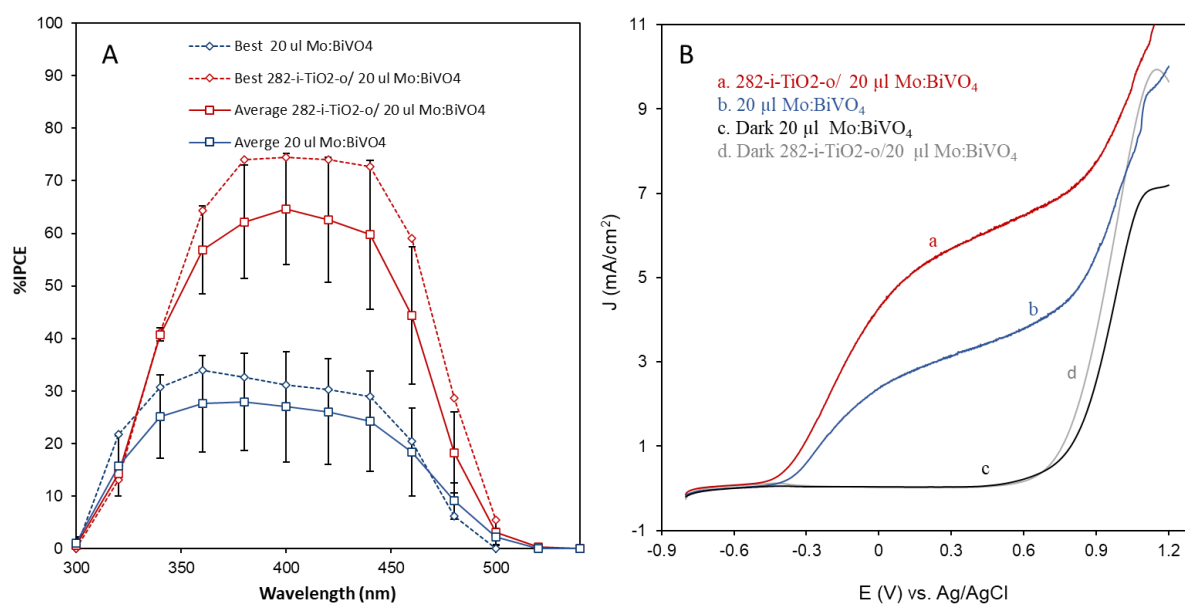


**Figure 23.** %IPCE at 0.6 V vs Ag/AgCl of (A) average and best film (highest %IPCE) bilayer 282-i-TiO<sub>2</sub>-o/ 20 μl Mo:BiVO<sub>4</sub> with the best film (B) I-V curves in the dark and back light illumination at 100 mW/cm<sup>2</sup> intensity of a scan rate 10 mV/s. Electrolyte solution is 0.5 M Na<sub>2</sub>SO<sub>4</sub> in 0.1 M Na<sub>2</sub>SO<sub>3</sub> solution (pH ~ 9.63).

Figure 24 A shows the average and best film of highest % IPCE of 282-i-TiO<sub>2</sub>-o/ 40 μl Mo:BiVO<sub>4</sub> at 0.6 V vs Ag/AgCl in back-wall light illumination. The onset photocurrent occurs at 500 nm and a plateau with max %IPCE is observed between 360 - 420 nm. The %IPCE of the best Mo:BiVO<sub>4</sub> film equals 20.73 % at 380 nm, and after 282-i-TiO<sub>2</sub>-o addition, it increased to 64.51 % at 380 nm. Moreover, the average %IPCE of Mo:BiVO<sub>4</sub> films equaled  $22.36 \pm 2.3$  % (N = 2) at 380 nm, and it increases with the addition of 282-i-TiO<sub>2</sub>-o to  $46.59 \pm 25.34$  % (N = 2) at 380 nm. The photocurrent was enhanced by a factor of  $1.71 \pm 1.13$  after 282-i-TiO<sub>2</sub>-o addition on Mo:BiVO<sub>4</sub> electrode measured from a total average % IPCE between 300-500nm. An improvement in photocurrent is observed for 282-i-TiO<sub>2</sub>-o/ 40 μl Mo:BiVO<sub>4</sub> by a factor of 2.52 enhancement for best film from % IPCE between 300-500 nm. But the average gain in %IPCE of the 282-i-TiO<sub>2</sub>-o/ 20 μl Mo:BiVO<sub>4</sub> which equaled  $2.21 \pm 0.53$  was

higher than the average gain in %IPCE of the 282-i-TiO<sub>2</sub>-o/ 40  $\mu$ l Mo:BiVO<sub>4</sub> which equaled  $1.71 \pm 1.13$  at total average % IPCE between 300-500nm. The reason is due to higher thickness of the 282-i-TiO<sub>2</sub>-o / 40  $\mu$ l Mo:BiVO<sub>4</sub> film and the structure of 40  $\mu$ l Mo:BiVO<sub>4</sub> where the nanostructured Mo:BiVO<sub>4</sub> are more connected that affected the photocurrent enhancement.

Figure 24 C represents I -V curves of the best film in %IPCE of 282-i-TiO<sub>2</sub>-o/ 40  $\mu$ l Mo:BiVO<sub>4</sub> in the dark and with back-wall light illumination at 100 mW/cm<sup>2</sup> intensity in sulfate sulfite solution. The onset potential cathodically shifts from -0.53 V vs Ag/AgCl to -0.62 V vs Ag/AgCl after the addition of the ordered TiO<sub>2</sub> inverse opals on the Mo:BiVO<sub>4</sub> as shown in Figure 24 C. The current density of 40  $\mu$ l Mo:BiVO<sub>4</sub> at 0.6 V vs Ag/AgCl is 1.81 mA/cm<sup>2</sup> and after 282-i-TiO<sub>2</sub>-o addition, it increases to 1.67 mA/cm<sup>2</sup> as shown in Figure 24 C. The photocurrent increased by a factor of 1.07 after 282-i-TiO<sub>2</sub>-o addition on 40  $\mu$ l Mo:BiVO<sub>4</sub> electrode. The current densities in this I-V curve also resulted in an enhancement as observed in the best % IPCE. So, the I-V curve photocurrent gain is 1.07 was lower than the photocurrent gain of %IPCE of a factor 1.71 for the same film. The gain in photocurrent in the best film I-V curves of the 282-i-TiO<sub>2</sub>-o/ 20  $\mu$ l Mo:BiVO<sub>4</sub> equaled 1.85 higher than the photocurrent gain in best film I-V curves of the 282-i-TiO<sub>2</sub>-o/ 40  $\mu$ l Mo:BiVO<sub>4</sub> which equaled 1.07 at 0.6 V vs Ag/AgCl in back-wall light illumination.

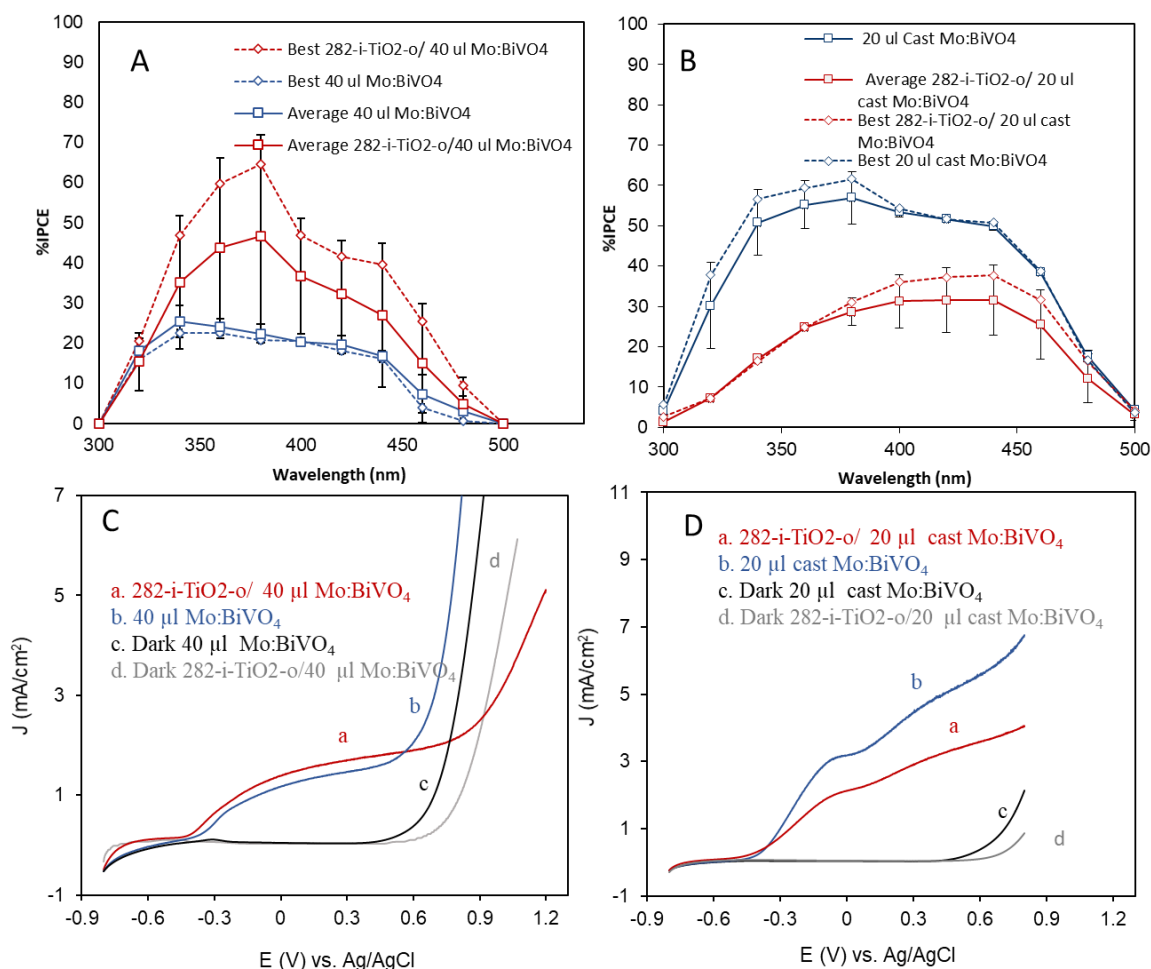


**Figure 24.** %IPCE at 0.6 V vs Ag/AgCl of (A) average and best film (highest %IPCE) bilayer 282-i-TiO<sub>2</sub>-o/ 40 μl Mo:BiVO<sub>4</sub>, (B) average and best film (highest %IPCE) bilayer 282-i-TiO<sub>2</sub>-o/ 20 μl cast Mo:BiVO<sub>4</sub> with their best film I-V curves (C and D) respectively in the dark and back light illumination at 100 mW/cm<sup>2</sup> intensity of a scan rate 10 mV/s. Electrolyte solution is 0.5 M Na<sub>2</sub>SO<sub>4</sub> in 0.1 M Na<sub>2</sub>SO<sub>3</sub> solution (pH ~ 9.63).

Figure 24 B shows the average and best film of highest % IPCE of 282-i-TiO<sub>2</sub>-o/ 20 μl cast Mo:BiVO<sub>4</sub> at 0.6 V vs Ag/AgCl in back-wall light illumination. The onset photocurrent occurs at 500 nm and generally plateau with max %IPCE between 360 - 450 nm. Figure 24 B shows the best film among the averaged films that reached the highest %IPCE for 282-i-TiO<sub>2</sub>-o / 20 μl cast Mo:BiVO<sub>4</sub>. The %IPCE of the best Mo:BiVO<sub>4</sub> film equaled 61.54 % at 380 nm, and after 282-i-TiO<sub>2</sub>-o addition, it

decreased to 37.64 % at 440 nm. Moreover, the average %IPCE of Mo:BiVO<sub>4</sub> films equaled  $56.92 \pm 6.52$  % (N = 2) at 380 nm, and it decreases with the addition of 282-i-TiO<sub>2</sub>-o to  $31.52 \pm 8.0$  % (N = 2) at 420 nm. The photocurrent declined to a factor of  $0.51 \pm 0.064$  after 282-i-TiO<sub>2</sub>-o addition on Mo:BiVO<sub>4</sub> electrode at total average % IPCE between 300-500nm. A decline in photocurrent is observed for 282-i-TiO<sub>2</sub>-o/ 20  $\mu$ l cast Mo:BiVO<sub>4</sub> to a factor of 0.56 in best film % IPCE between 300-500 nm. The absence of an enhancement for Mo:BiVO<sub>4</sub> prepared using the second deposition method (cast) which resulted in a more packed structure can possibly be attributed to this morphology not allowing as much infiltration of TiO<sub>2</sub> in Mo:BiVO<sub>4</sub>.

Figure 24 D represents I -V curves of the best film in %IPCE of 282-i-TiO<sub>2</sub>-o/ 20  $\mu$ l cast Mo:BiVO<sub>4</sub> in the dark and with back-wall light illumination at 100 mW/cm<sup>2</sup> intensity in sulfate sulfite solution. The onset potential cathodically shifts from -0.481 V vs Ag/AgCl to -0.529 V vs Ag/AgCl after the addition of the ordered TiO<sub>2</sub> inverse opals on the Mo:BiVO<sub>4</sub> as shown in Figure 24 D. The current density of 20  $\mu$ l cast Mo:BiVO<sub>4</sub> at 0.6 V vs Ag/AgCl is 5.21 mA/cm<sup>2</sup> and after 282-i-TiO<sub>2</sub>-o addition, it decreases to 3.47 mA/cm<sup>2</sup> as shown in Figure 24 D. The photocurrent declined to a factor of 0.67 after 282-i-TiO<sub>2</sub>-o addition on 20  $\mu$ l cast Mo:BiVO<sub>4</sub> electrode. The current densities in this I-V curve also resulted in a decline in photocurrent as observed in the best % IPCE. To be noted that as the thickness of Mo:BiVO<sub>4</sub> increased (initial %IPCE higher), as the film structure was more packed, the enhancement factor caused by coupling to i-TiO<sub>2</sub>-o.

#### 4. The Effect of 282-i-TiO<sub>2</sub>-o on the Photoelectrochemical Behavior

To better understand the reason behind the enhancement that occurs after coupling 20  $\mu\text{l}$  Mo:BiVO<sub>4</sub> with 282-i-TiO<sub>2</sub>-o, cyclic voltammograms and %IPCE measurements of the background 282-i-TiO<sub>2</sub>-o were performed in sulfate sulfite electrolyte. Figure 25 A shows the I -V curves of the 282-i-TiO<sub>2</sub>-o alone in the dark with both front and back light illumination at 100 mW/cm<sup>2</sup> intensity in sulfate sulfite solution. The onset potential was at -0.62 V vs Ag/AgCl in back illumination and at -0.728 V vs Ag/AgCl in front illumination. This indicates that the onset potential shift that was reported for 282-i-TiO<sub>2</sub>-o/Mo:BiVO<sub>4</sub> is due to the absorption of TiO<sub>2</sub> of a bandgap ( $E_g = 3.2$  eV). The current density of 282-i-TiO<sub>2</sub>-o at 0.6V vs Ag/AgCl equals 1.18 mA/cm<sup>2</sup> upon back light illumination, it equals 3.18 mA/cm<sup>2</sup> upon front light illumination as shown in Figure 25 A.

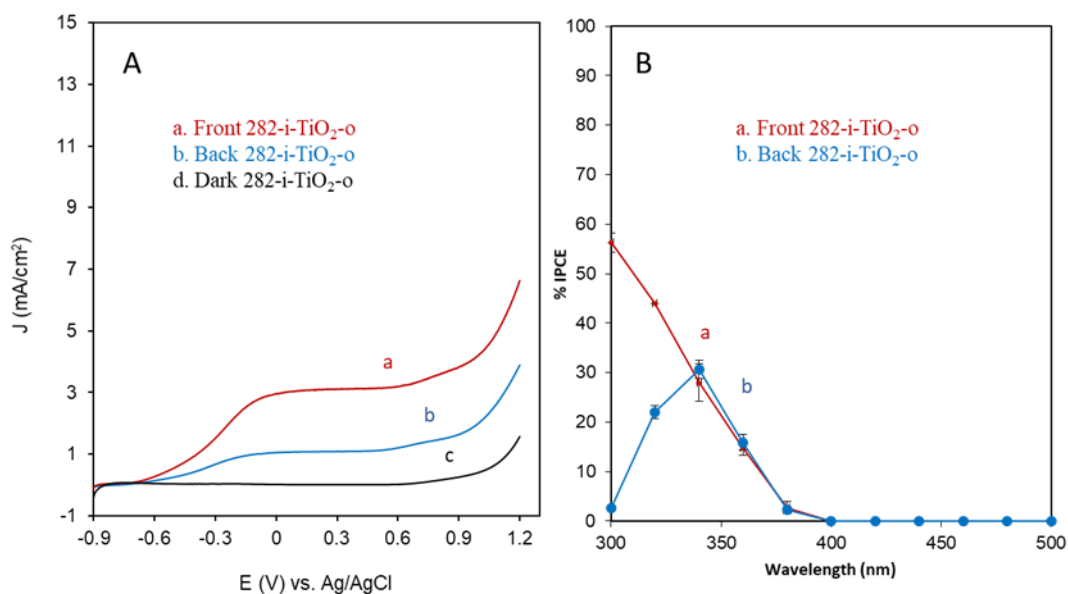


**Figure 25.** I-V curves of (A) 282-i-TiO<sub>2</sub>-o in dark and upon light under front and back illumination of 10mV/s scan rate with their (B) %IPCE vs wavelength (nm) at 0.6 V vs Ag/AgCl in 0.5 M Na<sub>2</sub>SO<sub>4</sub> in 0.1 M Na<sub>2</sub>SO<sub>3</sub> solution (pH ~ 9.63).

Figure 25 B shows the average % IPCE of 282-i-TiO<sub>2</sub>-o at 0.6 V vs Ag/AgCl in back and front light illumination. The photocurrent onset is at 380 - 400 nm and it maximizes at 340 nm then decreases to reach almost zero at 300 nm when the electrode is illuminated from the back as shown in Figure 25 B. However, when the electrode is illuminated from the front, the %IPCE continues to increase up to 300 nm as shown in Figure 25 B. The average %IPCE in front-wall illumination increased to  $56.25 \pm 1.8$  % (N=2) at 300 nm as shown in Figure 26 B. The average % IPCE in back-wall illumination increased to  $30.63 \pm 1.8$  % (N=2) at 340 m. The % IPCE of the background 282-i-TiO<sub>2</sub>-o at 400 nm is zero whether the electrode is illuminated from the back or from the front.

To be noted that the onset at 380 nm is consistent with TiO<sub>2</sub> absorbance ( $E_g = 3.2$  eV) and the values of %IPCE of the background under back wall light illumination are lower than the values obtained with the presence of Mo:BiVO<sub>4</sub>. The gain at 400 nm and the longer wavelength measured in % IPCE is all due to the coupling effect of the 282-i-TiO<sub>2</sub>-o with Mo:BiVO<sub>4</sub> electrodes. On the other hand, under back-wall illumination, a certain amount of photocurrent at shorter wavelength can be due to TiO<sub>2</sub>. The heterojunction system could have enhanced the electron and charge separation because from the conduction band of BiVO<sub>4</sub> the electron would flow to conduction band of TiO<sub>2</sub> leading to current enhancement.<sup>45</sup> To better understand the effect of coupling TiO<sub>2</sub> to Mo:BiVO<sub>4</sub>, further investigation was conducted by coupling 282-i-TiO<sub>2</sub> -g to Mo:BiVO<sub>4</sub> and nc-TiO<sub>2</sub> to Mo:BiVO<sub>4</sub> electrodes.

## **C. Disordered TiO<sub>2</sub> Inverse Glass as Photonic Crystals Coupled to Mo:BiVO<sub>4</sub> Photoanode Using the Same Air Hole Size (282 nm)**

### ***1. UV-Vis Absorption Spectra of Bilayer 282-i-TiO<sub>2</sub>-g/Mo:BiVO<sub>4</sub>***

To investigate the effect of order inverse opals versus disordered inverse glass on the photocurrent enhancement, disordered and ordered TiO<sub>2</sub> using the same air-hole size was coupled to Mo:BiVO<sub>4</sub>. Polystyrene 282 nm sphere size was assembled with similar preparation to that of 282-i-TiO<sub>2</sub>-o/Mo:BiVO<sub>4</sub>, however with the presence of NaCl during assembly process leading to disordered polystyrene photonic glass (PG<sub>282</sub>).<sup>33</sup> It is indicated that increasing ionic strength to causes a disorder in the assembly.<sup>33</sup> . Repulsion between interparticle is screened by the salt lead to disordered packing by reducing the barrier preventing the particle from flocculating.<sup>62</sup> This led to disordered TiO<sub>2</sub> inverse glass 282 nm sphere size on top of Mo:BiVO<sub>4</sub> (282-i-TiO<sub>2</sub>-g/Mo:BiVO<sub>4</sub>). The bilayer thickness equals  $3.99 \pm 2.65$   $\mu\text{m}$ . The UV-vis absorption spectra for PG<sub>282</sub>/ Mo:BiVO<sub>4</sub> and bilayer 282-i-TiO<sub>2</sub>-g/Mo:BiVO<sub>4</sub> shows no peak neither in the photonic glass (b) nor for the inverse glass (a) in Figure 26. A broad shoulder centered at the position of the PG<sub>282</sub> stop band peak at 650 nm was observed in Figure 26. A broad shoulder and absence of a peak confirms the significant disorder in this template.

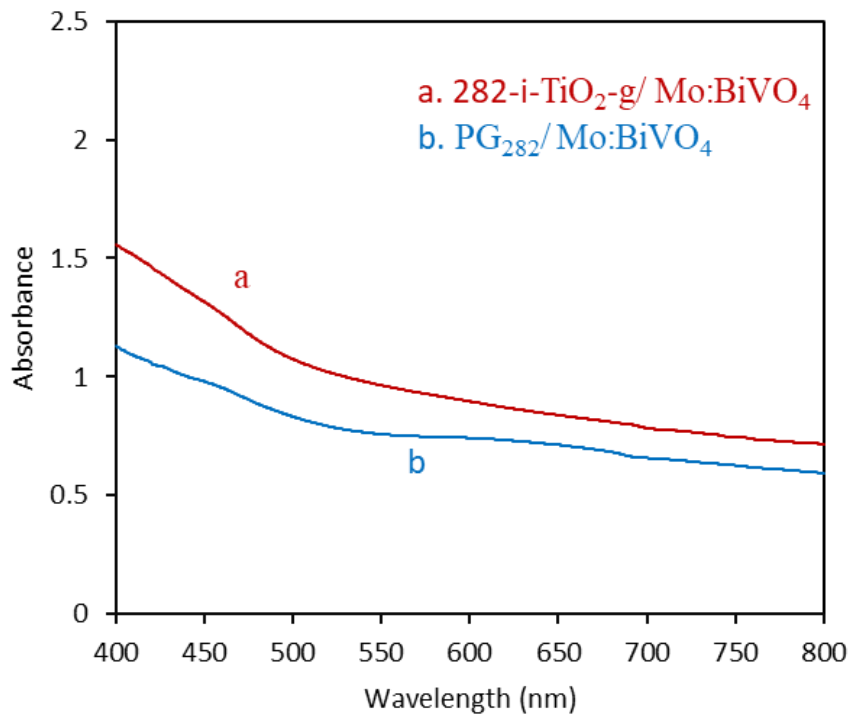


**Figure 26.** UV-vis absorption spectra of (a) PG<sub>282</sub>/ Mo:BiVO<sub>4</sub>, and (b) bilayer 282-i-TiO<sub>2</sub>-g/Mo:BiVO<sub>4</sub>

## 2. Characterization of PG<sub>282</sub>/Mo:BiVO<sub>4</sub> and Bilayer 282-i-TiO<sub>2</sub>-g/Mo:BiVO<sub>4</sub>

To better understand and compare the morphology of ordered and disordered TiO<sub>2</sub> coupled to Mo:BiVO<sub>4</sub>, SEM images were acquired. Figure 27 A shows SEM image of photonic glass (PG) formation assembled in the presence of salt on top of Mo:BiVO<sub>4</sub>. The PG spheres are disordered with an average diameter of (0.26 ± 0.01 μm) and PG<sub>282</sub>/Mo:BiVO<sub>4</sub> film thickness equals 4.72 ± 2.87 μm. The % shrinkage is 7.8 %. Figure 27 B shows SEM image of disordered inverse glass (282-i-TiO<sub>2</sub>-g) on top of Mo:BiVO<sub>4</sub>. The 282-i-TiO<sub>2</sub>-g/Mo:BiVO<sub>4</sub> film thickness is 3.99 ± 2.65 μm. The thickness of the PG<sub>282</sub>/Mo:BiVO<sub>4</sub> film is larger than 282-i-TiO<sub>2</sub>-g/Mo:BiVO<sub>4</sub> maybe due to some loss of spheres during infiltration with TiO<sub>2</sub>. Figures 27 C and D show the EDX spectra of PG<sub>282</sub>/Mo:BiVO<sub>4</sub> and 282-i-TiO<sub>2</sub>-g/Mo:BiVO<sub>4</sub>. Both spectra identify

the presence of Na and Cl remaining in the films. In addition, Figure 27 D corresponding to the EDX of bilayer 282- i-TiO<sub>2</sub>-g/Mo:BiVO<sub>4</sub> identifies the presence of Ti and O corresponding to TiO<sub>2</sub>. In addition, all EDX spectra of 282 sphere size indicate the presence of Bi, V, O elements and Mo only observed in Figure 27 B corresponding to Mo:BiVO<sub>4</sub>. The presence of Au in the EDX in Figure 27 C is because the PG<sub>282</sub>/Mo:BiVO<sub>4</sub> film was coated by 7 nm gold for SEM imaging purpose.

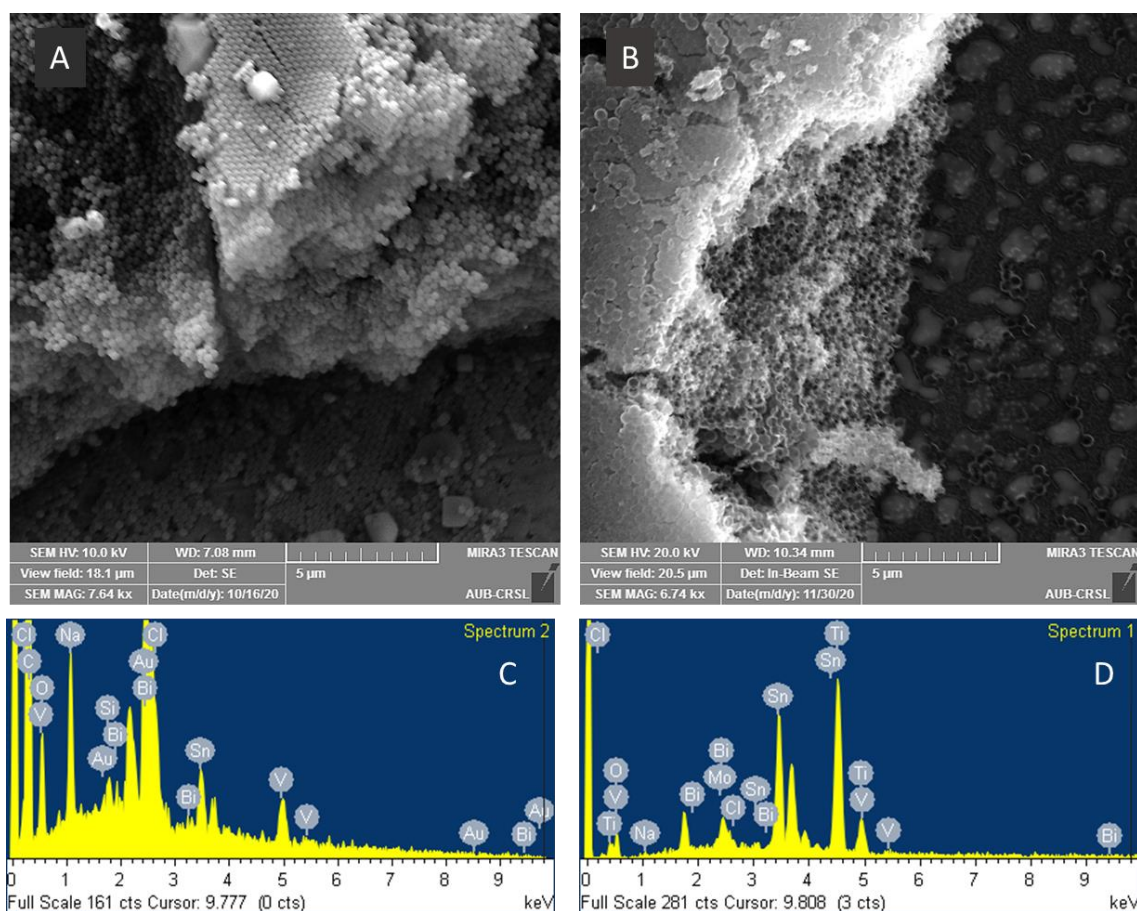


**Figure 27.** SEM images of (A) PG<sub>282</sub>/Mo:BiVO<sub>4</sub> ( $4.72 \pm 2.89 \mu\text{m}$ ) and (B) bilayer 282- i-TiO<sub>2</sub>-g/Mo:BiVO<sub>4</sub> ( $3.99 \pm 2.65 \mu\text{m}$ ), and with their EDX spectra (C and D) respectively

### 3. Investigation of Photoelectrochemical Behavior of 282nm Sphere Size Inverse

#### Glass TiO<sub>2</sub> Coupled to Mo:BiVO<sub>4</sub>

To investigate the photoelectrochemical behavior of Mo:BiVO<sub>4</sub> coupled to 282- i-TiO<sub>2</sub>-g layer, % IPCE and I-V curves measurements were performed in sulfate/sulfite

electrolyte. Figure 28 A shows the average and best film of highest % IPCE of 282-i-TiO<sub>2</sub>-g/ 20  $\mu$ l Mo:BiVO<sub>4</sub> at 0.6 V vs Ag/AgCl in back-wall light illumination. The onset photocurrent occurs at 500 - 520 nm which is consistent with Mo:BiVO<sub>4</sub> band gap ( $E_g=2.4$  eV) and its absorption onset and generally plateau occurs with max %IPCE between 360 - 450 nm. The %IPCE of the best Mo:BiVO<sub>4</sub> film equaled 37.74 % at 360nm, and after 282-i-TiO<sub>2</sub>-g addition, it increased to 53.45 % at 380 nm. Moreover, the average %IPCE of Mo:BiVO<sub>4</sub> films equaled  $37.36 \pm 12.69$  % (N = 6) at 360 nm, and it decreases with the addition of 282-i-TiO<sub>2</sub>-g to  $32.76 \pm 11.44$  % (N = 6) at 380 nm. Among the 6 films, 4 films exhibited a slight increase upon the addition of 282-i-TiO<sub>2</sub>-g and 2 films exhibited a decrease upon the addition of 282-i-TiO<sub>2</sub>-g.

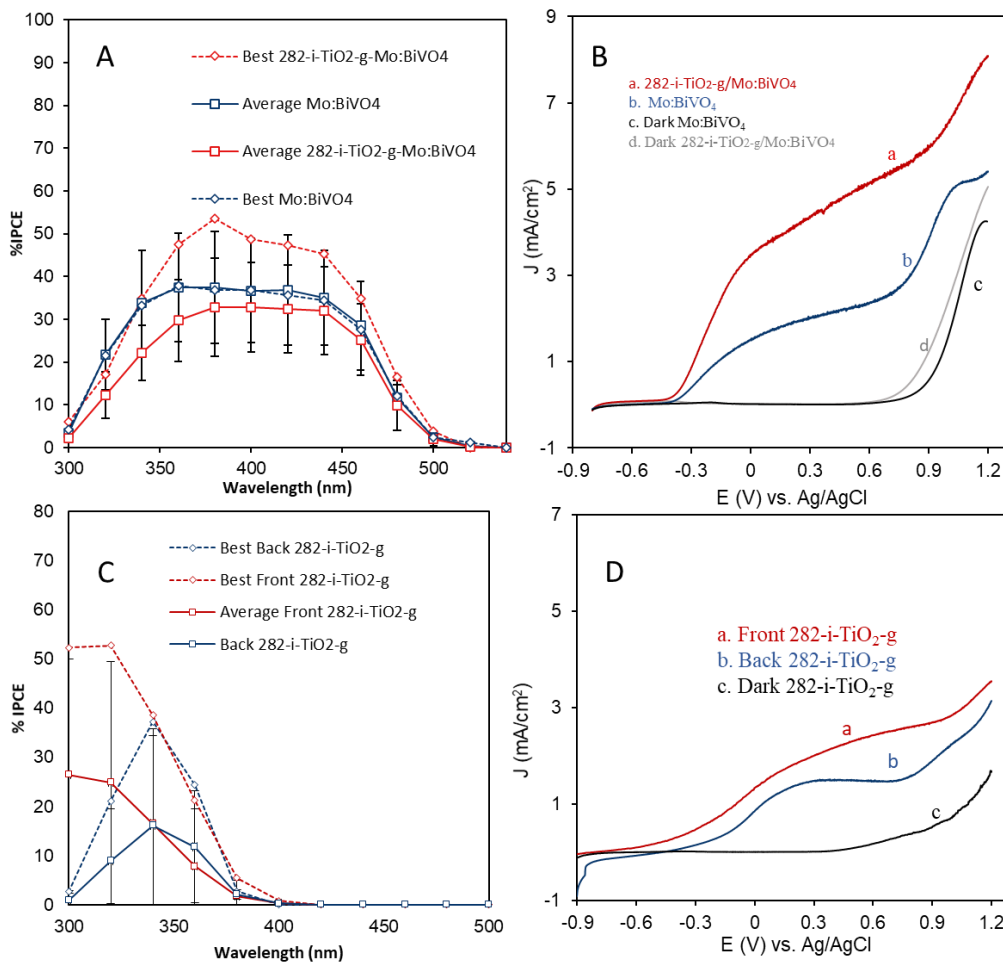


**Figure 28.** %IPCE vs wavelength (nm) at 0.6 V vs Ag/AgCl of (A) average and best film ( highest %IPCE ) bilayer 282-i-TiO<sub>2</sub>-g/ Mo:BiVO<sub>4</sub>, (C) average and best film (highest %IPCE ) 282-i-TiO<sub>2</sub>-g with their best cyclic voltammograms (B) and (D) respectively in dark and upon light under back illumination for (A,B,C and D) and front illumination (C and D) in 0.5 M Na<sub>2</sub>SO<sub>4</sub> in 0.1 M Na<sub>2</sub>SO<sub>3</sub> solution (pH ~ 9.63). The scan rate is 10 mV/s.

The photocurrent declined to a factor of  $0.89 \pm 0.34$  after 282-i-TiO<sub>2</sub>-o addition on Mo:BiVO<sub>4</sub> electrode at total average % IPCE between 300-500nm. An improvement in photocurrent is observed for 282-i-TiO<sub>2</sub>-o/Mo:BiVO<sub>4</sub> by a factor of 1.25 enhancement in best film % IPCE between 300-500 nm. This indicates that on average adding 282-i-TiO<sub>2</sub>-g does not result in similar enhancement despite the illumination being from the back compared to the integrated %IPCE total gain in 300 – 500 nm for 282-i-TiO<sub>2</sub>-o/Mo:BiVO<sub>4</sub> which equaled  $2.21 \pm 0.53$  after 282-i-TiO<sub>2</sub>-o addition on Mo:BiVO<sub>4</sub>. To be noted that the enhancement that occur in the best 282-i-TiO<sub>2</sub>-g/Mo:BiVO<sub>4</sub> film can be caused by possible back-scattering effect in the disordered 282-i-TiO<sub>2</sub>-g. The enhancement was caused by the structural ordered inverse opals rather than only scattering at disordered domains. Although scattering occurs in the disordered films but, it is maybe that there is greater backscattering in ordered inverse opals. There could be internal light trapping in the ordered 282-i-TiO<sub>2</sub>-o/Mo:BiVO<sub>4</sub> as there is indication in SEM images of intermingling. The effect cannot be caused directly by Braggs reflection since the stop band peak is located toward the red region through it extends over a broad frequency range.

Figure 28 B represents I -V curves of the best film in %IPCE of 282-i-TiO<sub>2</sub>-g/ Mo:BiVO<sub>4</sub> in the dark and with back-wall light illumination at 100 mW/cm<sup>2</sup> intensity in sulfate sulfite solution. The onset potential cathodically shifts from -0.414 V vs Ag/AgCl to -0.462 V vs Ag/AgCl after the addition of the disordered 282-i-TiO<sub>2</sub>-g on

the Mo:BiVO<sub>4</sub> as shown in Figure 28 B. The current density of Mo:BiVO<sub>4</sub> at 0.6 V vs Ag/AgCl is 2.32 mA/cm<sup>2</sup> and after 282-i-TiO<sub>2</sub>-g addition, it increases to 5.08 mA/cm<sup>2</sup> as shown in Figure 28 B. The photocurrent increased by a factor of 2.19 after 282-i-TiO<sub>2</sub>-g addition on Mo:BiVO<sub>4</sub> electrode. The current densities in this I-V curve also resulted in an enhancement as observed in best film % IPCE. However, the photocurrent gain in best I-V curve was greater than that observed in best film % IPCE.

To understand better the reason behind the increase in the best % IPCE in the disordered 282-i-TiO<sub>2</sub>-g coupled to Mo:BiVO<sub>4</sub> and in photocurrent in I-V curves, background 282-i-TiO<sub>2</sub>-g films were prepared and studied.

#### ***4. The Effect of 282-i-TiO<sub>2</sub>-g on the Photoelectrochemical Behavior***

Figure 28 C shows the average and best film % IPCE of 282-i-TiO<sub>2</sub>-g at 0.6 V vs Ag/AgCl in back and front light illumination. The photocurrent onset is at 380 - 400 nm and it maximizes at 340 nm then decreases to reach zero at 300 nm when the electrode is illuminated from the back as shown in Figure 28 C. However, when the electrode is illuminated from the front, the % IPCE continues to increase up to 300 nm as shown in Figure 28 C. The best film % IPCE in front-wall illumination increased to 52.33 at 300 nm as shown in Figure 28 C. The best film % IPCE in back-wall illumination increased to 37.28 at 340 m. The average % IPCE in front-wall illumination increased to  $26.46 \pm 23.6$  % (N=2) at 300 m as shown in Figure 28 C. The average % IPCE in back-wall illumination increased to  $16.14 \pm 18.34$  % (N=2) at 340 nm. The % IPCE of the background 282-i-TiO<sub>2</sub>-g at 400 nm is zero whether the electrode is illuminated from the back or from the front which is consistent with the absorption of

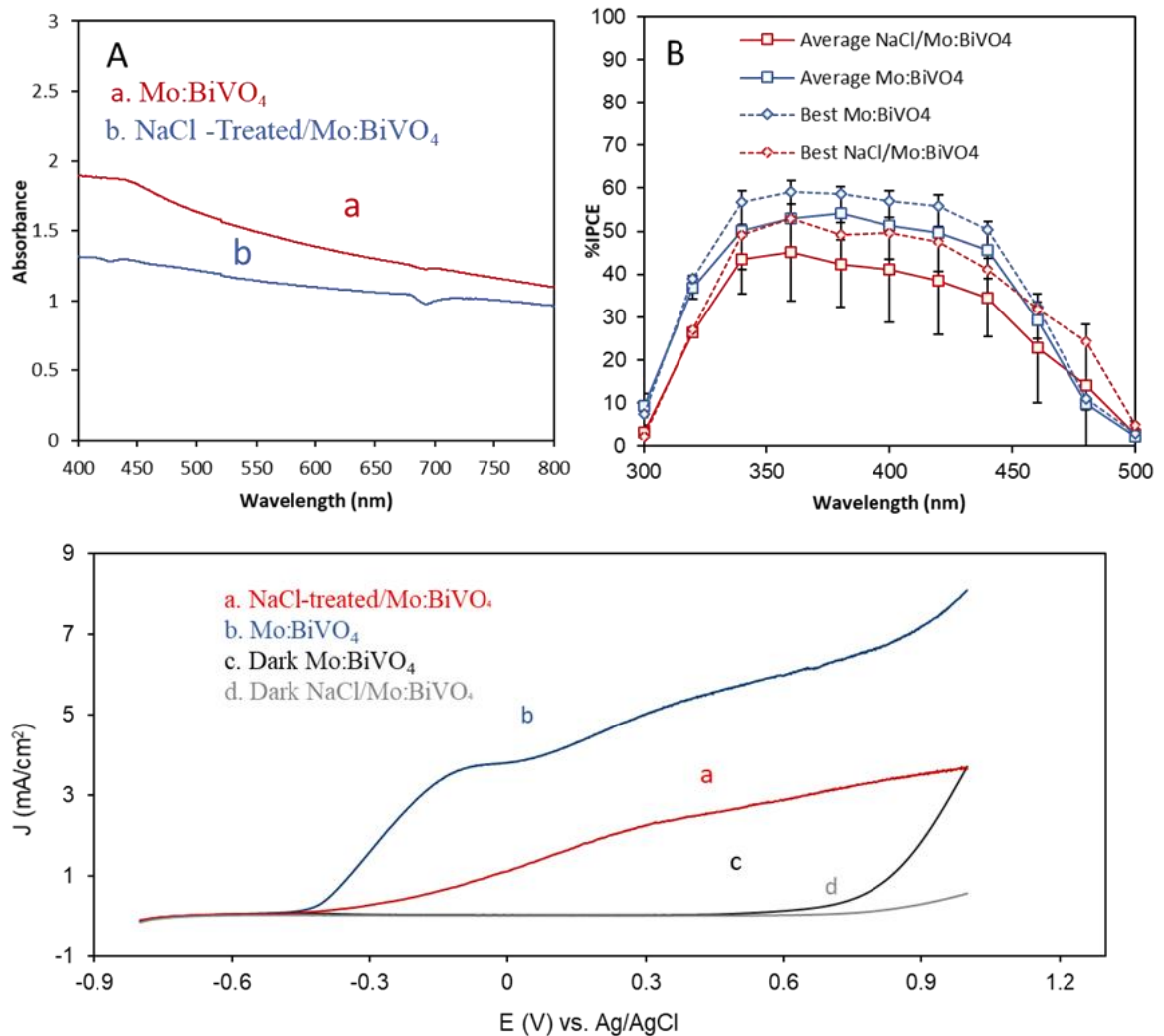
TiO<sub>2</sub> and the decrease at shorter wavelength in back-wall illumination is attributed to absorbance from FTO.

Figure 28 D shows the I -V curves of the 282-i-TiO<sub>2</sub>-g alone in the dark with both front and back light illumination at 100 mW/cm<sup>2</sup> intensity in sulfate sulfite solution. The onset potential shifts from -0.341 V vs Ag/AgCl in back illumination to -0.654 V vs Ag/AgCl in front illumination. This indicates that the onset potential shift that was reported for 282-i-TiO<sub>2</sub>-g/Mo:BiVO<sub>4</sub> is due to the absorption of TiO<sub>2</sub> of a bandgap ( $E_g = 3.2$  eV). The current density of 282-i-TiO<sub>2</sub>-g at 0.6V vs Ag/AgCl equaled 1.29 mA/cm<sup>2</sup> upon back light illumination; it equaled 2.23 mA/cm<sup>2</sup> upon front light illumination as shown in Figure 28 D. Therefore, in I-V curves of 282-i-TiO<sub>2</sub>-g/Mo:BiVO<sub>4</sub> electrodes, there can a contribution from 282-i-TiO<sub>2</sub>-g making contact with FTO or photogenerated charges from TiO<sub>2</sub> absorbance. While in % IPCE plots, photocurrents enhancement at 380 nm and longer wavelength originates from Mo:BiVO<sub>4</sub> and shorter wavelengths can have contribution from TiO<sub>2</sub>.

##### ***5. NaCl Control Test: Mo:BiVO<sub>4</sub> subjected to NaCl Treatment***

To understand better the reason behind the decrease in average %IPCE in the 282-i-TiO<sub>2</sub>-g coupled to Mo:BiVO<sub>4</sub>, a control NaCl experiment was performed while, subjecting Mo:BiVO<sub>4</sub> to similar steps of 282-i-TiO<sub>2</sub>-g/Mo:BiVO<sub>4</sub> to treat with NaCl in the absence of polystyrene in the assembly. Figure 29 A shows the UV-Vis absorption spectra of NaCl-treated/Mo:BiVO<sub>4</sub>. In Figure 29 A UV-Vis spectra of the NaCl-treated/Mo:BiVO<sub>4</sub> shows the absorption edge at ~ 520nm, in agreement with a gap of 2.4 eV and shows a shoulder at 450 nm.

Figure 29 B shows the average and best film of highest % IPCE of NaCl-treated/Mo:BiVO<sub>4</sub> at 0.6 V vs Ag/AgCl in back-wall illumination. The onset photocurrent occurs at 500nm and generally plateau with max % IPCE between 340 - 440 nm. Figure 29 B shows the best film among the averaged films that reached the highest % IPCE in NaCl-treated/Mo:BiVO<sub>4</sub>. The % IPCE of the best Mo:BiVO<sub>4</sub> film equaled 59.14% at 360nm, and after treating with NaCl, it decreased to 52.94 % at 360 nm. Moreover, the average % IPCE of Mo:BiVO<sub>4</sub> films equaled 54.22 ± 6.22% (N = 2) at 360 nm, and it decreases with the treatment of NaCl to 45.04 ± 11.18 % (N = 2) at 380 nm.



**Figure 29.** UV-Vis absorption spectra (A) of NaCl-treated/Mo:BiVO<sub>4</sub>, %IPCE at 0.6 V vs Ag/AgCl of (B) average and best film (highest %IPCE) bilayer NaCl-treated/Mo:BiVO<sub>4</sub> with its best film (B) I-V curves in the dark and back light illumination at 100 mW/cm<sup>2</sup> intensity of a scan rate 10 mV/s. Electrolyte solution is 0.5 M Na<sub>2</sub>SO<sub>4</sub> in 0.1 M Na<sub>2</sub>SO<sub>3</sub> solution (pH ~ 9.63).

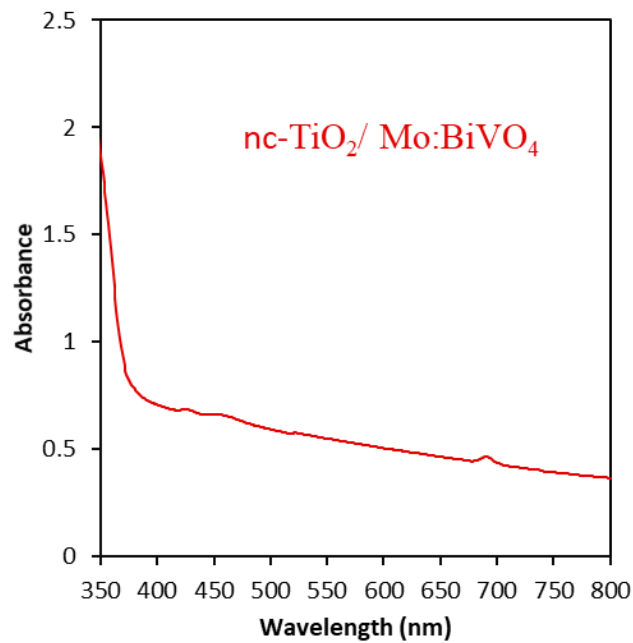
The photocurrent declined by a factor of  $0.79 \pm 0.12$  after NaCl treatment on Mo:BiVO<sub>4</sub> electrode at total average % IPCE between 300-500nm. A decline in photocurrent is observed NaCl-treated/Mo:BiVO<sub>4</sub> to a factor of 0.88 in best film % IPCE between 300-500 nm. This indicates the role of NaCl in decreasing the photocurrent by possible incorporation. There could be some possible enhancement in the photocurrent caused by disordered structure, but it may be masked by NaCl/calcination. NaCl presence could not be the full cause why the 282-i-TiO<sub>2</sub>-g/Mo:BiVO<sub>4</sub> film did not cause ca. 2.21-fold average gain as observed with 282-i-TiO<sub>2</sub>-o/Mo:BiVO<sub>4</sub>.

Figure 29 C represents I -V curves of the best film in %IPCE of NaCl-treated/Mo:BiVO<sub>4</sub> in the dark and with back-wall light illumination at 100 mW/cm<sup>2</sup> intensity in sulfate sulfite solution. The onset potential anodically shifts from -0.513 V vs Ag/AgCl to -0.427 V vs Ag/AgCl after the treating Mo:BiVO<sub>4</sub> with NaCl as shown in Figure 29 C. The current density of Mo:BiVO<sub>4</sub> at 0.6 V vs Ag/AgCl is 5.84 mA/cm<sup>2</sup> and after NaCl treatment, it decreases to 2.83 mA/cm<sup>2</sup> as shown in Figure 29 C. The photocurrent declined by a factor of 2.06 after NaCl treatment on Mo:BiVO<sub>4</sub> electrode. The current densities in this I-V curve resulted in a greater decline in photocurrent that the one observed in best film % IPCE.

## D. Mo:BiVO<sub>4</sub> Photoanodes Coupled to Nanocrystalline TiO<sub>2</sub> films

### 1. UV-Vis Absorption Spectra of Bilayer nc-TiO<sub>2</sub>/Mo:BiVO<sub>4</sub>

To investigate the effect of heterojunction with nc-TiO<sub>2</sub> on the photocurrent enhancement, nc-TiO<sub>2</sub> was coupled to Mo:BiVO<sub>4</sub>. Using squeegee method, nanocrystalline TiO<sub>2</sub> films were deposited on Mo:BiVO<sub>4</sub> films forming the bilayer nc-TiO<sub>2</sub>/Mo:BiVO<sub>4</sub>. Figure 30 represents the UV-vis absorption spectra of bilayer nc-TiO<sub>2</sub>/Mo:BiVO<sub>4</sub>. A shoulder at 450 nm was observed for nc-TiO<sub>2</sub>/Mo:BiVO<sub>4</sub> corresponding to Mo:BiVO<sub>4</sub> in Figure 30.



**Figure 30.** UV-vis absorption spectra of bilayer nc-TiO<sub>2</sub>/Mo:BiVO<sub>4</sub>

## 2. Characterization of Bilayer nc-TiO<sub>2</sub>/Mo:BiVO<sub>4</sub>

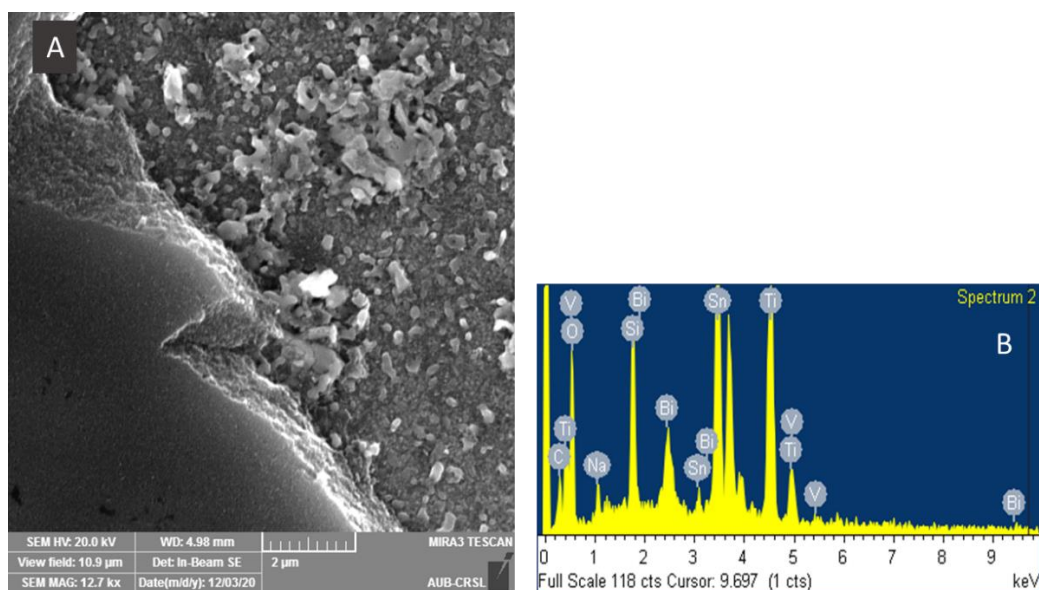


**Figure 31.** SEM images of (A) bilayer nc-TiO<sub>2</sub>/Mo:BiVO<sub>4</sub> ( $1.57 \pm 0.77 \mu\text{m}$ ) with (B) its EDX spectrum.

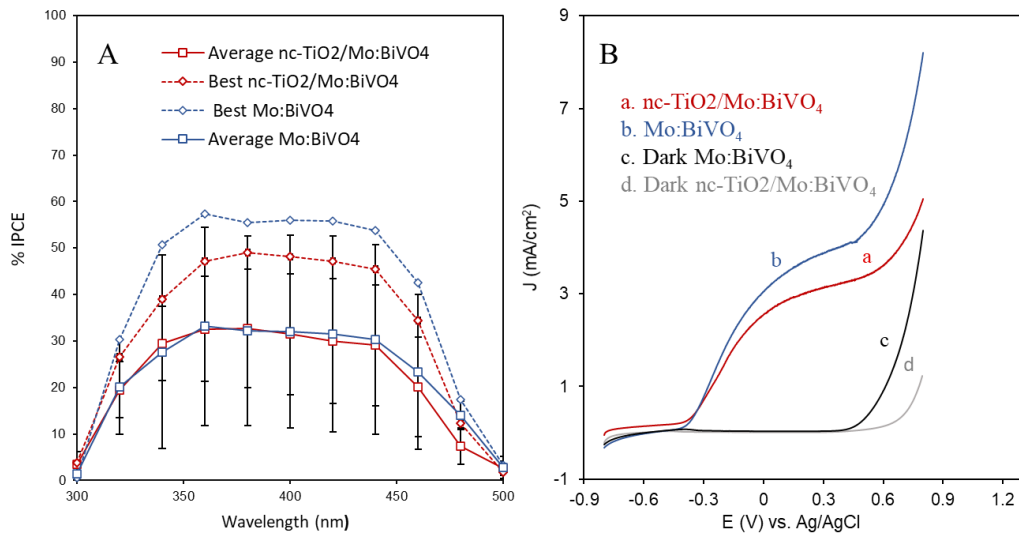
SEM images were taken to study the morphology of Mo:BiVO<sub>4</sub> photoanodes coupled to nc-TiO<sub>2</sub>. Figure 31 A shows an SEM image of nc-TiO<sub>2</sub>/Mo:BiVO<sub>4</sub> where non-scattering nanocrystalline TiO<sub>2</sub> formed from 13 nm particle is observed and Mo:BiVO<sub>4</sub> layer is shown on the right. The presence of Ti, O, Bi and V elements are identified in the EDX spectrum of nc-TiO<sub>2</sub>/Mo:BiVO<sub>4</sub> shown in figure 31 B.

## 3. Investigation of Photoelectrochemical Behavior of Nanocrystalline TiO<sub>2</sub> Coupled to Mo:BiVO<sub>4</sub> electrodes

To investigate the photoelectrochemical behavior of nc-TiO<sub>2</sub>/Mo:BiVO<sub>4</sub> electrodes, %IPCE and I-V curves measurements were performed in 0.5 M Na<sub>2</sub>SO<sub>4</sub> in 0.1 M Na<sub>2</sub>SO<sub>3</sub>. Figure 32 A shows the average and best film of highest % IPCE of nc-TiO<sub>2</sub> / Mo:BiVO<sub>4</sub> at 0.6 V vs Ag/AgCl in back-wall light illumination. The onset photocurrent occurs at 500 and generally plateau with max %IPCE between 340 - 440

nm. The %IPCE of the best Mo:BiVO<sub>4</sub> film equals 57.33 % at 360 nm, and after nc-TiO<sub>2</sub> addition, it decreased to 49.03 % at 380 nm. Moreover, the average %IPCE of Mo:BiVO<sub>4</sub> films equal  $33.15 \pm 21.30$  % (N = 3) at 360 nm, and it decreases with the addition of nc-TiO<sub>2</sub> to  $32.77 \pm 12.74$  % (N = 3) at 380 nm.

The photocurrent declined by a factor to  $0.85 \pm 0.069$  after nc -TiO<sub>2</sub> addition on Mo:BiVO<sub>4</sub> electrode at total average % IPCE between 300-500nm. A decline in photocurrent is observed for nc-TiO<sub>2</sub>/Mo:BiVO<sub>4</sub> to a factor 0.84 in best film % IPCE between 300-500 nm. This indicates that adding nc-TiO<sub>2</sub> as second layer to Mo:BiVO<sub>4</sub> does not result in enhancement in light harvesting.



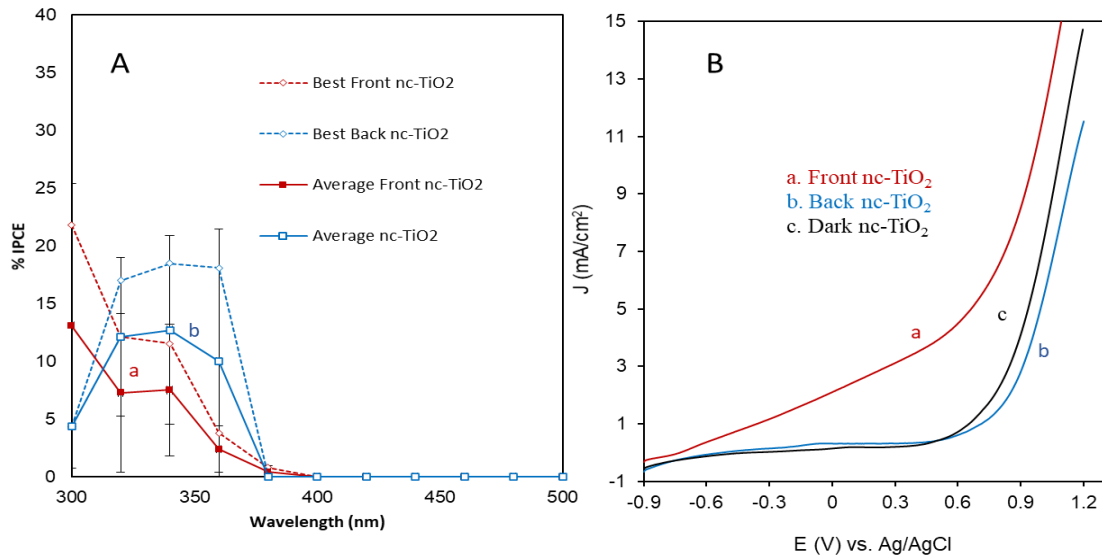
**Figure 32.** %IPCE at 0.6 V vs Ag/AgCl of (A) average and best film (highest %IPCE) bilayer nc-TiO<sub>2</sub> / Mo:BiVO<sub>4</sub> with its best film (B) I-V curves in the dark and back light illumination at 100 mW/cm<sup>2</sup> intensity of a scan rate 10 mV/s. Electrolyte solution is 0.5 M Na<sub>2</sub>SO<sub>4</sub> in 0.1 M Na<sub>2</sub>SO<sub>3</sub> solution (pH ~ 9.63).

Figure 32 B represents I -V curves of the best film in %IPCE of nc-TiO<sub>2</sub>/Mo:BiVO<sub>4</sub> in the dark and with back-wall light illumination at 100 mW/cm<sup>2</sup> intensity in sulfate sulfite solution. The onset potential cathodically shifts from -0.426 V vs Ag/AgCl to -0.439 V vs Ag/AgCl after the addition of the nc-TiO<sub>2</sub> on the Mo:BiVO<sub>4</sub> as

shown in Figure 32 B. The current density of Mo:BiVO<sub>4</sub> at 0.6 V vs Ag/AgCl is 4.02 mA/cm<sup>2</sup> and after nc-i-TiO<sub>2</sub> addition, it decreases to 3.47 mA/cm<sup>2</sup> as shown in Figure 32 B. The photocurrent declined by a factor of 0.86 after nc-TiO<sub>2</sub> addition on Mo:BiVO<sub>4</sub> electrode. The current densities in this I-V curve also resulted in a similar decline in photocurrent as observed in % IPCE. Therefore, the enhancement was caused by the structural ordered inverse opals rather than a heterojunction with non-scattering nanocrystalline TiO<sub>2</sub>.

#### 4. The Effect of nc-TiO<sub>2</sub> on the Photoelectrochemical Behavior

To better understand the reason behind the decline in photocurrent that occurs after coupling Mo:BiVO<sub>4</sub> with nc-TiO<sub>2</sub>, I-V curves and %IPCE measurements of the background nc-TiO<sub>2</sub> were performed in sulfate sulfite electrolyte.



**Figure 33.** %IPCE at 0.6 V vs Ag/AgCl of (A) average and best film (highest %IPCE) nc-TiO<sub>2</sub> with its best film (B) I-V curves in the dark and back light illumination at 100 mW/cm<sup>2</sup> intensity of a scan rate 10 mV/s. Electrolyte solution is 0.5 M Na<sub>2</sub>SO<sub>4</sub> in 0.1 M Na<sub>2</sub>SO<sub>3</sub> solution (pH ~ 9.63).

Figure 33 A shows the average and best film % IPCE of nc-TiO<sub>2</sub>-g at 0.6 V vs Ag/AgCl in back and front light illumination. The photocurrent onsets at 380 - 400 nm and it maximizes at 340 nm then decreases to reach 5% at 300 nm when the electrode is illuminated from the back as shown in Figure 33 A. However, when the electrode is illuminated from the front, the %IPCE continues to increase up to 300 nm as shown in Figure 33 A. The best film % IPCE in front-wall illumination equaled 21.77% at 300 nm as shown in Figure 33 A. The best film % IPCE in back-wall illumination equaled 18.48% at 340 nm. The % IPCE of the background nc-TiO<sub>2</sub>-g at 400 nm is zero whether the electrode is illuminated from the back or from the front. The average %IPCE in front-wall illumination equaled  $7.51 \pm 5.71$  % (N=2) at 300 nm as shown in Figure 33 A. The average % IPCE in back-wall illumination equaled  $12.70 \pm 8.17$  % (N=2) at 340 nm. The average % IPCE of the background nc-TiO<sub>2</sub>-g at 400 nm is zero whether the electrode is illuminated from the back or from the front which is consistent with the absorption of TiO<sub>2</sub> and the decrease at shorter wavelength in back-wall light illumination is attributed to absorbance from FTO.

Figure 33 B shows the I -V curves of the nc-TiO<sub>2</sub> alone in the dark with both front and back light illumination at 100 mW/cm<sup>2</sup> intensity in sulfate sulfite solution. The onset potential is at -0.687 V vs Ag/AgCl in back illumination, and at -0.736 V vs Ag/AgCl in front illumination. This indicates that the onset potential shift that was reported for nc-TiO<sub>2</sub>/Mo:BiVO<sub>4</sub> is due to the absorption of TiO<sub>2</sub>. The current density of nc-TiO<sub>2</sub> at 0.6V vs Ag/AgCl equaled 1.43 mA/cm<sup>2</sup> upon back light illumination and it equaled 2.03 mA/cm<sup>2</sup> upon front light illumination as shown in Figure 33 B. The reason why the nc-TiO<sub>2</sub> coupled to Mo:BiVO<sub>4</sub> did not cause an enhancement in the photocurrent despite the heterojunction could be caused due to the small size of the nc-

TiO<sub>2</sub> which hindered the contact of Mo:BiVO<sub>4</sub> with electrolyte or the absence of a transport path from this film to FTO. Therefore, it is shown that it is mainly the structural order in inverse opals rather than scattering in a disordered film or heterojunction with non-scattering nanocrystalline TiO<sub>2</sub> that caused the enhancement in light harvesting.

### **E. Mo:BiVO<sub>4</sub> Coupled to Ordered TiO<sub>2</sub> of Varied Stop Band**

To further investigate the effect of the stop band position relative to Mo:BiVO<sub>4</sub> on photocurrent enhancement, starting from 305 nm, 227 nm, and 150 nm polystyrene sphere size, TiO<sub>2</sub> inverse opals coupled to Mo:BiVO<sub>4</sub> were prepared.

#### ***1. UV-Vis Absorption Spectra of 150 nm, 227 nm, 305 Sphere Size Inverse Opals Coupled to Mo:BiVO<sub>4</sub>***

In Figure 34 A, 305 nm polystyrene spheres were assembled with similar preparation to that of 282-i-TiO<sub>2</sub>-o/Mo:BiVO<sub>4</sub> leading to 305-i-TiO<sub>2</sub>-o/Mo:BiVO<sub>4</sub> of thickness equals  $3.63 \pm 1.25 \mu\text{m}$ . Upon evaporation induced self-assembly at 55 °C of PC<sub>305</sub> on Mo:BiVO<sub>4</sub> layer, the stop band peak was at 695 nm as shown in Figure 34 A (b). After the liquid-phase deposition replication followed by calcination at 400 °C for 8 hours, it shifted to a broad peak at 594 nm for 305-i-TiO<sub>2</sub>-o/Mo:BiVO<sub>4</sub> as shown in Figure 34 A (a). The stop band peaks observed in the UV-Visible spectra in Figure 34 A are due to the order in PC and inverse opals.

In Figure 34 B, 227 nm polystyrene spheres were assembled with similar preparation to that of 282-i-TiO<sub>2</sub>-o/Mo:BiVO<sub>4</sub> leading to 227-i-TiO<sub>2</sub>-o/Mo:BiVO<sub>4</sub> of thickness equals  $2.4 \pm 0.99 \mu\text{m}$ . Upon evaporation induced self-assembly at 55 °C of PC<sub>227</sub> on Mo:BiVO<sub>4</sub> layer, the stop band peak was at 506 nm as shown in Figure 34 B

(b). After the liquid-phase deposition replication followed by calcination at 400 °C for 8 hours, it shifts toward the blue region and it is not differentiated from Mo:BiVO<sub>4</sub> absorbance peaks at 440 nm for 227-i-TiO<sub>2</sub>-o/Mo:BiVO<sub>4</sub> as shown in Figure 34 B (a). The SEM image later discussed in Figure 35 A shows air hole size of 162 nm, this would correspond to a stop band peak for 227-i-TiO<sub>2</sub>-o at 452 nm.

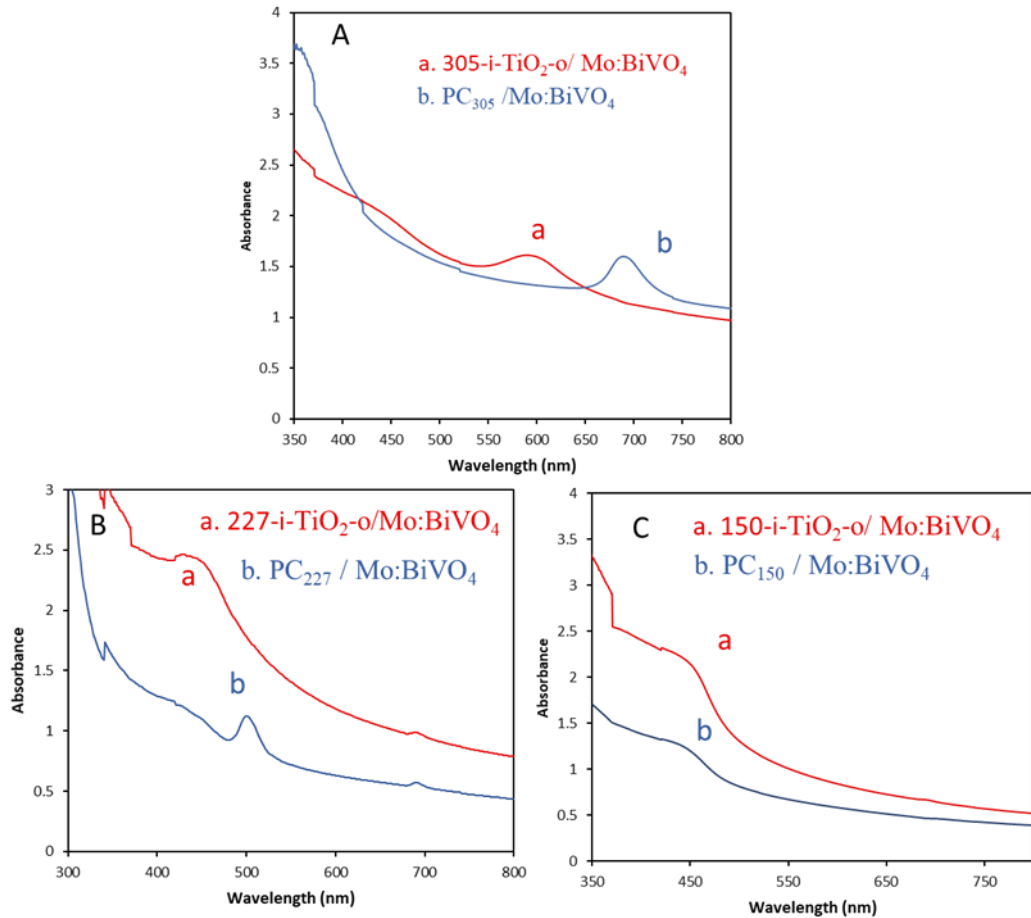


**Figure 34.** UV-Vis absorption spectra of (A) 305-i-TiO<sub>2</sub>-o/Mo:BiVO<sub>4</sub> (a) and (b) PC<sub>305</sub>/Mo:BiVO<sub>4</sub>, (B) 227-i-TiO<sub>2</sub>-o/Mo:BiVO<sub>4</sub> (a) and (b) PC<sub>227</sub>/Mo:BiVO<sub>4</sub> and (C) 150-i-TiO<sub>2</sub>-o/Mo:BiVO<sub>4</sub> (a) and (b) PC<sub>150</sub>/Mo:BiVO<sub>4</sub>

In Figure 34 C, 150 nm polystyrene spheres were assembled with similar preparation to that of 305-i-TiO<sub>2</sub>-o/Mo:BiVO<sub>4</sub> leading to 150-i-TiO<sub>2</sub>-o/Mo:BiVO<sub>4</sub> of thickness equals  $3.63 \pm 1.25 \mu\text{m}$ . Upon evaporation induced self-assembly at 55 °C of

PC<sub>150</sub> on Mo:BiVO<sub>4</sub> layer, only a peak was observed at 455 nm as shown in Figure 34 C (b) corresponding to Mo:BiVO<sub>4</sub>. The stop band peak of PC<sub>150</sub> position is to the blue region of Mo:BiVO<sub>4</sub> absorbance. After the liquid-phase deposition replication followed by calcination at 400 °C for 8 hours appeared a broad peak at 444 nm for 150-i-TiO<sub>2</sub>-o/Mo:BiVO<sub>4</sub> is attributed to Mo:BiVO<sub>4</sub> as shown in Figure 34 C (a).

## ***2. SEM and EDX Characterization of Bilayer 305-i-TiO<sub>2</sub>-o/Mo:BiVO<sub>4</sub>, 227-i-TiO<sub>2</sub>-o/Mo:BiVO<sub>4</sub> and 150-i-TiO<sub>2</sub>-o/Mo:BiVO<sub>4</sub>***

SEM images were taken to study the morphology of different TiO<sub>2</sub> photonic crystals from different sizes coupled to Mo:BiVO<sub>4</sub>. Figure 35 A shows an SEM image of PC<sub>305</sub>/Mo:BiVO<sub>4</sub> of thickness equals  $5.6 \pm 2.9 \mu\text{m}$  where a highly ordered assembly of spheres of average diameter ( $0.289 \pm 0.01 \mu\text{m}$ ). This film was also coated by 7 nm gold for SEM imaging purpose using a sputtering machine. Figure 35 D shows EDX spectrum indicating the presence of Au, in addition to the presence of Bi, O and V. The % shrinkage is 5.25%. According to Bragg's equation, the stop band peak corresponds to 0.262  $\mu\text{m}$  diameter polystyrene spheres which also indicates shrinkage of the photonic crystal sphere size. Figure 35 B shows SEM image of 305-i-TiO<sub>2</sub>-o/Mo:BiVO<sub>4</sub> of thickness  $3.6 \pm 1.25 \mu\text{m}$ . The thickness of the film always decreased after infiltration. The air-hole size measurements from the SEM image in figure 35 C shows an average diameter of  $0.239 \pm 0.008 \mu\text{m}$ . The % shrinkage is 27.61%. According to Bragg's equation, the diameter of the air holes equals 0.213  $\mu\text{m}$  which also indicates shrinkage. The presence of Ti, O, Bi and V elements of the bilayer are identified in EDX spectrum in figure 35 E.

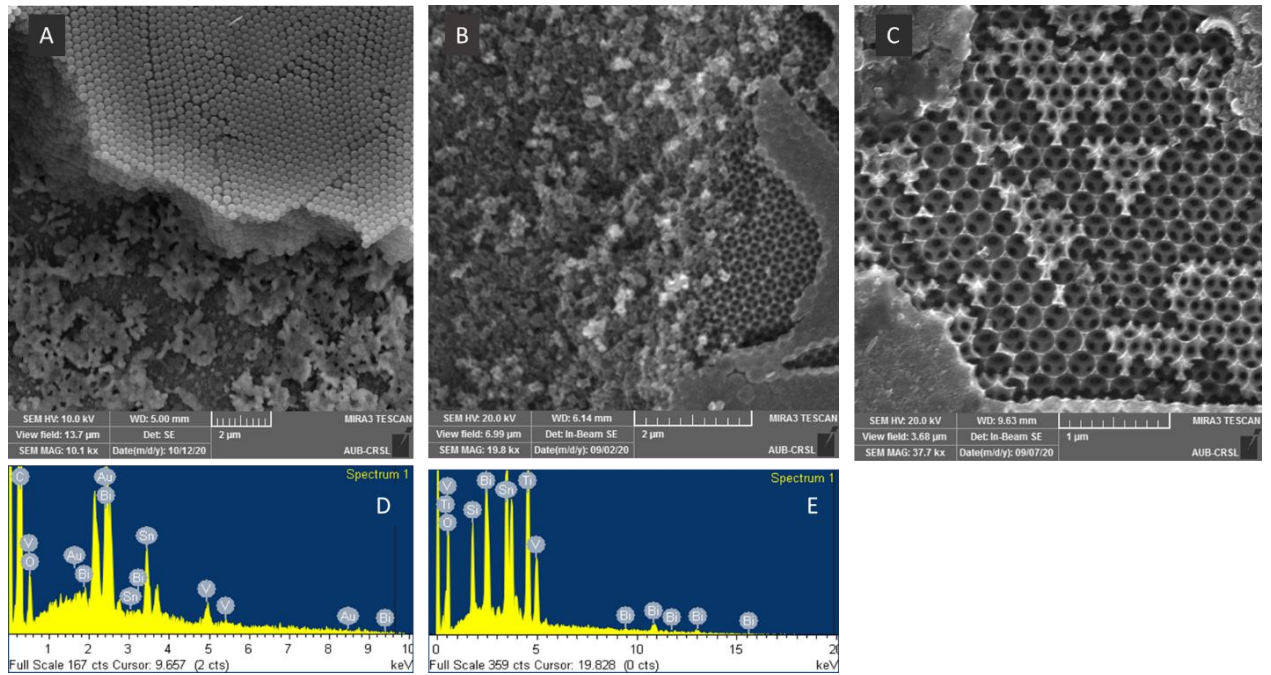


**Figure 35.** SEM images of (A) PC<sub>305</sub>/Mo:BiVO<sub>4</sub> ( $5.6 \pm 2.9 \mu\text{m}$ ), (B) bilayer 305-i-TiO<sub>2</sub>-o/Mo:BiVO<sub>4</sub> ( $3.6 \pm 1.25 \mu\text{m}$ ) with their EDX spectra (D and E) respectively and (C) inverse opal structures of 305 nm sphere size with average air-hole diameter  $0.239 \pm 0.008 \mu\text{m}$

Figure 36 shows SEM images bilayers of ordered inverse opals from 150 nm (A) and 227 nm (B) on top of Mo:BiVO<sub>4</sub>. Figure 36 A and B have similar bilayer structure of ordered inverse opals. EDX spectra are presentation of Figure 36 (C and D) and indicate the presence of Ti and O corresponding to TiO<sub>2</sub>. They also indicate the presence of Mo, Bi ,V , O corresponding to Mo:BiVO<sub>4</sub>. The large thickness of 150-i-TiO<sub>2</sub>-o/Mo:BiVO<sub>4</sub> maybe due to some photonic crystals that did not undergo infiltration well.

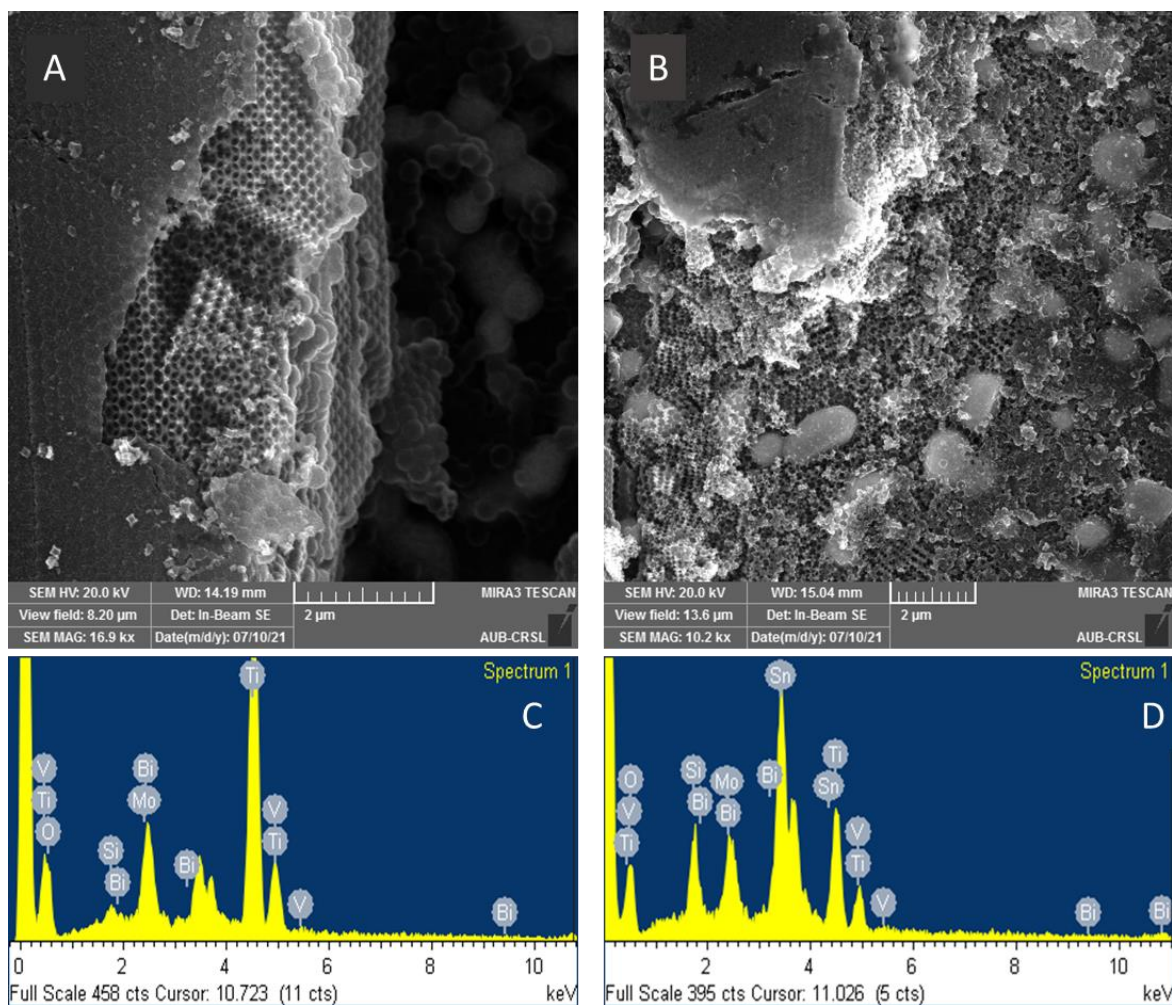


**Figure 36.** SEM images of (A) bilayer 150-i-TiO<sub>2</sub>-o/Mo:BiVO<sub>4</sub> ( $5.57 \pm 1.28 \mu\text{m}$ ), and (B) bilayer 227-i-TiO<sub>2</sub>-o/Mo:BiVO<sub>4</sub> ( $2.40 \pm 0.99 \mu\text{m}$ ) and with their EDX spectra (C and D) respectively

### 3. Investigation of Photoelectrochemical Behavior of 305nm , 227nm and 150 nm

#### *Sphere Size TiO<sub>2</sub> Inverse Opals Coupled to Mo:BiVO<sub>4</sub> electrodes*

To understand the photoelectrochemical behavior of 305-i-TiO<sub>2</sub>-o, 227-i-TiO<sub>2</sub>-o and 150-i-TiO<sub>2</sub>-o coupled to of Mo:BiVO<sub>4</sub> electrodes, %IPCE and I-V curves measurements were performed in sulfate sulfite electrolyte (pH~ 9.63). Figure 37 A shows the average and best film of highest % IPCE of 305-i-TiO<sub>2</sub>-o/ Mo:BiVO<sub>4</sub> at 0.6 V vs Ag/AgCl in back-wall light illumination. The onset photocurrent occurs at 500 nm

and generally plateau with max %IPCE between 340 - 450 nm. The %IPCE of the best Mo:BiVO<sub>4</sub> film equaled 45.18 % at 380 nm, and after 305-i-TiO<sub>2</sub>-o addition, it increased to 97.60% at 440 nm. Moreover, the average %IPCE of Mo:BiVO<sub>4</sub> films equaled  $43.98 \pm 6.78$  % (N = 4) at 380 nm, and it increases with the addition of 305-i-TiO<sub>2</sub>-o to  $83.49 \pm 12.10$  % (N = 4) at 400 nm.

The photocurrent increased by a factor of  $1.83 \pm 0.39$  after 305-i-TiO<sub>2</sub>-o addition on Mo:BiVO<sub>4</sub> electrode at total average % IPCE between 300-500nm. An improvement in photocurrent is observed for 305-i-TiO<sub>2</sub>-o/Mo:BiVO<sub>4</sub> by a factor of 2.14 enhancement in best film % IPCE between 300-500 nm. This indicates that the enhancement was caused by structural ordered TiO<sub>2</sub> inverse opals, the internal light trapping and backscattering in the 305-i-TiO<sub>2</sub>-o/Mo:BiVO<sub>4</sub>.

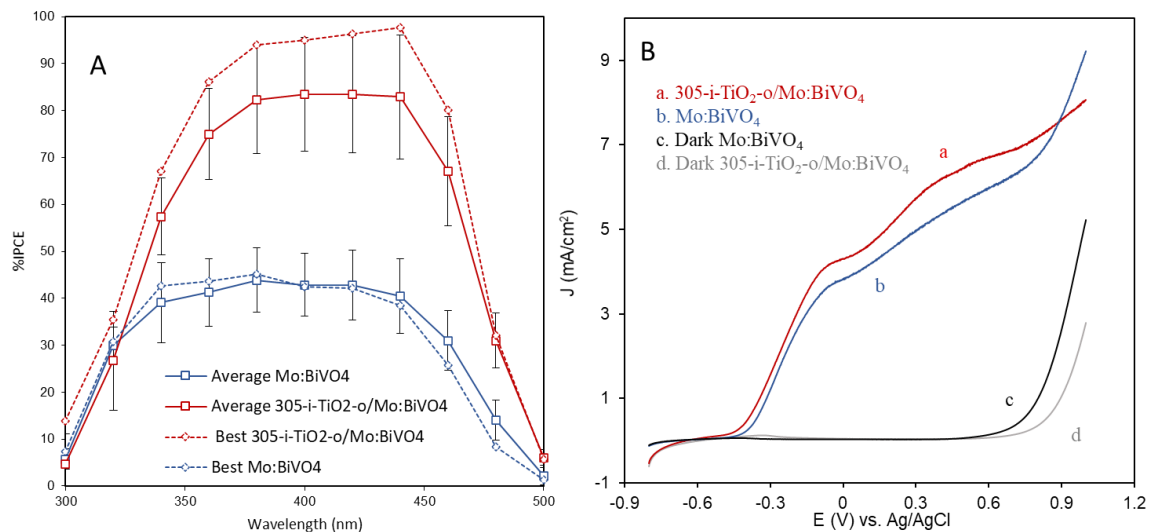


**Figure 37.** %IPCE vs wavelength (nm) at 0.6 V vs Ag/AgCl of (A) average and best film ( highest %IPCE ) bilayer 305-i-TiO<sub>2</sub>-g/ Mo:BiVO<sub>4</sub>, with its best film I-V curves (B) in dark and under back illumination in 0.5 M Na<sub>2</sub>SO<sub>4</sub> in 0.1 M Na<sub>2</sub>SO<sub>3</sub> solution (pH ~ 9.63). The scan rate is 10 mV/s.

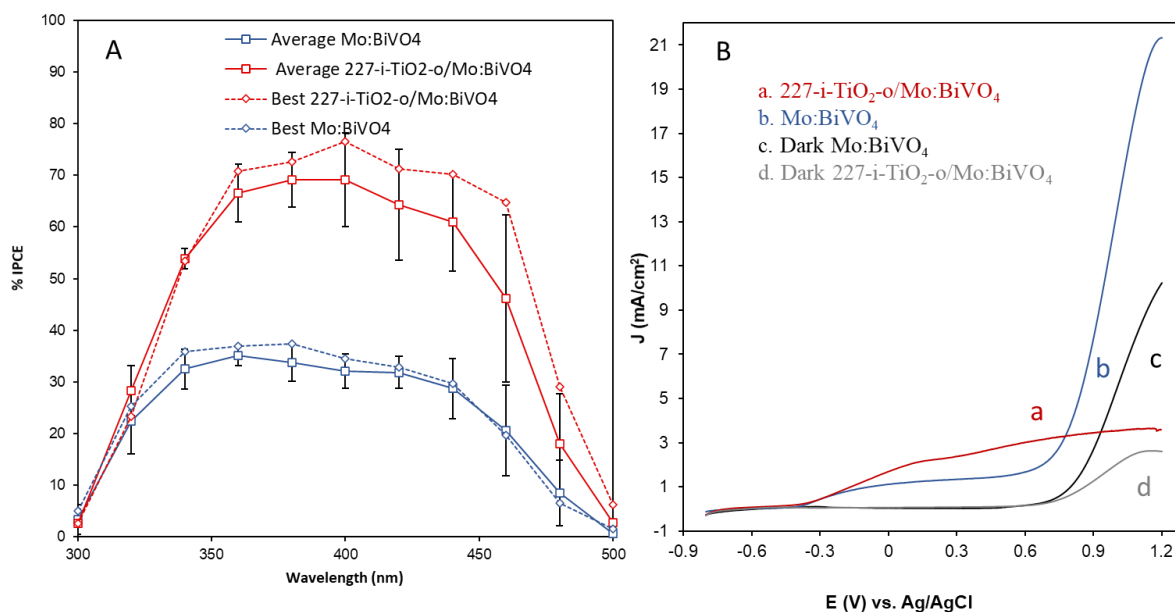
The photocurrent gain after 282-i-TiO<sub>2</sub>-o addition on Mo:BiVO<sub>4</sub> electrode is greater than the photocurrent gain after 305-i-TiO<sub>2</sub>-o addition on Mo:BiVO<sub>4</sub> electrode in both total average and best % IPCE between 300-500nm.

Figure 37 B represents I -V curves of the best film in %IPCE of 305-i-TiO<sub>2</sub>-o/Mo:BiVO<sub>4</sub> in the dark and with back-wall light illumination at 100 mW/cm<sup>2</sup> intensity in sulfate sulfite solution. The onset potential cathodically shifts from -0.461 V vs Ag/AgCl to -0.508 V vs Ag/AgCl after the addition of the ordered TiO<sub>2</sub> inverse opals on the Mo:BiVO<sub>4</sub> as shown in Figure 37 B. The current density of Mo:BiVO<sub>4</sub> at 0.6 V vs Ag/AgCl is 5.83 mA/cm<sup>2</sup> and after 305-i-TiO<sub>2</sub>-o addition it increases to 6.64 mA/cm<sup>2</sup> as shown in Figure 37 B. The photocurrent enhanced by a factor of 1.13 after 305-i-TiO<sub>2</sub>-o addition on Mo:BiVO<sub>4</sub> electrode. The current densities in this I-V curve resulted in an enhancement in the photocurrent lower than the one observed in best % IPCE.

Figure 38 A shows the average and best film of highest % IPCE of 227-i-TiO<sub>2</sub>-o/ Mo:BiVO<sub>4</sub> at 0.6 V vs Ag/AgCl in back-wall light illumination. The onset photocurrent occurs at 500 nm and generally plateau with max %IPCE between 340 - 450 nm. The %IPCE of the best Mo:BiVO<sub>4</sub> film equals 37.32 % at 380 nm, and after 227-i-TiO<sub>2</sub>-o addition, it increased to 76.55 % at 400 nm. Moreover, the average %IPCE of Mo:BiVO<sub>4</sub> films equal  $35.19 \pm 1.96$  % (N = 3) at 360 nm, and it increases with the addition of 227-i-TiO<sub>2</sub>-o to  $69.12 \pm 9.05$  % (N = 3) at 400 nm.

The photocurrent increased by a factor of  $1.93 \pm 0.27$  after 227-i-TiO<sub>2</sub>-o addition on Mo:BiVO<sub>4</sub> electrode at total average % IPCE between 300-500nm. An improvement in photocurrent is observed for 227-i-TiO<sub>2</sub>-o/Mo:BiVO<sub>4</sub> by a factor of 2.03 enhancement in best film % IPCE between 300-500 nm. This indicates that the enhancement was caused by structural ordered TiO<sub>2</sub> inverse opals, the internal light

trapping and backscattering in the 227-i-TiO<sub>2</sub>-o/Mo:BiVO<sub>4</sub>. The photocurrent gain after 282-i-TiO<sub>2</sub>-o addition on Mo:BiVO<sub>4</sub> electrode is greater than the photocurrent gain after 227-i-TiO<sub>2</sub>-o addition on Mo:BiVO<sub>4</sub> electrode in both total average and best % IPCE between 300-500nm. However, the photocurrent gain after 227-i-TiO<sub>2</sub>-o addition on Mo:BiVO<sub>4</sub> electrode is greater than the photocurrent gain after 305-i-TiO<sub>2</sub>-o addition on Mo:BiVO<sub>4</sub> electrode in both total average and best % IPCE between 300-500nm.

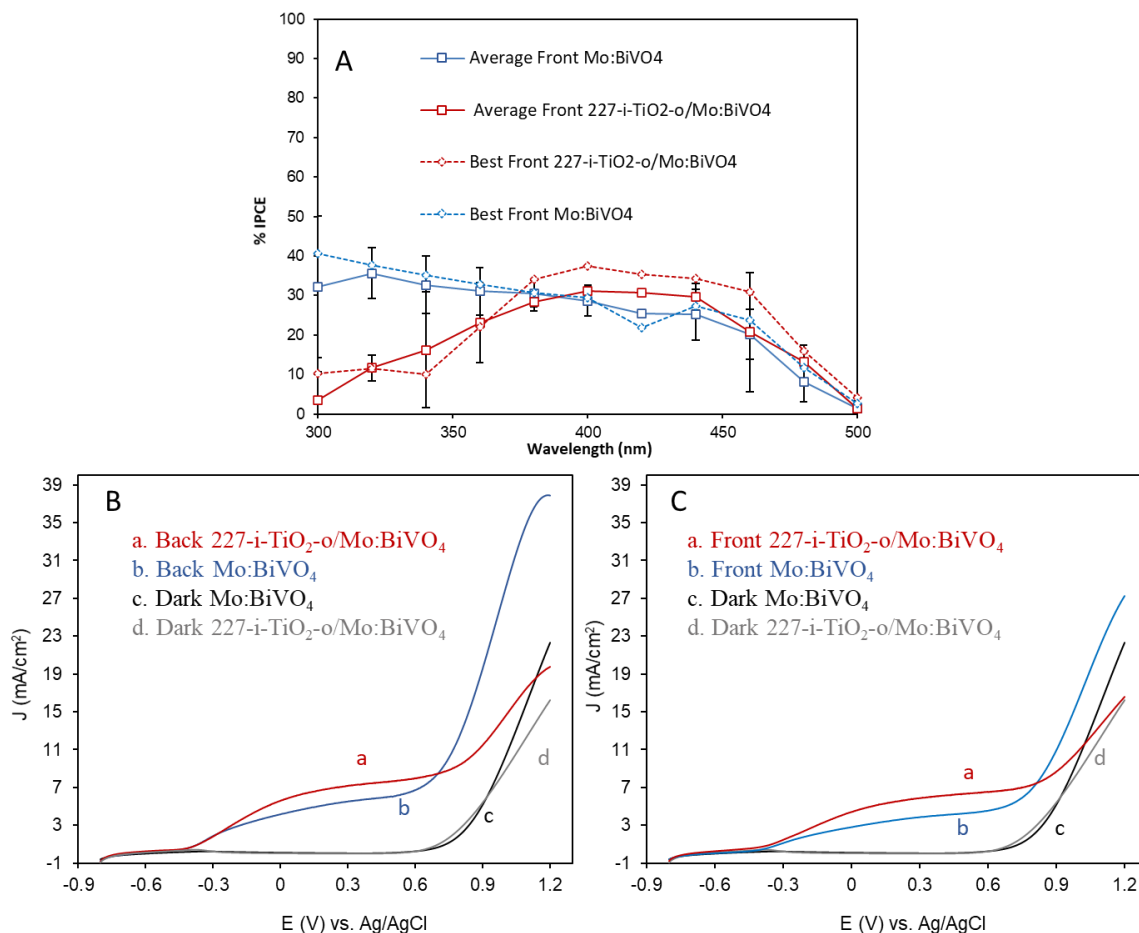


**Figure 38.** %IPCE vs wavelength (nm) at 0.6 V vs Ag/AgCl of (A) average and best film (highest %IPCE) bilayer 227-i-TiO<sub>2</sub>-g/Mo:BiVO<sub>4</sub>, with its best film I-V curves (B) in dark and under back illumination in 0.5 M Na<sub>2</sub>SO<sub>4</sub> in 0.1 M Na<sub>2</sub>SO<sub>3</sub> solution (pH ~ 9.63). The scan rate is 10 mV/s.

Figure 38 B represents I -V curves of the best film in %IPCE of 227-i-TiO<sub>2</sub>-o/Mo:BiVO<sub>4</sub> in the dark and with back-wall light illumination at 100 mW/cm<sup>2</sup> intensity in sulfate sulfite solution. The onset potential cathodically shifts from -0.365 V vs Ag/AgCl to -0.413 V vs Ag/AgCl after the addition of the ordered TiO<sub>2</sub> inverse opals on the Mo:BiVO<sub>4</sub> as shown in Figure 38 B. The current density of Mo:BiVO<sub>4</sub> at 0.6 V vs Ag/AgCl equaled 1.50 mA/cm<sup>2</sup> and after 227-i-TiO<sub>2</sub>-o addition it increases to 2.83

$\text{mA/cm}^2$  as shown in Figure 38 B. The photocurrent enhanced by a factor of 1.89 after  $\text{i-TiO}_2\text{-o}$  addition on  $\text{Mo:BiVO}_4$  electrode. The current densities in this I-V curve resulted in an enhancement in the photocurrent lower than the one observed in best % IPCE.

The difference in the photoelectrochemical behavior between front-wall and back-wall illumination was studied for the  $\text{227-i-TiO}_2\text{-o/ Mo:BiVO}_4$  in sulfate sulfite solution. Figure 38 A shows the average and best film of highest % IPCE of  $\text{227-i-TiO}_2\text{-o/ Mo:BiVO}_4$  at 0.6 V vs Ag/AgCl in front-wall illumination. The onset photocurrent occurs at 500 nm and generally plateau with max %IPCE between 360 – 450 nm and in  $\text{Mo:BiVO}_4$  in front-wall illumination reached maximum at 300 – 320 nm. The %IPCE of the best  $\text{Mo:BiVO}_4$  film equals 40.61 % at 300 nm, and after  $\text{227-i-TiO}_2\text{-o}$  addition, it decreased to 37.37 % at 400 nm. Moreover, the average %IPCE of  $\text{Mo:BiVO}_4$  films equal  $35.58 \pm 6.17$  % (N = 3) at 320 nm, and it decreases with the addition of  $\text{227-i-TiO}_2\text{-o}$  to  $31.06 \pm 9.02$  % (N = 3) at 380 nm. The photocurrent declined to a factor of  $0.82 \pm 0.36$  after  $\text{227-i-TiO}_2\text{-o}$  addition on  $\text{Mo:BiVO}_4$  electrode at total average % IPCE between 300-500nm. A decline in photocurrent is observed for  $\text{227-i-TiO}_2\text{-o/Mo:BiVO}_4$  to a factor of 0.84 enhancement in best film % IPCE between 300-500 nm. This indicates that structural ordered  $\text{TiO}_2$  inverse opals in front-wall did not enhance the photocurrent but, it caused a decline may be due to forward scattering being less important than backscattering in  $\text{227-i-TiO}_2\text{-o/Mo:BiVO}_4$ , and Bragg reflection reducing light intensity at  $\text{Mo:BiVO}_4$ . The enhancement of bilayer  $\text{227-i-TiO}_2\text{-o/Mo:BiVO}_4$  is both %IPCE and I-V curves therefore occurs in back-wall illumination rather than in front-wall illumination.



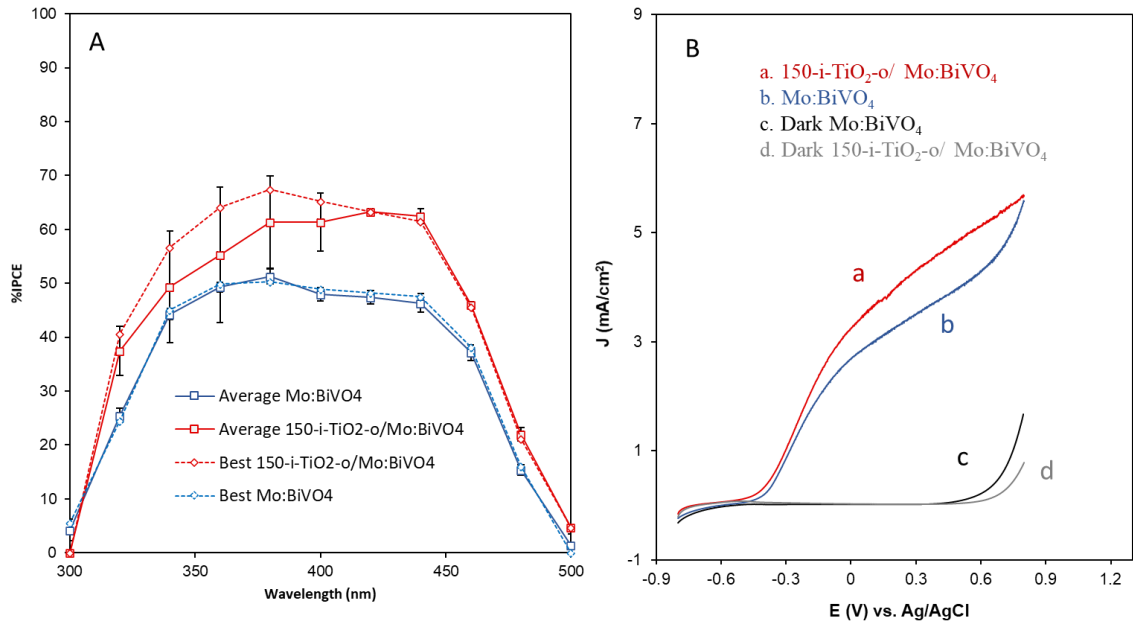
**Figure 39.** %IPCE vs wavelength (nm) at 0.6 V vs Ag/AgCl of (A) average and best film (highest %IPCE) bilayer 227-i-TiO<sub>2</sub>-g/Mo:BiVO<sub>4</sub> under front illumination, with its best film I-V curves in dark and (B) under back illumination and (C) under front illumination in 0.5 M Na<sub>2</sub>SO<sub>4</sub> in 0.1 M Na<sub>2</sub>SO<sub>3</sub> solution (pH ~ 9.63). The scan rate is 10 mV/s.

Figure 39 B represents I -V curves of the best film in %IPCE of 227-i-TiO<sub>2</sub>-o/Mo:BiVO<sub>4</sub> in the dark and with back-wall light illumination at 100 mW/cm<sup>2</sup> intensity in sulfate sulfite solution. The onset potential cathodically shifts from -0.42 V vs Ag/AgCl to -0.498 V vs Ag/AgCl after the addition of the ordered TiO<sub>2</sub> inverse opals on the Mo:BiVO<sub>4</sub> as shown in Figure 39 B. The current density of Mo:BiVO<sub>4</sub> at 0.6 V vs Ag/AgCl equaled 6.46 mA/cm<sup>2</sup> and after 227-i-TiO<sub>2</sub>-o addition, it increases to 7.69

mA/cm<sup>2</sup> as shown in Figure 39 B. The photocurrent increased by a factor of 1.19 after 227-i-TiO<sub>2</sub>-o addition on Mo:BiVO<sub>4</sub> electrode.

Figure 39 C represents I -V curves of the best film in %IPCE of 227-i-TiO<sub>2</sub>-o/ Mo:BiVO<sub>4</sub> in the dark and with front-wall light illumination at 100 mW/cm<sup>2</sup> intensity in sulfate sulfite solution. The onset potential cathodically shifts from -0.42 V vs Ag/AgCl to -0.434 V vs Ag/AgCl after the addition of the ordered TiO<sub>2</sub> inverse opals on the Mo:BiVO<sub>4</sub> as shown in Figure 39 C. The current density of Mo:BiVO<sub>4</sub> at 0.6 V vs Ag/AgCl equaled 4.29 mA/cm<sup>2</sup> and after 227-i-TiO<sub>2</sub>-o addition, it increases to 6.26 mA/cm<sup>2</sup> as shown in Figure 39 C. The photocurrent enhanced by a factor of 1.46 after 227-i-TiO<sub>2</sub>-o addition on Mo:BiVO<sub>4</sub> electrode. The current densities in this I-V curve show a small enhancement in the photocurrent while the % IPCE plots show a small decline in Figure 39 A.

Figure 40 A shows the average and best film of highest % IPCE of 150-i-TiO<sub>2</sub>-o/ Mo:BiVO<sub>4</sub> at 0.6 V vs Ag/AgCl in back-wall light illumination. The onset photocurrent occurs at 500 nm and generally plateau with max %IPCE between 340 - 450 nm. The %IPCE of the best Mo:BiVO<sub>4</sub> film equals 50.26 % at 380 nm, and after 150-i-TiO<sub>2</sub>-o addition, it increased to 67.43 % at 380 nm. Moreover, the average %IPCE of Mo:BiVO<sub>4</sub> films equal 51.28 ± 1.45 % (N = 2) at 380 nm, and it increases with the addition of 150-i-TiO<sub>2</sub>-o to 63.35 ± 0 % (N = 3) at 420 nm.



**Figure 40.** %IPCE vs wavelength (nm) at 0.6 V vs Ag/AgCl of (A) average and best film (highest %IPCE) bilayer 150-i-TiO<sub>2</sub>-g/Mo:BiVO<sub>4</sub>, with its best film I-V curves (B) in dark and under back illumination in 0.5 M Na<sub>2</sub>SO<sub>4</sub> in 0.1 M Na<sub>2</sub>SO<sub>3</sub> solution (pH ~ 9.63). The scan rate is 10 mV/s.

The photocurrent enhanced by a factor of  $1.25 \pm 0.084$  after 150-i-TiO<sub>2</sub>-o addition on Mo:BiVO<sub>4</sub> electrode at total average % IPCE between 300-500nm. An improvement in photocurrent is observed for 150-i-TiO<sub>2</sub>-o/Mo:BiVO<sub>4</sub> by a factor of 1.31 enhancement in best film % IPCE between 300-500 nm. This indicates that the enhancement was caused by structural ordered TiO<sub>2</sub> inverse opals, the internal light trapping and backscattering in the 150-i-TiO<sub>2</sub>-o/Mo:BiVO<sub>4</sub>. The photocurrent gain after the addition 282-i-TiO<sub>2</sub>-o, 227-i-TiO<sub>2</sub>-o, and 305-i-TiO<sub>2</sub>-o on Mo:BiVO<sub>4</sub> electrodes are greater than the photocurrent gain after 150-i-TiO<sub>2</sub>-o addition on Mo:BiVO<sub>4</sub> electrode in both total average and best % IPCE between 300-500nm respectively. Therefore, the enhancement in photocurrent was affected by variation of stop band, but even by varying the photonic crystal sphere from 305 nm, 282 nm, 227nm to 150 nm the photocurrent enhancement was observed.

Figure 40 B represents I -V curves of the best film in %IPCE of 150-i-TiO<sub>2</sub>-o/Mo:BiVO<sub>4</sub> in the dark and with back-wall light illumination at 100 mW/cm<sup>2</sup> intensity in sulfate sulfite solution. The onset potential cathodically shifts from -0.484 V vs Ag/AgCl to -0.509 V vs Ag/AgCl after the addition of the ordered TiO<sub>2</sub> inverse opals on the Mo:BiVO<sub>4</sub> as shown in Figure 40 B. The current density of Mo:BiVO<sub>4</sub> at 0.6 V vs Ag/AgCl equaled 4.06 mA/cm<sup>2</sup> and after 150-i-TiO<sub>2</sub>-o addition, it increases to 5.04 mA/cm<sup>2</sup> as shown in Figure 40 B. The photocurrent enhanced by a factor of 1.24 after -i-TiO<sub>2</sub>-o addition on Mo:BiVO<sub>4</sub> electrode. The current densities in this I-V curve resulted in an enhancement in the photocurrent lower than the one observed in % IPCE in Figure 40 A.

#### **D. Conclusions**

In this study, we investigated of the effect of TiO<sub>2</sub> photonic crystals of varying stop bands on light harvesting at Mo:BiVO<sub>4</sub> films, in a photoelectrochemical cell in the presence of hole scavenger (sulfate sulfite solution ) to minimize the kinetics limitations. The stop band was varied by changing the sphere size in the polystyrene opal template and the effect of TiO<sub>2</sub> inverse opal on the light-to-current conversion efficiency of Mo:BiVO<sub>4</sub> was compared to the effect of coupling to disordered inverse glass and non-scattering nanocrystalline TiO<sub>2</sub> films. It is concluded from these studies that:

- 1) The enhancement in photocurrent was caused by structural ordered TiO<sub>2</sub> inverse opals and is attributed to the internal light trapping and backscattering in the i-TiO<sub>2</sub>-o/Mo:BiVO<sub>4</sub>.

- 2) Under white light illumination from 300 W Xenon lamp of  $100 \text{ mA/cm}^2$  intensity, it was shown that absorption of light by inverse opal  $\text{TiO}_2$  in the bilayer can lead to photocurrent generation and affects both the photocurrent onset and the photocurrent.
- 3) The absence of an enhancement for  $\text{Mo:BiVO}_4$  prepared using the second deposition method (cast) which resulted in a more packed structure, can possibly be attributed to this morphology not allowing as much infiltration of  $\text{TiO}_2$  in  $\text{Mo:BiVO}_4$ .
- 4) As the thickness of  $\text{Mo:BiVO}_4$  increased ( its initial %IPCE is higher), as the film structure was more packed, the enhancement of the photocurrent caused by coupling i- $\text{TiO}_2$ -o decreases.
- 5) The gain at 400 nm and the longer wavelength measured in %IPCE is all due to the coupling effect of the i- $\text{TiO}_2$ -o with  $\text{Mo:BiVO}_4$  electrodes. On the other hand, under back-wall white light illumination, a certain amount of photocurrent at shorter wavelength can be due to  $\text{TiO}_2$ .
- 6) The photocurrent enhancement that happened in the best 282-i- $\text{TiO}_2$ -g/ $\text{Mo:BiVO}_4$  film was caused by the possibility of back-scattering effect in the disordered 282-i- $\text{TiO}_2$ -g. However, higher enhancement in photocurrent was caused by the structural ordered inverse opals rather than only scattering at disordered domains.
- 7) Although scattering occurred in the disordered films but it is maybe that there was a greater backscattering in ordered inverse opals. The effect cannot be caused directly by Bragg reflection since the stop band peak is located toward the red region through it extends over a broad frequency range.

- 8) The I-V curves of 282-i-TiO<sub>2</sub>-g/Mo:BiVO<sub>4</sub> electrodes showed a contribution from 282-i-TiO<sub>2</sub>-g making contact with FTO or photogenerated charges from TiO<sub>2</sub> absorbance. While in % IPCE plots, photocurrents enhancement at 380 nm and longer wavelength originated from Mo:BiVO<sub>4</sub> and shorter wavelengths can have contribution from TiO<sub>2</sub>.
- 9) The role of NaCl was proven to decrease the photocurrent of 282-i-TiO<sub>2</sub>-g/Mo:BiVO<sub>4</sub> by possible incorporation. And some possible enhancement in the photocurrent maybe caused by disordered structure, but it may be masked by NaCl/calcination.
- 10) The NaCl presence could not be the full cause why the 282-i-TiO<sub>2</sub>-g/Mo:BiVO<sub>4</sub> film did not cause ca. 2-fold gain as observed with 282-i-TiO<sub>2</sub>-o/Mo:BiVO<sub>4</sub>.
- 11) Adding nc-TiO<sub>2</sub> as second layer to Mo:BiVO<sub>4</sub> does not result in enhancement in light harvesting. The enhancement in photocurrent was caused by the structural ordered inverse opals rather than a heterojunction with non-scattering nanocrystalline TiO<sub>2</sub>.
- 12) The reason why the nc-TiO<sub>2</sub> coupled to Mo:BiVO<sub>4</sub> did not cause an enhancement in the photocurrent despite the heterojunction could be due to the small size of the nc-TiO<sub>2</sub> which hindered the contact of Mo:BiVO<sub>4</sub> with the electrolyte or the absence of a transport path from the nc-TiO<sub>2</sub>/Mo:BiVO<sub>4</sub> film to FTO.
- 13) It is mainly the structural order in inverse opals rather than scattering in a disordered film or heterojunction with non-scattering nanocrystalline TiO<sub>2</sub> that caused the enhancement in light harvesting.

- 14) The enhancement in photocurrent of bilayer 227-i-TiO<sub>2</sub>-o/Mo:BiVO<sub>4</sub> is much greater when both %IPCE and I-V curves in back-wall illumination rather than in front-wall illumination. The structural ordered TiO<sub>2</sub> inverse opals in front-wall did not enhance the photocurrent but, it caused a decline may be due to forward scattering being less important than backscattering in 227-i-TiO<sub>2</sub>-o/Mo:BiVO<sub>4</sub>, and Bragg reflection reducing light intensity at Mo:BiVO<sub>4</sub>.
- 15) The enhancement in photocurrent was affected by variation of stop band but even by varying the photonic crystal sphere from 305 nm, 282 nm , 227nm to 150 nm , the photocurrent enhancement was observed.

## CHAPTER IV

### INVESTIGATION OF OER CATALYSIS AT Ni-B<sub>i</sub> ON THE Mo:BiVO<sub>4</sub> PHOTOANODE COUPLED TO TiO<sub>2</sub> PHOTONIC CRYSTAL IN POTASSIUM BORATE ELCTROLYTE

Previous studies show that Ni-based oxides have proven their high catalytic activity with a promoting effect after the incorporation of a guest metal.<sup>63</sup> By coupling oxygen evolution catalysts Co-Pi and Ni-B<sub>i</sub>, a significant enhancement on the semiconductor photocatalytic performance has been shown.<sup>54</sup> Choi *et.al* studies showed that a maximum IPCE of 30% was recorded after photodeposition (PD) of Ni-B<sub>i</sub> for 3min on BiVO<sub>4</sub> in comparison to 15% at the bare BiVO<sub>4</sub> films. A significant decrease in the produced photocurrent was also noted at very high deposition times in 0.1 M potassium borate (pH=9.2 ).<sup>64</sup> Ni-B<sub>i</sub> functions as a recombination center when Ni-B<sub>i</sub> film is thick.<sup>55</sup> It was investigated that PD of Ni-B<sub>i</sub> on BiVO<sub>4</sub> in PEC water oxidation play a dual role on increasing photocurrent and lowering bias.<sup>55</sup> First, it mediates the hole transfer which inhibits the recombination of electron-hole pairs photogenerated at BiVO<sub>4</sub>, and it results in a change in the Ni oxidation state from lower (Ni<sup>2+</sup> and Ni<sup>3+</sup>) to higher states (Ni<sup>3+</sup> and Ni<sup>4+</sup>), which then results in water oxidation. Other studies were performed by an in situ electrodeposition method of synthesized Ni-doped on BiVO<sub>4</sub>.<sup>65</sup> A decrease in the particle size of BiVO<sub>4</sub> and the formation of V<sup>4+</sup> species/oxygen defects were reported due to the effect of Ni-doping.<sup>65</sup> A higher %IPCE value of 45% was obtained after Ni-doping, while only 25% for BiVO<sub>4</sub> without doping at 400 nm.<sup>65</sup> Some studies were performed to understand the doping effect of nickel in TiO<sub>2</sub>.<sup>66</sup> It was reported that TiO<sub>2</sub> particle sizes increased and the band gap energy decreased from

3.2 eV to 2.86 eV which shifts the absorption of TiO<sub>2</sub> in the visible region due to the 0.05 mole% Ni<sup>2+</sup> doping on TiO<sub>2</sub> that enhance solar applications.<sup>66</sup>

Thus, this chapter focuses on studying the photoelectrochemical behavior of bilayer i-TiO<sub>2</sub>-o/Mo:BiVO<sub>4</sub> of modified Ni-B<sub>i</sub> co-catalyst on water oxidation. The effect of the i-TiO<sub>2</sub>-o and Ni-B<sub>i</sub> OER catalyst in borate buffer compared to Ni-B<sub>i</sub>/ spread Mo:BiVO<sub>4</sub> and Ni-B<sub>i</sub>/ cast Mo:BiVO<sub>4</sub> photoanodes was studied.

### **A. Effect of Ni-B<sub>i</sub> OER Co-Catalyst on the Mo:BiVO<sub>4</sub> Photoanode Coupled to TiO<sub>2</sub> Photonic Crystal**

Ni-B<sub>i</sub> as OER catalyst was coupled to 282-i-TiO<sub>2</sub>-o/Mo:BiVO<sub>4</sub> and the photoelectrochemical (PEC) behavior was studied in borate buffer (pH= 9.16 ) with and without Ni-B<sub>i</sub> at Mo:BiVO<sub>4</sub> and at the bilayer i-TiO<sub>2</sub>-o/Mo:BiVO<sub>4</sub>.

#### ***1. Characterization of Ni-Bi/282-i-TiO<sub>2</sub>-o/Mo:BiVO<sub>4</sub> electrode***

Figure 41 shows the SEM images of the bilayer Ni-282-i-TiO<sub>2</sub>-o/Mo:BiVO<sub>4</sub> with its EDX spectrum. This film was prepared by immersing the 282-i-TiO<sub>2</sub>-o/Mo:BiVO<sub>4</sub> electrode in 0.1 M KBi electrolyte (pH ~ 9.16) with 0.4 mM Ni(NO<sub>3</sub>)<sub>2</sub> and subjecting to white light from 300 W Xenon lamp with an intensity of 100 mW/cm<sup>2</sup> with front illumination for 3 minutes. Then the electrode was rinsed with deionized water to obtain Ni-282-i-TiO<sub>2</sub>-o/Mo:BiVO<sub>4</sub> (2.36 ± 0.74 μm). Figure 41 A shows the inverse opals structure of the bilayer 282-i-TiO<sub>2</sub>-o/Mo:BiVO<sub>4</sub>. Figure 41 B show a combination formed between Mo:BiVO<sub>4</sub> and the 282 nm sphere size inverse opals. EDX spectrum of the bilayer Ni-B<sub>i</sub>/282-i-TiO<sub>2</sub>-o/Mo:BiVO<sub>4</sub> in Figure 41 C was

performed to verify the presence of Ni , Bi , V , Ti , and O elements. All elements were confirmed.

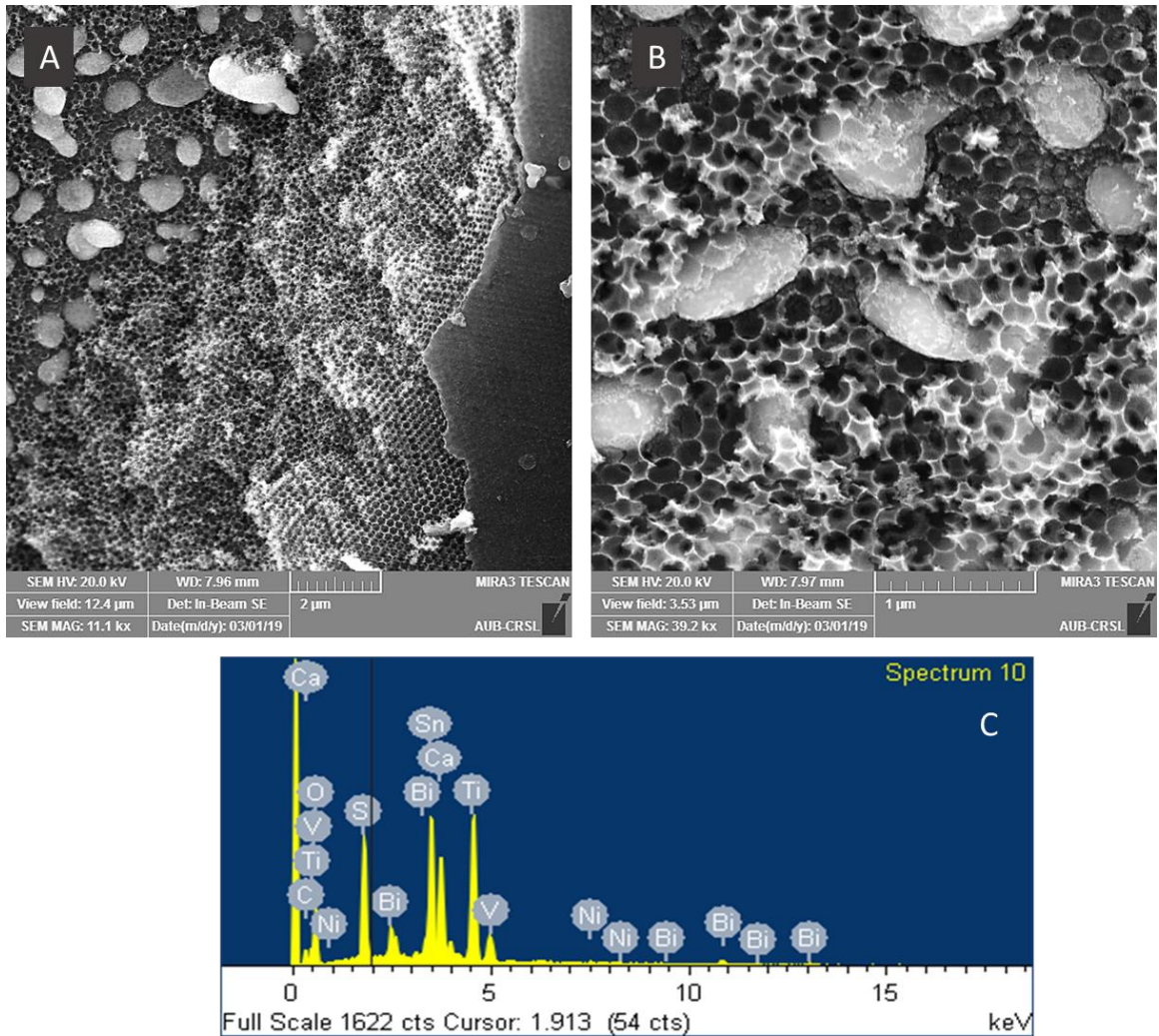


**Figure 41.** SEM images of (A) bilayer Ni-Bi/282-i-TiO<sub>2</sub>-o/Mo:BiVO<sub>4</sub>(2.36 ± 0.74 μm) , (B) inverse opals 282nm TiO<sub>2</sub>/ Mo:BiVO<sub>4</sub>, with its EDX spectrum (C)

## 2. Photoelectrochemical Behavior of 282-i-TiO<sub>2</sub>-o/Mo:BiVO<sub>4</sub> Photoanode before and after Ni-Bi Photodeposition

Figure 42 A show the average %IPCE of 282-i-TiO<sub>2</sub>-o/ Mo:BiVO<sub>4</sub> (N=7) before and after the photodeposition of Ni-Bi acquired in 1M KBi electrolyte pH ~ 9.16. The photocurrent onset occurs at 500 - 520 nm, and generally plateau with max %IPCE

between 380 - 440 nm. And Figure 42 B shows the best film among the averaged films that reached the highest %IPCE reached in Ni-B<sub>i</sub>/ 282-i-TiO<sub>2</sub>-o / Mo:BiVO<sub>4</sub>. The %IPCE of the best Mo:BiVO<sub>4</sub> film equaled 22.35 % at 420nm, and after 282-i-TiO<sub>2</sub>-o addition, it increased to 32.63 %. Then after Ni-B<sub>i</sub> photodeposition, it increased to 47.83%. Moreover, the average %IPCE of Mo:BiVO<sub>4</sub> films equaled  $16.91 \pm 4.68$  % (N = 7) and increased with the addition of 282 nm sphere size inverse opal to  $21.90 \pm 5.89$  % (N = 7) at 400 nm. And after the Ni-B<sub>i</sub> photodeposition, it further increased to  $38.35 \pm 5.65$  % (N = 7) at 400 nm

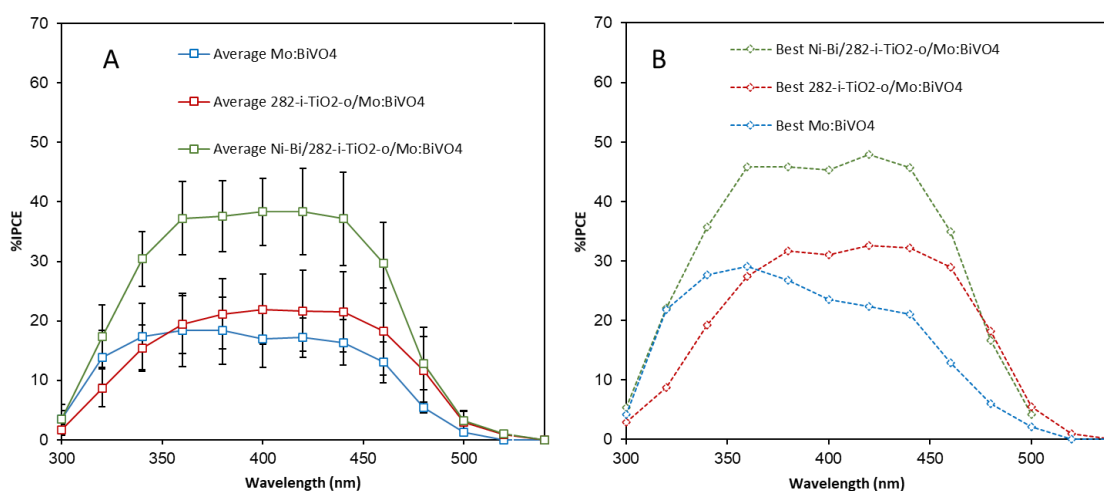


**Figure 42.** %IPCE at 0.6 V vs Ag/AgCl of (A) Average of Ni-B<sub>i</sub> coupled to bilayer 282-i-TiO<sub>2</sub>-o/Mo:BiVO<sub>4</sub> and (B) best Film of Ni-B<sub>i</sub> coupled to bilayer 282-i-TiO<sub>2</sub>-o/Mo:BiVO<sub>4</sub>. Electrolyte is 1M KB<sub>i</sub> (pH=9.16).

The photocurrent was enhanced by a factor of  $1.22 \pm 0.34$  after 282-i-TiO<sub>2</sub>-o addition on Mo:BiVO<sub>4</sub> electrode determined from the total average % IPCE between 300-500nm. It is noted that the enhancement of the bilayer in sulfate sulfite ( $2.21 \pm 0.53$ ) is much greater than the enhancement of the bilayer in borate electrolyte. Despite the gain in light harvesting in 1 M KB<sub>i</sub>, kinetics limitation from sluggish water oxidation resulted in a significant smaller effect of increasing absorbance. An improvement in photocurrent is observed for 282-i-TiO<sub>2</sub>-o/Mo:BiVO<sub>4</sub> after PD of Ni-B<sub>i</sub>

relative to Mo:BiVO<sub>4</sub> by a factor of  $2.09 \pm 0.48$  enhancement in total average % IPCE between 300-500 nm. Moreover, the total average %IPCE of 282-i-TiO<sub>2</sub>-o/Mo:BiVO<sub>4</sub> after PD of Ni-B<sub>i</sub> relative to 282-i-TiO<sub>2</sub>-o/Mo:BiVO<sub>4</sub> was enhanced by a factor of  $1.78 \pm 0.28$  at 300-500 nm. The gain that occurred after the PD of Ni-B<sub>i</sub> on bilayer can be attributed to a decrease in surface electron - hole recombination that is caused by the co-catalyst Ni-B<sub>i</sub>, and Ni-B<sub>i</sub> could be acting as a co-catalyst after scavenging the hole from Mo:BiVO<sub>4</sub>.<sup>55</sup>

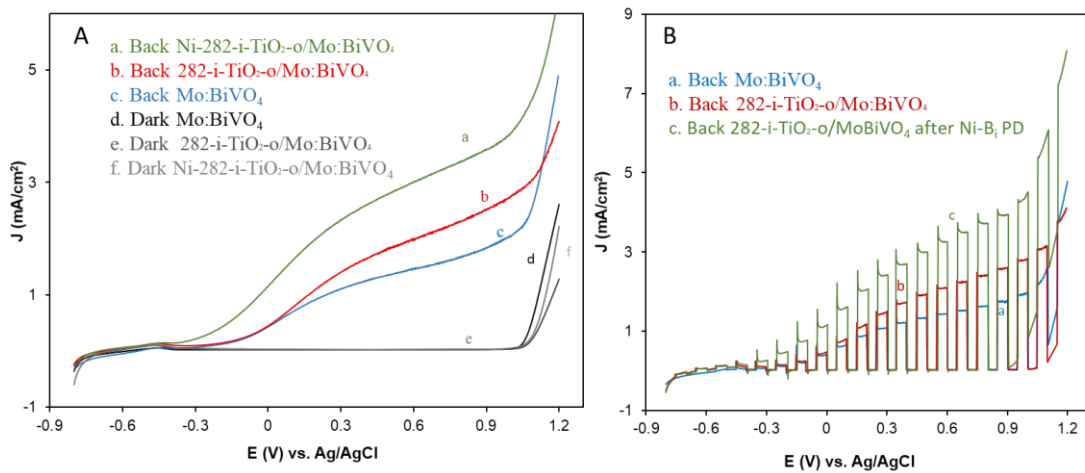


**Figure 43.** Cyclic voltammograms (A) of the best film in %IPCE of 282-i-TiO<sub>2</sub>-o/Mo:BiVO<sub>4</sub> before and after the photodeposition of Ni-B<sub>i</sub> in the dark and with back light illumination at 100 mW/cm<sup>2</sup> intensity along with its (B) linear sweep voltammograms under chopped light irradiation for 3 min . The Scan rate is 10 mV/s.

Figure 43 A represents I -V curves of the best film in %IPCE of 282-i-TiO<sub>2</sub>-o/Mo:BiVO<sub>4</sub> before and after the photodeposition of Ni-B<sub>i</sub> in the dark and with back white light illumination at 100 mW/cm<sup>2</sup> intensity in 1 M KBi. Table 1 shows the current density at 0.6 V from I-V curves of figure 43 A of Ni-B<sub>i</sub>/282-i-TiO<sub>2</sub>-o/Mo:BiVO<sub>4</sub> in 1 M KB<sub>i</sub> Electrolyte (pH= 9.16). In table 1, the current density of Mo:BiVO<sub>4</sub> at 0.6 V vs Ag/AgCl equaled 1.43 mA/cm<sup>2</sup> and after 282-i-TiO<sub>2</sub>-o addition it increases to 1.97

$\text{mA/cm}^2$ , and reaches  $2.98 \text{ mA/cm}^2$  after the PD of Ni-B<sub>i</sub> as shown in Figure 43 A. While the current density of the Mo:BiVO<sub>4</sub> (N=7) at 0.6 V vs Ag/AgCl equaled  $1.57 \pm 0.59 \text{ mA/cm}^2$  and it increases to  $1.98 \pm 0.41 \text{ mA/cm}^2$  for the bilayer to reach  $2.56 \pm 0.93 \text{ mA/cm}^2$  after PD of Ni-B<sub>i</sub>. The current density increases by  $1.26 \pm 0.67$ -fold after addition of inverse opal. However, after photodeposition it increases to  $1.29 \pm 2.32$ -fold relative to bilayer. Therefore, the average current densities in this I-V curve also resulted in an enhancement as observed in % IPCE. The overall gain in %IPCE is higher than the overall gain by I-V curves.

Table 2 shows the bias shift in I-V curves of figure 43 A of Ni-B<sub>i</sub>/282-i-TiO<sub>2</sub>-o/Mo:BiVO<sub>4</sub> at 0.2 and 0.5  $\text{mA/cm}^2$  in 1 M KBi electrolyte (pH= 9.16). When the current density equals  $0.2 \text{ mA/cm}^2$ , the bias shifts cathodically from -0.117 V vs Ag/AgCl to -0.13 V vs Ag/AgCl after the addition of the 282-i-TiO<sub>2</sub>-o layer. Then after photodeposition of Ni-Bi, it shifted to -0.312 V vs Ag/AgCl as reported in Table 2. However, when the current density equals  $0.5 \text{ mA/cm}^2$ , the bias shifts from 0.024 to 0.017 V vs Ag/AgCl after the addition of the 282-i-TiO<sub>2</sub>-o. After photodeposition of Ni-Bi, it shifted toward -0.165 V vs Ag/AgCl. Therefore, the increase in photocurrent at low bias and the increase saturation (plateau) photocurrent at high bias in I-V can be attributed to the catalytic property of Ni-B<sub>i</sub> alongside the inhibition of electron-hole recombination by the catalyst.

Figure 43 B shows the linear sweep voltammograms (LSV) of the best film in %IPCE of 282-i-TiO<sub>2</sub>-o/ Mo:BiVO<sub>4</sub> before and after the photodeposition of Ni-B<sub>i</sub> under chopped light irradiation for 3 mins. In Figure 43 B, the photocurrent transients are observed upon turning light on and off due to electrons-holes recombination and accumulation of trapped charges. P. Salvador *et. al* explains that this effect occurs due

to electrons accumulating in the bulk region (anodic transient) where light is on and holes accumulating near the surface (cathodic transient) where light is off .<sup>67</sup> The onset potential cathodically shifts from -0.55 V vs Ag/AgCl to -0.75 V vs Ag/AgCl after the addition of the inverse opals on the Mo:BiVO<sub>4</sub>. No shift occurs in the onset potential after three mins PD of Ni-B<sub>i</sub>. Under white light illumination from 300 W Xenon lamp of 100 mA/cm<sup>2</sup> intensity, absorption of light by inverse opal TiO<sub>2</sub> can lead to photocurrent generation and affect both the photocurrent onset and the photocurrent. Therefore, control studies were conducted at 282-i-TiO<sub>2</sub>-o alone where Ni-B<sub>i</sub> was photodeposited on 282-i-TiO<sub>2</sub>-o photoanode similar to the photodeposition on 282-TiO<sub>2</sub>-o/Mo:BiVO<sub>4</sub>.

| Films | Current Density (mA/cm <sup>2</sup> ) at 0.6 V |        |         |                |        |         | Scan Rate ( 10 mV/s)              |        |          |
|-------|--|--------|---------|----------------|--------|---------|-----------------------------------|--------|----------|
|       | Before Photodeposition                         |        |         |                |        |         | After Photodeposition             |        |          |
|       | Mo:BiVO <sub>4</sub>                           |        |         | 282 io bilayer |        |         | Ni-B <sub>i</sub> /282 io bilayer |        |          |
|       | Dark   | Light  |         | Dark           | Light  |         | Dark                              | Light  |          |
| #1    | 0.05972  | 1.50   | 1.45    | 0.06988        | 1.826  | 1.75612 | 0.02996                           | 3.354  | 3.324036 |
| #2    | 0.12328  | 1.4756 | 1.35232 | 0.03248        | 1.6192 | 1.58672 | 0.03154                           | 1.7876 | 1.756064 |
| #3    | 0.37036  | 1.0664 | 0.69604 | 0.02738        | 1.5272 | 1.49982 | 0.04652                           | 2.3108 | 2.26428  |
| #4    | 0.02332  | 2.2088 | 2.18548 | 0.03084        | 2.5112 | 2.48036 | 0.02755                           | 2.9284 | 2.900848 |
| #5    | 0.02485  | 1.4568 | 1.43195 | 0.02367        | 1.994  | 1.97033 | 0.02456                           | 3.0048 | 2.98024  |
| #6    | 0.03728  | 2.5232 | 2.48592 | 0.02953        | 2.5688 | 2.53927 | 0.02603                           | 3.6968 | 3.670772 |
| #7    | 0.03248  | 1.4316 | 1.39912 | 0.02764        | 2.084  | 2.05636 | 1.4316                            | 2.4656 | 1.034    |

| Average (mA/cm <sup>2</sup> ) at 0.6 V |                |                             |
|--|----------------|-----------------------------|
| Mo:BiVO <sub>4</sub>                   | 282 io bilayer | Ni-B <sub>i</sub> / bilayer |
| 1.57 ± 0.59                            | 1.98 ± 0.41    | 2.56 ± 0.93                 |

**Table 1.** Current density at 0.6 V of I-V curves of figure 43 A of Ni-B<sub>i</sub>/282-i-TiO<sub>2</sub>-o/Mo:BiVO<sub>4</sub> in 1 M KB<sub>i</sub> electrolyte (pH= 9.16)

| Ni-B <sub>i</sub> /282-i-TiO <sub>2</sub> -o/Mo:BiVO <sub>4</sub> |                      |                | at 0.2 mA/cm <sup>2</sup>          |
|---|----------------------|----------------|------------------------------------|
| Figure 43<br>Film # 5   | Before PD            |                | After PD                           |
|   | Mo:BiVO <sub>4</sub> | 282 io bilayer | Ni-B <sub>i</sub> / 282 io bilayer |
|   | Light                | Light          | Light                              |
| <i>J</i> (mA/cm <sup>2</sup> )                                    | 0.20064              | 0.20092        | 0.20052                            |
| <i>E</i> (V) vs Ag/AgCl   | -0.117               | -0.13          | -0.312                             |

| Ni-B <sub>i</sub> /282-i-TiO <sub>2</sub> -o/Mo:BiVO <sub>4</sub> |                      |                | at 0.5 mA/cm <sup>2</sup>          |
|---|----------------------|----------------|------------------------------------|
| Figure 43<br>Film # 5   | Before PD            |                | After PD                           |
|   | Mo:BiVO <sub>4</sub> | 282 io bilayer | Ni-B <sub>i</sub> / 282 io bilayer |
|   | Light                | Light          | Light                              |
| <i>J</i> (mA/cm <sup>2</sup> )                                    | 0.5032               | 0.5            | 0.5032                             |
| <i>E</i> (V) vs Ag/AgCl   | 0.024                | 0.017          | -0.165                             |

**Table 2.** Bias shift in I-V curves of figure 43 A of Ni-B<sub>i</sub>/282-i-TiO<sub>2</sub>-o/Mo:BiVO<sub>4</sub> at 0.2 and 0.5 mA/cm<sup>2</sup> in 1 M KB<sub>i</sub> electrolyte (pH= 9.16)

### 3. The Effect of 282-i-TiO<sub>2</sub>-o on the Photoelectrochemical Behavior Before and After Ni-B<sub>i</sub> Photodeposition

Figure 44 A shows the LSV of 282-i-TiO<sub>2</sub>-o before and after PD of Ni-B<sub>i</sub> for 3 mins in 1M KB<sub>i</sub> electrolyte. When the current density equals 0.05 mA/cm<sup>2</sup>, the bias shifts from -0.39 V vs Ag/AgCl to -0.38 V vs Ag/AgCl after 3 mins photodeposition of Ni-B<sub>i</sub> on the 282-i-TiO<sub>2</sub>-o electrode in back light illumination as shown in Figure 44 A. However, the bias shifts cathodically from -0.413 V vs Ag/AgCl to -0.414 vs Ag/AgCl at 0.2 mA/cm<sup>2</sup> current density after PD of Ni-B<sub>i</sub> in front light illumination. A peak was observed in figure 44 A in both front and back light illumination after PD of Ni-B<sub>i</sub> is attributed to oxidation of Ni(OH)<sub>2</sub> to NiOOH. In front illumination, at a potential equal to 0.824 V vs Ag/AgCl and a current density equal to 0.352 mA/cm<sup>2</sup> a sharp oxidation peak was observed. Similarly, a broader peak was observed when the current density equals 0.552 mA/cm<sup>2</sup> at a potential of 0.805 V vs Ag/AgCl upon back illumination after PD of Ni-B<sub>i</sub>. These peaks were only observed after PD of Ni-B<sub>i</sub> on 282-i-TiO<sub>2</sub>-o alone

and no peaks were observed in figure 43 A corresponding to inverse opals Mo:BiVO<sub>4</sub> after PD of Ni-B<sub>i</sub>. These peaks are due to the effect of the Ni-B<sub>i</sub> catalyst on the TiO<sub>2</sub> and it seems that the peaks are masked or hidden by the presence of Mo:BiVO<sub>4</sub>.

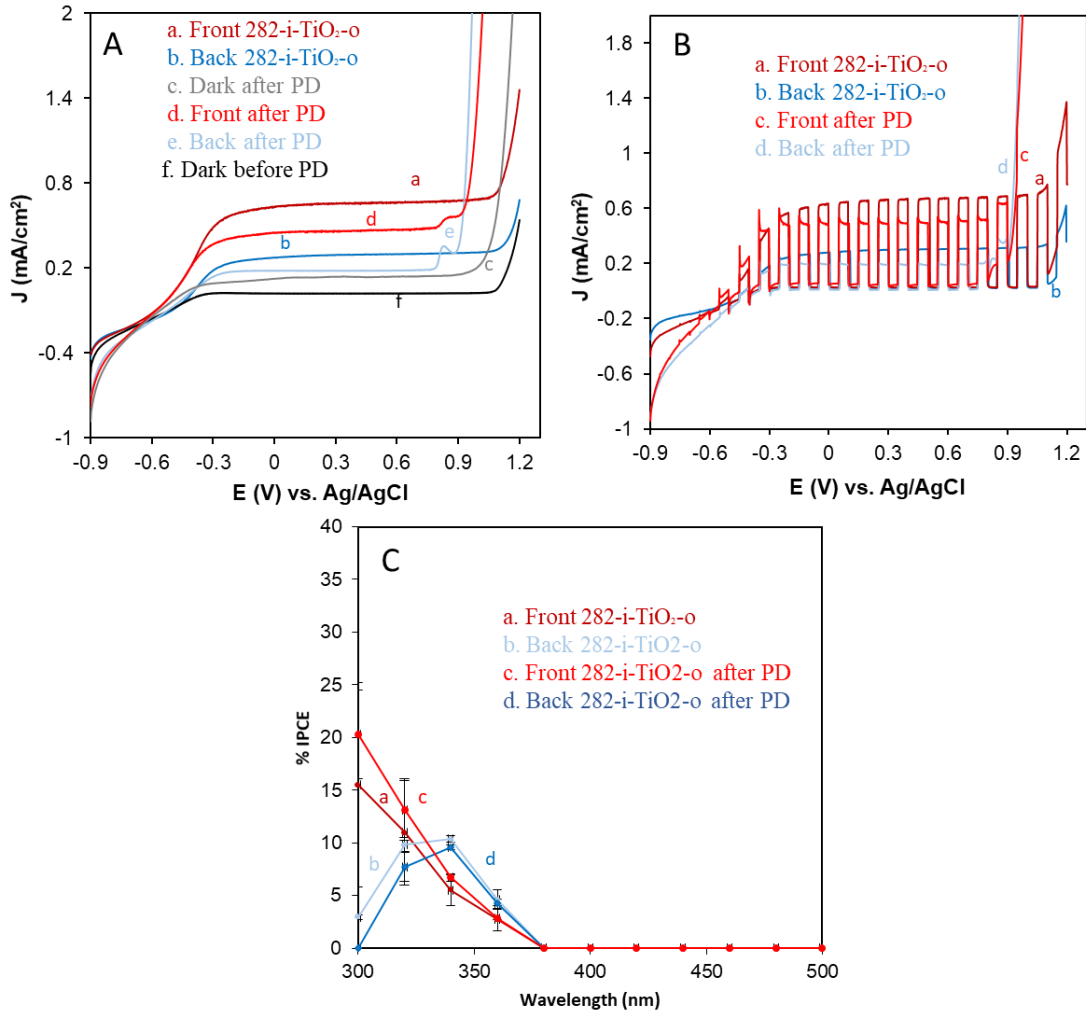


**Figure 44.** Cyclic voltammograms of (A) 282-i-TiO<sub>2</sub>-o in dark and upon light under front and back illumination of 10 mV/s scan rate before and after PD Ni-B<sub>i</sub>, (B) along with linear sweep voltammograms under chopped light irradiation for 3 min and (A) %IPCE vs wavelength (nm) in 1M KB<sub>i</sub> (pH=9.16).

The current density of 282-i-TiO<sub>2</sub>-o at 0.6V vs Ag/AgCl is 1.43 mA/cm<sup>2</sup>, it decreases to 0.0437 mA/cm<sup>2</sup> after the PD of Ni-B<sub>i</sub> as shown in Figure 44 A in back-wall illumination. Similarly, upon front illumination, the current density of 282-i-TiO<sub>2</sub>-o at 0.6V vs Ag/AgCl is 0.641 mA/cm<sup>2</sup>, it decreases to 0.33 mA/cm<sup>2</sup> after the PD of Ni-B<sub>i</sub>.

Therefore, no enhancement occurs, but a decline in the current density is observed after 3 mins of PD of Ni-B<sub>i</sub> in both front and back illumination. The current densities of 282-i-TiO<sub>2</sub>-o are smaller than the observed ones in Figure 44 related to 282-i-TiO<sub>2</sub>-o/Mo:BiVO<sub>4</sub> after PD of Ni-B<sub>i</sub>. Figure 44 B shows the LSV under 3 min chopped light of 282-i-TiO<sub>2</sub>-o before and after PD of Ni-B<sub>i</sub> for 3 mins in 1M KB<sub>i</sub> electrolyte in both front and back illumination. In front illumination, the onset potential before and after PD of Ni-B<sub>i</sub> on the 282-i-TiO<sub>2</sub>-o alone equals -0.76 V vs Ag/AgCl. Similarly in back illumination, the onset potential equals -0.76 V vs Ag/AgCl before and after PD of Ni-B<sub>i</sub> as shown in Figure 44 B. This indicates that the onset potential shift that was reported before for 282-i-TiO<sub>2</sub>-o/Mo:BiVO<sub>4</sub> is due to the absorption of TiO<sub>2</sub> only.

Figure 44 C shows the % IPCE of the background 282-i-TiO<sub>2</sub>-o under back-wall and front-wall light illumination before and after PD of Ni-B<sub>i</sub> in 1M KB<sub>i</sub>. The photocurrent onset at 380 nm and it maximizes at 340 nm then decreases to reach zero at 300 nm when the electrode is illuminated from the back. However, when the electrode is illuminated from the front, the %IPCE continues to increase up to 300 nm as shown in Figure 44 C. The average %IPCE in front-wall illumination before PD equaled to  $15.49 \pm 9.67$  % (N=2) at 300 nm, and after PD it increased to  $20.28 \pm 4.23$  % (N=2) at 300 nm. An improvement in photocurrent for Ni-B<sub>i</sub>/282-i-TiO<sub>2</sub>-o relative to 282-i-TiO<sub>2</sub>-o by a factor of  $1.34 \pm 0.44$  enhancement was measured in the total average % IPCE between 300-500 nm. The average % IPCE in back-wall illumination before PD equaled to  $10.34 \pm 0.30$  % (N=2) at 340 nm, while after PD it decreased to  $9.54 \pm 0.22$  % (N=2) at 340 nm. No improvement of light harvesting was observed in back illumination after PD. The % IPCE of the background 282-i-TiO<sub>2</sub>-o at 400 nm is zero whether the electrode is illuminated from the back or from the front. To be noted that

the onset at 380 nm is consistent with  $\text{TiO}_2$  absorbance ( $E_g = 3.2 \text{ eV}$ ) and the %IPCE values are lower than the values obtained with the presence of  $\text{Mo:BiVO}_4$ . The %IPCE was slightly enhanced by Ni- $\text{Bi}_i$  deposition in the front illumination and not in back illumination is due to possible different recombination rates in  $\text{TiO}_2$  at different illumination direction. It is noted that the enhancement in %IPCE with Ni- $\text{Bi}_i$  was not recorded at higher illumination intensity with white light and could be related to the effect of charge carrier on recombination. To further investigate the role of Ni- $\text{Bi}_i$  co-catalyst on the water oxidation reaction and the reason that lead to the photocurrent enhancement of Ni- $\text{Bi}_i/282\text{-i-TiO}_2\text{-o/Mo:BiVO}_4$ , Ni- $\text{Bi}_i$  was photodeposited on bare  $\text{Mo:BiVO}_4$  photoanode alone similar to the photodeposition on  $282\text{-TiO}_2\text{-o/Mo:BiVO}_4$ .

## B. Effect of Ni- $\text{Bi}_i$ OER Co-Catalyst on the $\text{Mo:BiVO}_4$ Photoanode

### 1. Characterization of Ni- $\text{Bi}_i/\text{Mo:BiVO}_4$ electrode

Figure 45 A shows an SEM image of Ni- $\text{Bi}_i$  coupled to  $\text{Mo:BiVO}_4$ . Figure 45 B shows an EDX spectrum which was performed on the film in Figure 45 A to identify the presence of Ni.

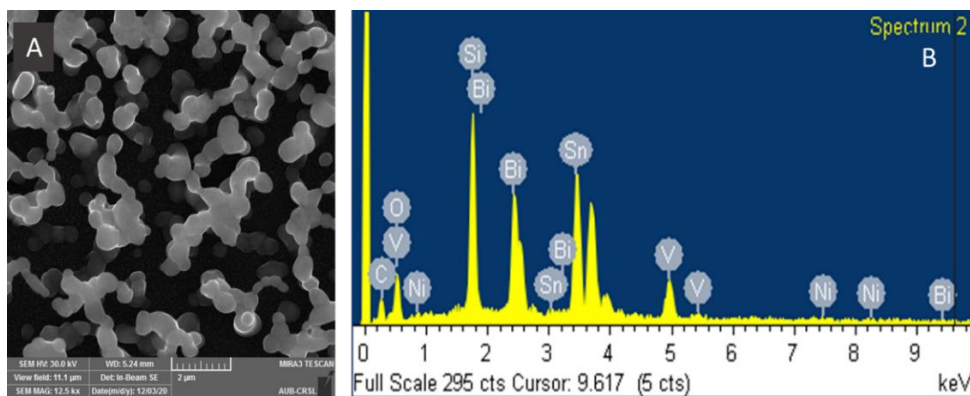


**Figure 45.** SEM images of (A) Ni- $\text{Bi}_i/\text{Mo:BiVO}_4$  with its EDX spectrum (B).

## 2. The Photoelectrochemical Behavior of Mo:BiVO<sub>4</sub> Photoanode before and after Ni-B<sub>i</sub> Bilayer Photodeposition

Figure 46 A shows the %IPCE of both average and the best film of highest %IPCE reached of Mo:BiVO<sub>4</sub> before and after Ni-B<sub>i</sub> photodeposition under same condition of Ni-B<sub>i</sub> photodeposition on the 282-i-TiO<sub>2</sub>-o/Mo:BiVO<sub>4</sub>. The onset photocurrent is at 500 - 520 nm which is consistent with Mo:BiVO<sub>4</sub> band gap ( $E_g = 2.4$  eV) and its absorption onset and generally a plateau with max %IPCE between 340 - 440 nm is observed.

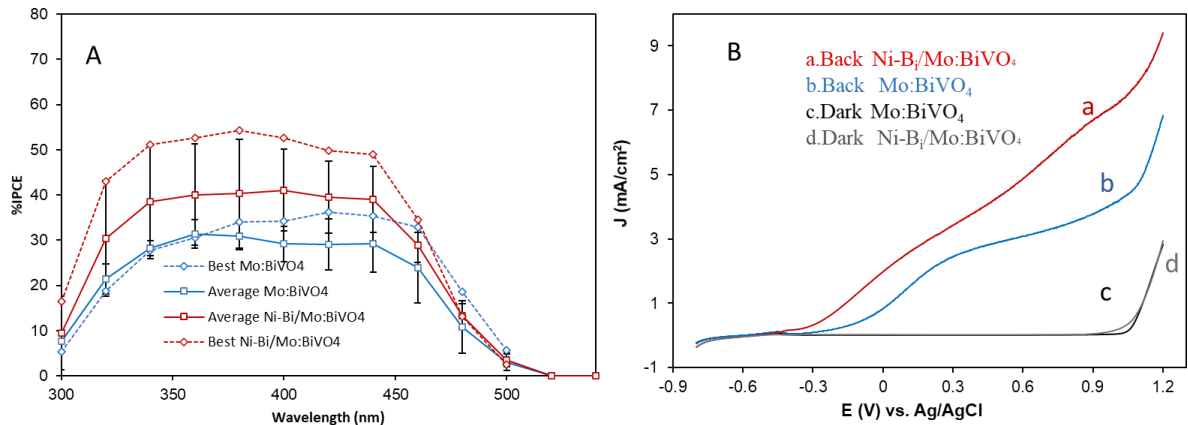


**Figure 46.** %IPCE at 0.6 V (A) of Mo:BiVO<sub>4</sub> and photodeposition of Ni-B<sub>i</sub> 3 min along with their (B) cyclic voltammograms under dark and light illumination. Electrolyte is 1M KB<sub>i</sub> (pH = 9.18) and scan rate is 10 mV/s

The %IPCE of the best Mo:BiVO<sub>4</sub> film in figure 46 A equaled 34.10 % at 380 nm, and after Ni-B<sub>i</sub> photodeposition, it increased to 54.33% at 380 nm. Moreover, the average %IPCE of Mo:BiVO<sub>4</sub> films equaled  $29.18 \pm 3.94$  % (N = 4) at 400 nm, and after the Ni-B<sub>i</sub> photodeposition, it increased to  $41.09 \pm 8.99$  % (N = 4) at 400 nm. The average %IPCE between 300 – 500 nm increased by a factor of  $1.31 \pm 0.16$  after 3 mins PD of Ni-B<sub>i</sub>. The best film (greatest %IPCE after modification with Ni-B<sub>i</sub>) showed a gain of 1.50 in %IPCE between 300 – 500 nm. It is shown that the overall %IPCE

enhancement of the spread Mo:BiVO<sub>4</sub> alone after PD of Ni-B<sub>i</sub> ( $1.31 \pm 0.16$ ) is greater than the enhancement obtained by the 282-i-TiO<sub>2</sub>-o/Mo:BiVO<sub>4</sub> ( $1.22 \pm 0.34$ ) between 300 – 500 nm in 1 M KB<sub>i</sub>. However, the % overall IPCE enhancement between 300 – 500 nm after PD of Ni-B<sub>i</sub> on the 282-i-TiO<sub>2</sub>-o/Mo:BiVO<sub>4</sub> whether relative to inverse opals ( $1.78 \pm 0.28$ ) or to Mo:BiVO<sub>4</sub> ( $2.09 \pm 0.48$ ) shown in figure 42 A is much greater than the enhancement obtained by Ni-B<sub>i</sub>/Mo:BiVO<sub>4</sub> shown in figure 46 A.

| <i>Films</i> | <b>Current Density (mA/cm<sup>2</sup>) at 0.6 V</b> |              |         | <b>Scan Rate ( 10 mV/s)</b>                 |              |         |
|--------------|---|--------------|---------|---|--------------|---------|
|              | <i>Before Photodeposition</i>                       |              |         | <i>After Photodeposition</i>                |              |         |
|              | <i>Mo:BiVO<sub>4</sub></i>                          |              |         | <i>Ni-B<sub>i</sub>/Mo:BiVO<sub>4</sub></i> |              |         |
|              | <i>Dark</i>   | <i>Light</i> |         | <i>Dark</i>                                 | <i>Light</i> |         |
| #1           | 0.01731   | 3.0756       | 3.05829 | 0.02471                                     | 4.88         | 4.85529 |
| #2           | 0.02259   | 2.5368       | 2.51421 | 0.02715                                     | 4.676        | 4.64885 |
| #3           | 0.03469   | 2.424        | 2.38931 | 0.02639                                     | 3.932        | 3.90561 |
| #4           | 0.02958   | 2.01         | 1.98042 | 0.01968                                     | 3.6584       | 3.63872 |

| <b>Average (mA/cm<sup>2</sup>) at 0.6 V</b> |   |
|---|---|
| <i>Mo:BiVO<sub>4</sub></i>                  | <i>Ni-B<sub>i</sub>/Mo:BiVO<sub>4</sub></i> |
| 2.49 ± 0.44                                 | 4.26 ± 0.58                                 |

**Table 3.** Current density at 0.6 V of cyclic voltammogram of figure 46 B of Ni-B<sub>i</sub>/Mo:BiVO<sub>4</sub> in 1 M KB<sub>i</sub> Electrolyte (pH= 9.18)

Figure 46 B shows the I-V curve of the best film of Mo:BiVO<sub>4</sub> before and after the photodeposition of Ni-B<sub>i</sub> in the dark and with light illumination in 1M KB<sub>i</sub> electrolyte of pH= 9.18 and upon back light illumination of 100 mW/cm<sup>2</sup> intensity. Table 3 shows the current density of Ni-B<sub>i</sub> /Mo:BiVO<sub>4</sub> at 0.6 V of the I-V curve of figure 46 B in 1 M KB<sub>i</sub> electrolyte of pH= 9.18 .The current density of Mo:BiVO<sub>4</sub> at 0.6 V vs Ag/AgCl is 3.05 mA/cm<sup>2</sup> and it increases to reach 4.86 mA/cm<sup>2</sup> after the PD of Ni-B<sub>i</sub> as shown in Figure 46 B. While the average current density of Mo:BiVO<sub>4</sub> (N = 4) at 0.6 V vs Ag/AgCl is  $2.49 \pm 0.44$  mA/cm<sup>2</sup> and it increases to reach  $4.36 \pm 0.58$  mA/cm<sup>2</sup> after PD of Ni-B<sub>i</sub>. The current density increases by  $1.71 \pm 1.32$ -fold after

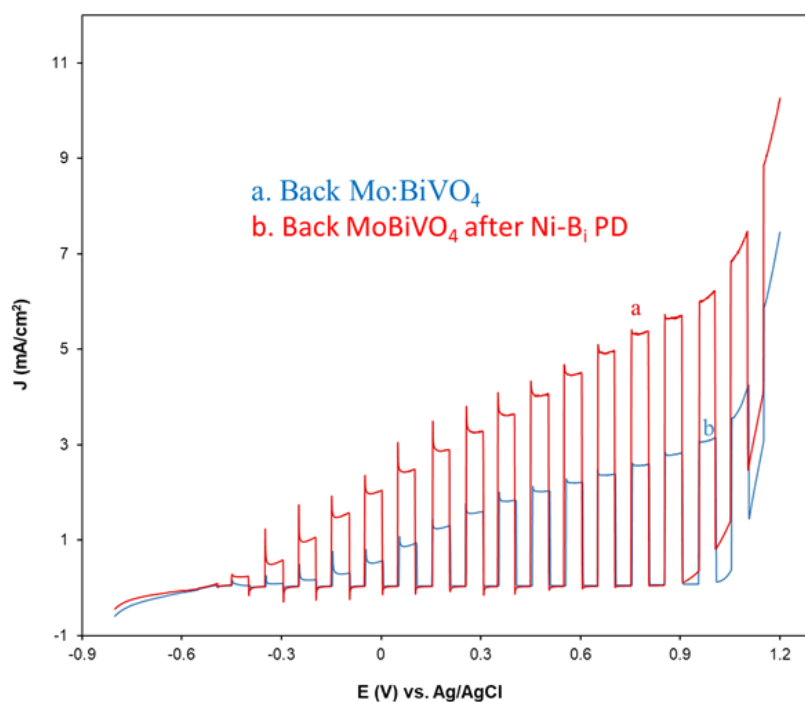
photodeposition of Ni-B<sub>i</sub>. Therefore, the average current densities in this I-V curve at 0.6 V also resulted in an enhancement consistent with the gain in %IPCE, but with larger values of the gain. The gain for best film in %IPCE is 1.5 smaller than the gain of the best film in I-V curve which is 1.71.

Table 4 shows the bias shift of I-V curves of Figure 46 B of Ni-B<sub>i</sub>/ Mo:BiVO<sub>4</sub> at 0.2 and 0.5 mA/cm<sup>2</sup> in 1 M KB<sub>i</sub> (pH= 9.18). In Figure 46 B, when the current density equals 0.2 mA/cm<sup>2</sup>, the bias shifts cathodically from -0.205 V vs Ag/AgCl to -0.36 V vs Ag/AgCl after photodeposition of Ni-B<sub>i</sub>. When the current density equals 0.5 mA/cm<sup>2</sup>, the bias shifts from -0.076 to -0.253 V vs Ag/AgCl after the photodeposition of Ni-B<sub>i</sub>. This shift and the increase in photocurrent at high bias are more likely due to the catalytic property of Ni-B<sub>i</sub> alongside the inhibition of electron-hole recombination by the catalyst. Figure 47 A shows the linear sweep voltammograms (LSV) of the best film in %IPCE of Mo:BiVO<sub>4</sub> before and after the photodeposition of Ni-B<sub>i</sub> under chopped light irradiation. The onset potential equals -0.548 V vs Ag/AgCl before PD of Ni-B<sub>i</sub> on Mo:BiVO<sub>4</sub>. No shift occurs in the onset potential after three mins PD of Ni-B<sub>i</sub>.

| Ni-B <sub>i</sub> /Mo:BiVO <sub>4</sub> at 0.2 mA/cm <sup>2</sup> |                            |   |
|---|----------------------------|---|
| <i>Figure 46 B</i>  | <i>Before PD</i>           | <i>After PD</i>                             |
| <i>Film # 1</i>   | <i>Mo:BiVO<sub>4</sub></i> | <i>Ni-B<sub>i</sub>/Mo:BiVO<sub>4</sub></i> |
| <i>Best in %IPCE</i>  | <i>Light</i>               | <i>Light</i>                                |
| <i>J (mA/cm<sup>2</sup>)</i>                                      | <i>0.20048</i>             | <i>0.20044</i>                              |
| <i>E(V) vs Ag/AgCl</i>  | <i>-0.205</i>              | <i>-0.36</i>                                |

| Ni-B <sub>i</sub> /Mo:BiVO <sub>4</sub> at 0.5 mA/cm <sup>2</sup> |                            |   |
|---|----------------------------|---|
| <i>Figure 46 B</i>  | <i>Before PD</i>           | <i>After PD</i>                             |
| <i>Film # 1</i>   | <i>Mo:BiVO<sub>4</sub></i> | <i>Ni-B<sub>i</sub>/Mo:BiVO<sub>4</sub></i> |
| <i>Best in % IPCE</i>   | <i>Light</i>               | <i>Light</i>                                |
| <i>J (mA/cm<sup>2</sup>)</i>                                      | <i>0.5028</i>              | <i>0.5028</i>                               |
| <i>E(V) vs Ag/AgCl</i>  | <i>-0.076</i>              | <i>-0.253</i>                               |

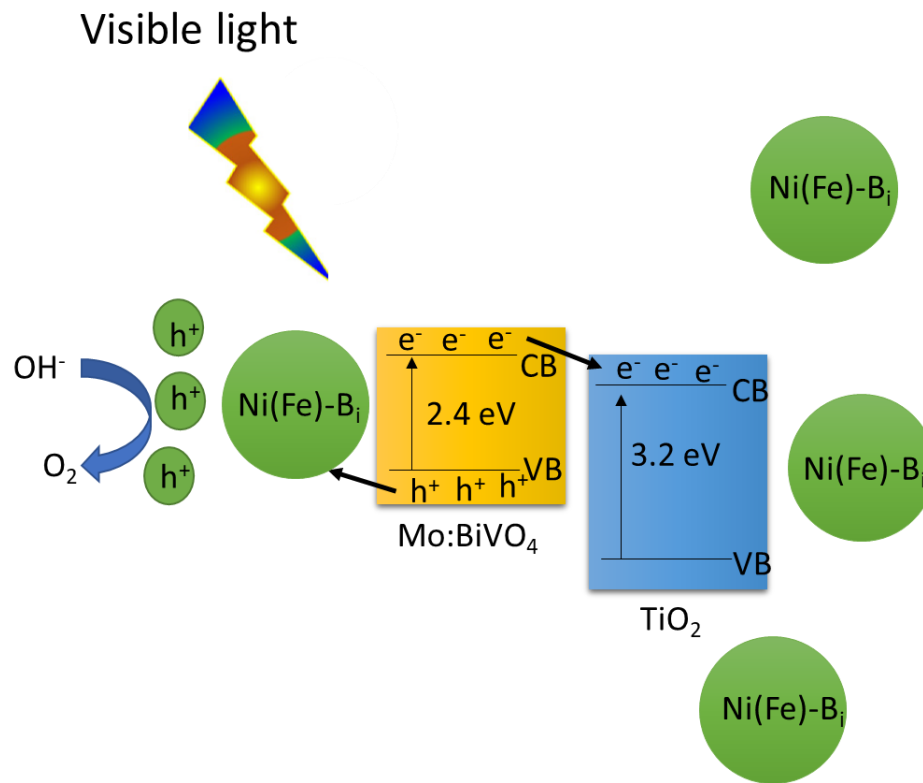
**Table 4.** Bias shift of I-V curves of Figure 46 B of Ni-B<sub>i</sub>/ Mo:BiVO<sub>4</sub> at 0.2 and 0.5 mA/cm<sup>2</sup> in 1 M KB<sub>i</sub> Electrolyte (pH= 9.18)



**Figure 47.** linear sweep voltammograms under chopped light irradiation at the Mo:BiVO<sub>4</sub> photoanode before and after photodeposition of Ni<sup>2+</sup>/KB<sub>i</sub> under 3 min back light illumination. Scan rate is 10 mV/s

It is noted therefore that Ni-B<sub>i</sub> increases the saturation (plateau) photocurrent in I-V curve, in addition to lowering the bias for low current density but doesn't cause a shift in onset potential. The increase in photocurrent at high bias can be attributed to a catalytic effect of Ni-B<sub>i</sub> (where there is a significant band bending as explained in chapter 1 C in the absence of or with small photocurrent transient). The combination of Ni-B<sub>i</sub>/282-i-TiO<sub>2</sub>-o/Mo:BiVO<sub>4</sub> electrodes are better in enhancement than the combination of Ni-B<sub>i</sub>/Mo:BiVO<sub>4</sub>.

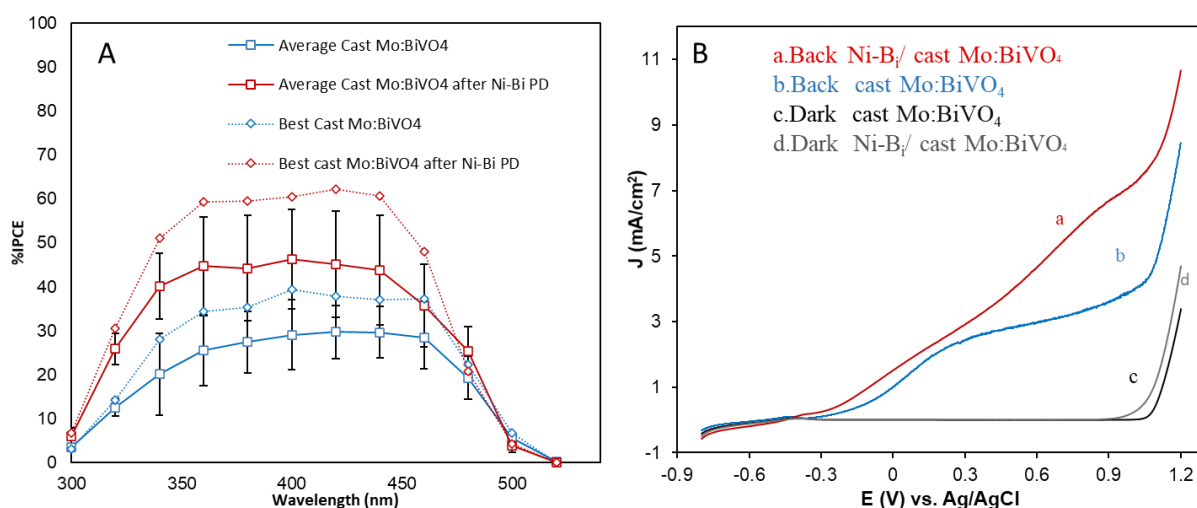
This is shown by Figure 48 which explains charge transfer processes in Ni-B<sub>i</sub>/i-TiO<sub>2</sub>-o/Mo:BiVO<sub>4</sub> photoanode upon visible light irradiation. When the visible light is irradiated, Mo:BiVO<sub>4</sub> generates electron-hole pairs. Oxidation of OH<sup>-</sup> to O<sub>2</sub> are allowed due to the photogenerated holes on the Mo:BiVO<sub>4</sub>. Due to the TiO<sub>2</sub> band energy ( $E_g = 3.2$  eV), TiO<sub>2</sub> cannot be excited by visible light. When a heterojunction is formed between TiO<sub>2</sub> and BiVO<sub>4</sub>, the photogenerated electrons in Mo:BiVO<sub>4</sub> are transferred to the conduction band (CB) of TiO<sub>2</sub> resulting in a driving force (more positive), and therefore charge separation is facilitated. Simultaneously, the photogenerated holes are depleted by co-catalyst Ni-Bi photodeposited on i-TiO<sub>2</sub>-o/Mo:BiVO<sub>4</sub>. This results in lowering electron-hole recombination in Mo:BiVO<sub>4</sub> and allows the oxidized Ni-B<sub>i</sub> co-catalyst to oxidize water. It is noted that the catalyst absorbs Fe impurities from the electrolyte as shown in previous studies,<sup>49</sup> and the active catalyst is therefore Ni(Fe)-B<sub>i</sub> boosting PEC water splitting as shown in Figure 48.



**Figure 48.** Scheme of charge transfer processes in Ni(Fe)-Bi/i-TiO<sub>2</sub>-o/Mo:BiVO<sub>4</sub> photocatalyst under visible light irradiation.

### ***3- Effect of Ni-Bi Photodeposition on Cast Mo:BiVO<sub>4</sub> on the Photoelectrochemical Behavior***

Another method was used to prepared Mo:BiVO<sub>4</sub> by casting 20  $\mu$ l on FTO without spreading, the same preparation conditions. The electrodes are modified with Ni-Bi in a front-wall light illumination for 3 min.



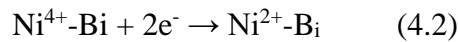
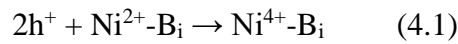
**Figure 49.** %IPCE at 0.6 V (A) of Cast Mo:BiVO<sub>4</sub> and photodeposition of Ni-Bi (0.4mM) along with their (B) cyclic voltammograms under dark and light illumination. Electrolyte is 1M KBi (pH = 9.18) and scan rate is 10 mV/s.

Figure 49 A shows the %IPCE of both average (N=4) and best film of cast Mo:BiVO<sub>4</sub> before and after Ni-Bi photodeposition for 3 mins of Ni-Bi. The onset photocurrent is at 500 - 520 nm which is consistent with Mo:BiVO<sub>4</sub> band gap (E<sub>g</sub>= 2.4 eV) and its absorption onset and generally plateau with max %IPCE between 340 - 440 nm. The %IPCE of the best Mo:BiVO<sub>4</sub> film in Figure 49 A equals 37.86 % at 420 nm, and after Ni-Bi photodeposition, it increased to 62.32 % at 420 nm. Moreover, the average %IPCE of Mo:BiVO<sub>4</sub> films equaled  $29.05 \pm 7.92$  % (N = 4) at 400 nm, and after the Ni-Bi photodeposition, it increased to  $46.26 \pm 11.31$  % (N = 4) at 400 nm. The average %IPCE between 300 – 500 nm increased by a factor of  $1.57 \pm 0.129$  after 3 mins PD of Ni-Bi. The best film (greatest %IPCE after modification with Ni-Bi) showed a gain of 1.56-fold in %IPCE between 300 – 500 nm. It is shown that the overall average %IPCE enhancement of the cast Mo:BiVO<sub>4</sub> alone after PD of Ni-Bi ( $1.57 \pm 0.129$ ) is greater than the enhancement obtained by the spread Mo:BiVO<sub>4</sub> ( $1.31 \pm 0.16$ ) after PD of Ni-Bi between 300 – 500 nm in 1 M KBi. However, still the 282-i-

TiO<sub>2</sub>-o/Mo:BiVO<sub>4</sub> after PD of Ni-B<sub>i</sub> has the greatest gain (2.09 ± 0.48) in average % IPCE between 300 – 500 nm.

Figure 49 B shows the I-V curve of the best film of the cast Mo:BiVO<sub>4</sub> before and after 3 mins PD of Ni-B<sub>i</sub>. The onset potential equals -0.344 V vs Ag/AgCl before PD of Ni-B<sub>i</sub> on Mo:BiVO<sub>4</sub> as shown in Figure 49 B. It shifts cathodically to -0.429 after three mins PD of Ni-B<sub>i</sub>. No shift occurred in the onset potential of spread Mo:BiVO<sub>4</sub> and 282-i-TiO<sub>2</sub>-o/Mo:BiVO<sub>4</sub> after photodeposition of Ni-B<sub>i</sub> for 3 mins. When the current density equals 0.2 mA/cm<sup>2</sup>, the bias shifts cathodically from -0.231 V vs Ag/AgCl to -0.345 V vs Ag/AgCl after the after photodeposition of Ni-B<sub>i</sub> as shown in Figure 49 B. When the current density equals 0.5 mA/cm<sup>2</sup>, the bias shifts from -0.112 to -0.211 V vs Ag/AgCl after the photodeposition of Ni-B<sub>i</sub>.

Therefore, Ni-B<sub>i</sub> appears increase the photocurrent at lower bias and high bias by reducing recombination especially at low bias (small band bending) and its catalytic effect.



It can be explained that Ni-B<sub>i</sub> mediates the hole transfer leading to inhibition in the recombination of electron–hole pairs photogenerated at BiVO<sub>4</sub> through the cyclic change of Ni oxidation states (II/IV) as shown in equation 4.1 and 4.2 .<sup>55</sup> Therefore, the photogenerated electrons lead to the increase in photocurrent and % IPCE.

### C. Conclusions

In this chapter, the photoelectrochemical behavior of bilayer  $i\text{-TiO}_2\text{-o}/\text{Mo:BiVO}_4$  modified with  $\text{Ni-B}_i$  OER co-catalyst in borate buffer was studied. The effect of the  $i\text{-TiO}_2\text{-o}$  and  $\text{Ni-B}_i$  OER catalyst on water oxidation in borate buffer was compared to the effect of  $\text{Ni-B}_i$  on spread  $\text{Mo:BiVO}_4$  and on cast  $\text{Mo:BiVO}_4$  photoanodes. It is concluded from these studies that:

- 1) The enhancement in light harvesting caused by the  $i\text{-TiO}_2\text{-o}$  for water oxidation has lower gain in light harvesting in the presence of a hole scavenger attributed to kinetic limitations in water oxidation.
- 2) The bilayer  $\text{Ni-B}_i/282\text{-}i\text{-TiO}_2\text{-o}/\text{Mo:BiVO}_4$  electrodes showed a higher gain in photocurrent than  $\text{Ni-B}_i/\text{Mo:BiVO}_4$  and  $\text{Ni-B}_i/\text{cast Mo:BiVO}_4$  in both %IPCE and I-V curves, relative to the  $\text{Mo:BiVO}_4$  as a result of  $\text{Ni-B}_i$  modification.
- 3)  $\text{Ni-B}_i$  co-catalyst results in increasing saturation photocurrent (high bias, large band bending). These effects are attributed to its dual role by reducing recombination especially at low bias (small band bending at both  $\text{Mo:BiVO}_4$  and bilayer), increasing photocurrent at high bias and its catalytic effect.
- 4) The  $\text{Ni-B}_i/\text{cast Mo:BiVO}_4$  electrodes showed higher photocurrent enhancement in %IPCE than  $\text{Ni-B}_i/\text{spread Mo:BiVO}_4$ .
- 5) The highest gain in photocurrent reached by  $\text{Ni-B}_i/282\text{-}i\text{-TiO}_2\text{-o}/\text{Mo:BiVO}_4$  relative to  $\text{Mo:BiVO}_4$  was greater than the gain resulting from  $\text{Ni-B}_i/282\text{-}i\text{-TiO}_2\text{-o}/\text{Mo:BiVO}_4$  relative to bilayer and from  $282\text{-}i\text{-TiO}_2\text{-o}$  on  $\text{Mo:BiVO}_4$ .
- 6) The PD of  $\text{Ni-B}_i$  on  $282\text{-}i\text{-TiO}_2\text{-o}/\text{Mo:BiVO}_4$  did not affect the onset potential, however the  $282\text{-}i\text{-TiO}_2\text{-o}$  deposition caused a cathodic shift in the onset potential.

## CHAPTER V

### CONCLUSION

In this thesis work, the effect of TiO<sub>2</sub> photonic crystals of varying stop bands on light harvesting at Mo:BiVO<sub>4</sub> films, in a photoelectrochemical cell in the presence of hole scavenger (sulfate sulfite solution ) to minimize the kinetics limitations was studied. The effect of TiO<sub>2</sub> inverse opal on the photocurrent conversion efficiency of Mo:BiVO<sub>4</sub> was compared to disordered inverse glass and non-scattering nanocrystalline TiO<sub>2</sub> films. The photoelectrochemical behavior of bilayer i-TiO<sub>2</sub>-o/Mo:BiVO<sub>4</sub> of modified Ni-B<sub>i</sub> co-catalyst on water oxidation was investigated. The effect of the i-TiO<sub>2</sub>-o and Ni-B<sub>i</sub> OER catalyst in borate buffer compared to Ni-B<sub>i</sub>/ spread Mo:BiVO<sub>4</sub> and Ni-B<sub>i</sub>/ cast Mo:BiVO<sub>4</sub> photoanodes was studied.

In the study of the effect of light harvesting of TiO<sub>2</sub> photonic crystals by varying stop bands coupled to Mo:BiVO<sub>4</sub> electrodes in the presence of hole scavenger in sulfate sulfite electrolyte (Chapter 3), the effect of Mo:BiVO<sub>4</sub> coupled to TiO<sub>2</sub> inverse opal was compared to disordered inverse glass and non-scattering nanocrystalline TiO<sub>2</sub> films. The photocurrent gain was found to be caused by structural ordered TiO<sub>2</sub> inverse opals, the internal light trapping and backscattering in the i-TiO<sub>2</sub>-o/Mo:BiVO<sub>4</sub>. It was shown that absorption of light by inverse opal TiO<sub>2</sub> can lead to photocurrent generation and affect both the photocurrent onset and increases the photocurrent under white light illumination. As the thickness of Mo:BiVO<sub>4</sub> increased ( its initial %IPCE is higher), as the film structure was more packed caused by coupling i-TiO<sub>2</sub>-o photocurrent decreases.

The I-V curves of 282-i-TiO<sub>2</sub>-g/Mo:BiVO<sub>4</sub> electrodes showed a contribution from 282-i-TiO<sub>2</sub>-g contacting FTO or photogenerated charges from TiO<sub>2</sub> absorbance.

While in % IPCE plots, photocurrents enhancement at 380 nm and longer wavelength originated from Mo:BiVO<sub>4</sub> and shorter wavelengths can have contribution from TiO<sub>2</sub>. The enhancement in photocurrent was caused by the structural ordered inverse opals rather than disordered or a heterojunction with non-scattering nanocrystalline TiO<sub>2</sub>. Despite the heterojunction between nc-TiO<sub>2</sub> and Mo:BiVO<sub>4</sub> the small size of the nc-TiO<sub>2</sub> hindered the contact of Mo:BiVO<sub>4</sub> with electrolyte or the absence of a transport path from the nc-TiO<sub>2</sub>/Mo:BiVO<sub>4</sub> film to FTO.

Although scattering occurred in the disordered films which caused gain for some films but, it is maybe that there was a greater backscattering in ordered inverse opals. It would also be that the coupling of order with disorder contributed to different internal light trapping and greater backscattering. It was shown also that the effect cannot be caused directly by Bragg reflection since the stop band peak is located toward the red region through it extends over a broad frequency range.

The role of NaCl was proven to decrease the photocurrent of 282-i-TiO<sub>2</sub>-g/Mo:BiVO<sub>4</sub> by masking the enhancement caused by disordered structure in the photocurrent. The NaCl presence could not be the full cause why the 282-i-TiO<sub>2</sub>-g/Mo:BiVO<sub>4</sub> film did not cause ca. 2.21-fold gain as observed with 282-i-TiO<sub>2</sub>-o/Mo:BiVO<sub>4</sub>.

The enhancement in photocurrent of bilayer 227-i-TiO<sub>2</sub>-o/Mo:BiVO<sub>4</sub> is much greater when both %IPCE and I-V curves are done in back-wall illumination rather than in front-wall illumination. The enhancement in photocurrent is not on stop band, however highly dependent on its position because even by varying the photonic crystal stop band from 305 nm , 282nm, 227 nm to 150 nm polystyrene spheres, the photocurrent enhancement was observed.

In the study of the photoelectrochemical behavior of Ni-B<sub>i</sub> co-catalyst at bilayer 282-i-TiO<sub>2</sub>-o/Mo:BiVO<sub>4</sub> on water oxidation at the OEC in 1 M KB<sub>i</sub> solution (chapter 4), the effect of bilayer i-TiO<sub>2</sub>-o/Mo:BiVO<sub>4</sub> of modified Ni-B<sub>i</sub> co-catalyst on water oxidation was studied. The effect of the i-TiO<sub>2</sub>-o and Ni-B<sub>i</sub> OER catalyst in borate buffer compared to Ni-B<sub>i</sub>/ spread Mo:BiVO<sub>4</sub> and Ni-B<sub>i</sub>/ cast Mo:BiVO<sub>4</sub> photoanodes was also studied. The enhancement in light harvesting was found to be caused by the i-TiO<sub>2</sub>-o for water oxidation that has lower gain in light harvesting in the presence of a hole scavenger attributed to kinetic limitations in water oxidation.

The bilayer Ni-B<sub>i</sub>/282-i-TiO<sub>2</sub>-o/Mo:BiVO<sub>4</sub> electrodes showed a higher gain in photocurrent than Ni-B<sub>i</sub>/Mo:BiVO<sub>4</sub> and Ni-B<sub>i</sub>/ cast Mo:BiVO<sub>4</sub> in both %IPCE and I-V curves, relative to the Mo:BiVO<sub>4</sub> as a result of Ni-B<sub>i</sub> modification. Ni-B<sub>i</sub> co-catalyst results in increasing saturation photocurrent (high bias, large band bending). These effects are attributed to its dual role by reducing recombination especially at low bias (small band bending at both Mo:BiVO<sub>4</sub> and bilayer), increasing photocurrent at high bias and its catalytic effect.

The Ni-B<sub>i</sub>/ cast Mo:BiVO<sub>4</sub> electrodes showed higher photocurrent enhancement in %IPCE than Ni-B<sub>i</sub>/ spread Mo:BiVO<sub>4</sub>. The highest gain in photocurrent reached by Ni-B<sub>i</sub>/282-i-TiO<sub>2</sub>-o/Mo:BiVO<sub>4</sub> relative to Mo:BiVO<sub>4</sub> was greater than the gain resulting from Ni-B<sub>i</sub>/282-i-TiO<sub>2</sub>-o/Mo:BiVO<sub>4</sub> relative to bilayer and from 282-i-TiO<sub>2</sub>-o on Mo:BiVO<sub>4</sub>. The PD of Ni-B<sub>i</sub> on 282-i-TiO<sub>2</sub>-o/Mo:BiVO<sub>4</sub> did not affect the onset potential, however the 282-i-TiO<sub>2</sub>-o deposition caused a cathodic shift in the onset potential.

Future studies can be conducted by including different guest metals (Fe, Al, or Co) to Ni-oxo/hydroxo co-catalyst materials coupled photoelectrodes to pave the way for more efficient and stable solar water splitting. Other catalyst materials of interest to be couple to the electrode that are bi-functional for OER and HER such as Ni-Selenides and phosphates. Further studies can also vary the thickness of the i-TiO<sub>2</sub>-o layer to enhance water oxidation in thinner films.

## REFERENCES

1. Mao, S. S.; Shen, S.; Guo, L., Nanomaterials for renewable hydrogen production, storage and utilization. *Progress in Natural Science: Materials International* **2012**, 22 (6), 522-534.
2. Abas, N.; Kalair, E.; Kalair, A.; Hasan, Q. u.; Khan, N., Nature inspired artificial photosynthesis technologies for hydrogen production: Barriers and challenges. *International Journal of Hydrogen Energy* **2020**, 45 (41), 20787-20799.
3. Bediako, D. K.; Surendranath, Y.; Nocera, D. G., Mechanistic studies of the oxygen evolution reaction mediated by a nickel-borate thin film electrocatalyst. *J Am Chem Soc* **2013**, 135 (9), 3662-74.
4. Fayad, R.; Dhainy, J.; Ghandour, H.; Halaoui, L., Electrochemical study of the promoting effect of Fe on oxygen evolution at thin 'NiFe-Bi' films and the inhibiting effect of Al in borate electrolyte. *Catalysis Science & Technology* **2017**, 7 (17), 3876-3891.
5. Decker, F.; Cattarin, S., Photoelectrochemical cells *Elsevier* **2009**, 1-9.
6. Hisatomi, T.; Kubota, J.; Domen, K., Recent advances in semiconductors for photocatalytic and photoelectrochemical water splitting. *Chem Soc Rev* **2014**, 43 (22), 7520-35.
7. Ni, M.; Leung, M. K. H.; Leung, D. Y. C.; Sumathy, K., A review and recent developments in photocatalytic water-splitting using TiO<sub>2</sub> for hydrogen production. *Renewable and Sustainable Energy Reviews* **2007**, 11 (3), 401-425.
8. Kocha, S. S.; Montgomery, D.; Peterson, M. W.; Turner, J. A., Photoelectrochemical decomposition of water utilizing monolithic tandem cells. *Solar Energy Materials and Solar Cells* **1998**, 389 - 397.
9. Nocera, D. G., The artificial leaf. *Acc Chem Res* **2012**, 45 (5), 767-76.
10. Fujishima, A.; Honda, K., Electrochemical Photolysis of Water at a Semiconductor Electrode. *Nature* **1972**, 238, 37.
11. Liao, C.-H.; Huang, C.-W.; Wu, J. C. S., Hydrogen Production from Semiconductor-based Photocatalysis via Water Splitting. *Catalysts* **2012**, 2 (4), 490-516.
12. Minggu, L. J.; Wan Daud, W. R.; Kassim, M. B., An overview of photocells and photoreactors for photoelectrochemical water splitting. *International Journal of Hydrogen Energy* **2010**, 35 (11), 5233-5244.
13. Ahmad, H.; Kamarudin, S. K.; Minggu, L. J.; Kassim, M., Hydrogen from photo-catalytic water splitting process: A review. *Renewable and Sustainable Energy Reviews* **2015**, 43, 599-610.
14. Suen, N. T.; Hung, S. F.; Quan, Q.; Zhang, N.; Xu, Y. J.; Chen, H. M., Electrocatalysis for the oxygen evolution reaction: recent development and future perspectives. *Chem Soc Rev* **2017**, 46 (2), 337-365.
15. Reier, T.; Nong, H. N.; Teschner, D.; Schlogl, R.; Strasser, P., Electrocatalytic oxygen evolution reaction in acidic environments-reaction mechanisms and catalysts. *Advanced Energy Materials* **2017**, 7 (1).
16. Shinagawa, T.; Garcia-Esparza, A. T.; Takanabe, K., Insight on Tafel slopes from a microkinetic analysis of aqueous electrocatalysis for energy conversion. *Sci Rep* **2015**, 5, 13801.

17. Rahman, M. A., A Review on Semiconductors Including Applications and Temperature Effects in Semiconductors. *American Scientific Research Journal for Engineering, Technology, and Sciences (ASRJETS)* **7** (2014), 50-70.
18. Bard, A. J.; Faulkner, L. R., PHOTOELECTROCHEMISTRY AND ELECTROGENERATED CHEMILUMINESCENCE. In *ELECTROCHEMICAL METHODS : Fundamentals and Applications* Second ed.; Harris, D.; Swain, E.; Robey, C.; Aiello, E., Eds. JOHN WILEY & SONS, INC.: 2001; pp 745-760.
19. Knight, A. W.; Greenway, G. M., *Analyst*. **1994**, 119.
20. Bard, A. J., Inner-sphere heterogeneous electrode reactions. Electrocatalysis and photocatalysis: the challenge. *J Am Chem Soc* **2010**, *132* (22), 7559-67.
21. Iwase, A.; Kudo, A., Photoelectrochemical water splitting using visible-light-responsive BiVO<sub>4</sub> fine particles prepared in an aqueous acetic acid solution. *Journal of Materials Chemistry* **2010**, *20* (35).
22. Zhou, M.; Bao, J.; Xu, Y.; Zhang, J.; Xie, J.; Guan, M.; Wang, C.; Wen, L.; Lei, Y.; Xie, Y., Photoelectrodes Based upon Mo: BiVO<sub>4</sub> Inverse Opals for Photoelectrochemical Water Splitting. *ACS Nano* **2014**, *8*, 7088-7098.
23. Ye, H.; Lee, J.; Jang, J. S.; Bard, A. J., Rapid Screening of BiVO<sub>4</sub>-Based Photocatalysts by Scanning Electrochemical Microscopy (SECM) and Studies of Their Photoelectrochemical Properties. *American Chemical Society* **2010**, *114*, 13322-13328.
24. Pilli, S. K.; Janarthanan, R.; Deutsch, T. G.; Furtak, T. E.; Brown, L. D.; Turner, J. A.; Herring, A. M., Efficient photoelectrochemical water oxidation over cobalt-phosphate (Co-Pi) catalyst modified BiVO<sub>4</sub>/1D-WO<sub>3</sub> heterojunction electrodes. *Phys Chem Chem Phys* **2013**, *15* (35), 14723-8.
25. Talasila, G.; Sachdev, S.; Srivastva, U.; Saxena, D.; Ramakumar, S. S. V., Modified synthesis of BiVO<sub>4</sub> and effect of doping (Mo or W) on its photoelectrochemical performance for water splitting. *Energy Reports* **2020**, *6*, 1963-1972.
26. Li, H.; Yu, H.; Quan, X.; Chen, S.; Zhao, H., Improved photocatalytic performance of heterojunction by controlling the contact facet: high electron transfer capacity between TiO<sub>2</sub> and the {110} facet of BiVO<sub>4</sub> caused by suitable energy band alignment. *Advanced Functional Materials* **2015**, 3074-3080.
27. Zhang, X.; Wang, X.; Wang, D.; Ye, J., Conformal BiVO<sub>4</sub>-layer/WO<sub>3</sub>-nanoplate-array heterojunction photoanode modified with cobalt phosphate cocatalyst for significantly enhanced photoelectrochemical performances. *ACS Applied Material* **2018**, 5623-5631.
28. Abdi, F. F.; van de Krol, R., Nature and Light Dependence of Bulk Recombination in Co-Pi-Catalyzed BiVO<sub>4</sub> Photoanodes. *The Journal of Physical Chemistry C* **2012**, *116* (17), 9398-9404.
29. Liang, Y.; Tsubota, T.; Mooij, L. P. A.; van de Krol, R., Highly Improved Quantum Efficiencies for Thin Film BiVO<sub>4</sub> Photoanodes. *The Journal of Physical Chemistry C* **2011**, *115* (35), 17594-17598.
30. Abdi, F. F.; Firet, N.; van de Krol, R., Efficient BiVO<sub>4</sub>Thin Film Photoanodes Modified with Cobalt Phosphate Catalyst and W-doping. *ChemCatChem* **2013**, *5* (2), 490-496.
31. Chiappini, A.; Tran, L. T. N.; Trejo-Garcia, P. M.; Zur, L.; Lukowiak, A.; Ferrari, M.; Righini, G. C., Photonic Crystal Stimuli-Responsive Chromatic Sensors: A Short Review. *Micromachines (Basel)* **2020**, *11* (3).

32. Bayram, S.; Halaoui, L., Amplification of Solar Energy Conversion in Quantum-Confined CdSe-Sensitized TiO<sub>2</sub> Photonic Crystals by Trapping Light. *Particle & Particle Systems Characterization* **2013**, *30* (8), 706-714.
33. Garcia, P. D.; Sapienza, R.; Lopez, C., Photonic glasses: a step beyond white paint. *Adv Mater* **2010**, *22* (1), 12-9.
34. Nishimura, S.; Abrams, N.; Lewis, B. A.; Halaoui, L. I.; Mallouk, T. E.; Benkstein, K. D.; van de Lagemaat, J.; Frank, A. J., Standing wave enhancement of red absorbance and photocurrent in dye-sensitized titanium dioxide photoelectrodes coupled to photonic crystals. *J Am Chem Soc* **2003**, *125* (20), 6306-10.
35. Yablonovitch, E., Inhibited spontaneous emission in solid-state physics and electronics. *Phys Rev Lett* **1987**, *58* (20), 2059-2062.
36. John, S., Strong localization of photons in certain disordered dielectric superlattices. *Phys Rev Lett* **1987**, *58* (23), 2486-2489.
37. Joannopoulos, J. D.; Johnson, S. G.; Winn, J. N.; Meade, R. D., Photonic Crystals Molding the Flow of Light. Second ed.; Princeton University Press: 2008; p 302.
38. Müller, M.; Zentel, R.; Maka, T.; Romanov, S. G.; Torres, C. M. S., Photonic Crystal Films with High Refractive Index Contrast. *Advanced Materials* **2000**.
39. Mekis, A.; Chen, J. C.; Kurland, I.; Fan, S.; Villeneuve, P. R.; Joannopoulos, J. D., High Transmission through Sharp Bends in Photonic Crystal Waveguides. *Physical Review Letters* **1996**.
40. Beydoun, N.; Farhat, R.; Halaoui, L. I., Enhanced Solar Light Harvesting with Q-CdTe/Se Sensitized Inverse Opal TiO<sub>2</sub>. *ACS Applied Energy Materials* **2020**, *3* (3), 3104-3119.
41. El Harakeh, M.; Halaoui, L., Enhanced Conversion of Light at TiO<sub>2</sub> Photonic Crystals to the Blue of a Stop Band and at TiO<sub>2</sub> Random Films Sensitized with Q-CdS: Order and Disorder. *The Journal of Physical Chemistry C* **2010**, *114* (6), 2806-2813.
42. Yip, C.-H.; Chiang, Y.-M.; Wong, C.-C., Dielectric Band Edge Enhancement of Energy Conversion Efficiency in Photonic Crystal Dye-Sensitized Solar Cell. *The Journal of Physical Chemistry C* **2008**, *112* (23), 8735-8740.
43. Wolf, P.-E.; Maret, G., Weak Localization and Coherent Backscattering of Photons in Disordered Media. *Physical Review Letters* **1985**, *55* (24), 2696-2699.
44. van der Mark, M. B.; van Albada, M. P.; Lagendijk, A., Light scattering in strongly scattering media: Multiple scattering and weak localization. *Physical Review B* **1988**, *37* (7), 3575-3592.
45. Lv, Y.-R.; Liu, C.-J.; He, R.-K.; Li, X.; Xu, Y.-H., BiVO<sub>4</sub>/TiO<sub>2</sub> heterojunction with enhanced photocatalytic activities and photoelectrochemistry performances under visible light illumination. *Materials Research Bulletin* **2019**, *117*, 35-40.
46. Zhang, H.; Cheng, C., Three-Dimensional FTO/TiO<sub>2</sub>/BiVO<sub>4</sub> Composite Inverse Opals Photoanode with Excellent Photoelectrochemical Performance. *ACS Energy Letters* **2017**, *2* (4), 813-821.
47. OLIVA, P.; LEONARD, J.; LAURENT, J. F., REVIEW OF THE STRUCTURE AND THE ELECTROCHEMISTRY OF NICKEL HYDROXIDES AND OXY-HYDROXIDES. *Journal of Power Sources*, **1982**, *8*, 229 - 255.

48. Hall, D. S.; Lockwood, D. J.; Bock, C.; MacDougall, B. R., Nickel hydroxides and related materials: a review of their structures, synthesis and properties. *Proc Math Phys Eng Sci* **2015**, *471* (2174), 20140792.
49. Klaus, S.; Cai, Y.; Louie, M. W.; Trotochaud, L.; Bell, A. T., Effects of Fe Electrolyte Impurities on Ni(OH)<sub>2</sub>/NiOOH Structure and Oxygen Evolution Activity. *The Journal of Physical Chemistry C* **2015**, *119* (13), 7243-7254.
50. Bode, H.; Dehmelt, K.; Witt, J., UR KENNTNIS DER NICKELHYDROXIDELEKTRODE-I. ijBER DAS NICKEL (II)-HYDROXIDHYDRAT. *IZkctrmhimica Acta* **1966**, *11*, 1079-1087.
51. Dionigi, F.; Strasser, P., NiFe-Based (Oxy)hydroxide Catalysts for Oxygen Evolution Reaction in Non-Acidic Electrolytes. *Advanced Energy Materials* **2016**, *6* (23).
52. Zhang, W.; Ma, J.; Xiong, L.; Jiang, H.-Y.; Tang, J., Well-Crystallized  $\alpha$ -FeOOH Cocatalysts Modified BiVO<sub>4</sub> Photoanodes for Efficient and Stable Photoelectrochemical Water Splitting. *ACS Applied Energy Materials* **2020**, *3* (6), 5927-5936.
53. Zhang, X.; Li, H.; Kong, W.; Liu, H.; Fan, H.; Wang, M., Reducing the surface recombination during light-driven water oxidation by core-shell BiVO<sub>4</sub>@Ni:FeOOH. *Electrochimica Acta* **2019**, *300*, 77-84.
54. Du, P.; Kokhan, O.; Chapman, K. W.; Chupas, P. J.; Tiede, D. M., Elucidating the domain structure of the cobalt oxide water splitting catalyst by X-ray pair distribution function analysis. *J Am Chem Soc* **2012**, *134* (27), 11096-9.
55. Choi, S. K.; Choi, W.; Park, H., Solar water oxidation using nickel-borate coupled BiVO<sub>4</sub> photoelectrodes. *Phys Chem Chem Phys* **2013**, *15* (17), 6499-507.
56. Rettie, A. J.; Lee, H. C.; Marshall, L. G.; Lin, J. F.; Capan, C.; Lindemuth, J.; McCloy, J. S.; Zhou, J.; Bard, A. J.; Mullins, C. B., Combined charge carrier transport and photoelectrochemical characterization of BiVO<sub>4</sub> single crystals: intrinsic behavior of a complex metal oxide. *J Am Chem Soc* **2013**, *135* (30), 11389-96.
57. Madiabu, M. J.; Gunlazuardi, J., Preparation and characterization of TiO<sub>2</sub>/BiVO<sub>4</sub> composite: Can this photocatalyst, under visible light, be able to eliminate rhodamine B from water and why? 2018.
58. Zalfani, M.; van der Schueren, B.; Hu, Z.-Y.; Rooke, J. C.; Bourguiga, R.; Wu, M.; Li, Y.; Van Tendeloo, G.; Su, B.-L., Novel 3DOM BiVO<sub>4</sub>/TiO<sub>2</sub> nanocomposites for highly enhanced photocatalytic activity. *Journal of Materials Chemistry A* **2015**, *3* (42), 21244-21256.
59. Walter, M. G.; Warren, E. L.; McKone, J. R.; Boettcher, S. W.; Mi, Q.; Santori, E. A.; Lewis, N. S., Solar water splitting cells. *Chem Rev* **2010**, *110* (11), 6446-73.
60. Zhong, D. K.; Choi, S.; Gamelin, D. R., Near-complete suppression of surface recombination in solar photoelectrolysis by "Co-Pi" catalyst-modified W:BiVO<sub>4</sub>. *J Am Chem Soc* **2011**, *133* (45), 18370-7.
61. Liu, B. T.; Lin, Y. L.; Huang, S. X., Photonic bandgap of inverse opals prepared from core-shell spheres. *Nanoscale Res Lett* **2012**, *7* (1), 457.
62. Suriye, K.; Praserthdam, P.; Jongsomjit, B., Control of Ti<sup>3+</sup>-surface defect on TiO<sub>2</sub> nanocrystal using various calcination atmospheres as the first step for surface defect creation and its application in photocatalysis. *Applied Surface Science* **2007**, *253* (8), 3849-3855.

63. Trotochaud, L.; Ranney, J. K.; Williams, K. N.; Boettcher, S. W., Solution-cast metal oxide thin film electrocatalysts for oxygen evolution. *J Am Chem Soc* **2012**, *134* (41), 17253-61.
64. Park, H.; Park, B. H.; Choi, J.; Kim, S.; Kim, T.; Youn, Y. S.; Son, N.; Kim, J. H.; Kang, M., Enhanced Electrochemical Properties and OER Performances by Cu Substitution in NiCo<sub>2</sub>O<sub>4</sub> Spinel Structure. *Nanomaterials (Basel)* **2020**, *10* (9).
65. Kong, D.; Qi, J.; Liu, D.; Zhang, X.; Pan, L.; Zou, J., Ni-Doped BiVO<sub>4</sub> with V<sup>4+</sup> Species and Oxygen Vacancies for Efficient Photoelectrochemical Water Splitting. *Transactions of Tianjin University* **2019**, *25* (4), 340-347.
66. P. Soni; V.V.S. Murty; Kushwaha, K. K., The Effect of Ni<sup>2+</sup> Ions on Energy Band Gap of TiO<sub>2</sub> Nanoparticles for Solar Cell Applications. *STM* **2018**, *8* (2), 69-74.
67. Gutierrez, P. S. a. C., ANALYSIS OF THE TRANSIENT PHOTOCURRENT-TIME BEHAVIOUR OF A SINTERED n-SrTiO<sub>3</sub> ELECTRODE IN WATER PHOTOELECTROLYSIS. *J. Electroanal. Chem* **1984**, *160*, 117-130.

